ASPECTS OF MAGNETIC FIELD THEORY IN SOLAR AND LABORATORY PLASMAS

Robert M. Lothian

A Thesis Submitted for the Degree of PhD
at the
University of St Andrews

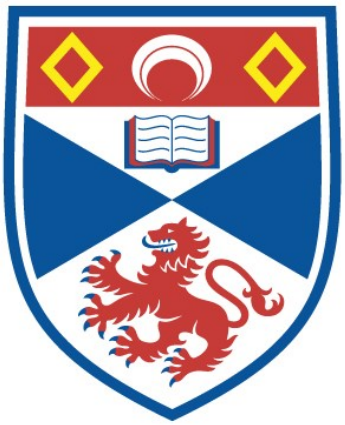

1990

Aspects of Magnetic Field Theory in Solar and Laboratory Plasmas

Robert M. Lothian

A thesis submitted for the degree of Doctor of Philosophy at the University of St. Andrews

Abstract.

Using the Magnetohydrodynamic model, two problems in the behaviour of magnetic field structures are investigated. Firstly, the stability of tokamak equilibria to coupled tearing modes is calculated. Secondly, the equilibrium structure of a solar coronal loop is examined.

The flux co-ordinate method is used to construct toroidal equilibria of the type found in large aspect ratio tokamaks. In such a field configuration, the analysis of tearing modes is complicated by the coupling of different poloidal fourier modes. The effect of coupling through elliptic shaping of plasma surfaces is calculated. For certain current profiles, this effect may cause instability.

The response of coronal loops to twisting at their photospheric footpoints is investigated. Long loops are shown to have an essentially 1-D nature. This observation is used to develop a 1-D, line-tied model for such loops. This model is used to conduct an extensive survey of the non-linear twist regime, including the effects of enhanced fluid pressure. The possibility of non-equilibrium, which would provide energy for coronal heating and compact flares, is examined. When the physical variable of footpoint displacement is specified, no loss of equilibrium is found by twisting. Loss of equilibrium is found for high pressures, which we do not, however, expect to find in the corona.

I, Robert McKay Lothian, hereby certify that this thesis has been composed by myself, that it is a record of my own work, and that it has not been accepted in partial or complete fulfilment of any other degree or professional qualification.

Signature of Candidate _____

Date 17th May 1990

I was admitted to the faculty of Science of the University of St. Andrews under Ordinance General No. 12 on 1st. October 1986 and as a candidate for the degree of Ph.D. on 1st. October 1987.

Signature of Candidate _____

Date 17th May 1990

I hereby certify that the candidate has fulfilled the conditions of the Resolution and Regulations appropriate to the degree of Ph.D.

Signature of Supervisor ___

Date 17/5/90

Acknowledgements

I would like to thank the many people who have helped me in the creation of this thesis.

Alan Hood, my long-suffering supervisor, has been patient, tolerant, diligent and pretty good at maths, too !

Everyone in the solar group and everybody else in the Maths Department at St. Andrews have been a mine of help and good advice.

My supervisors at Culham Laboratory, Jack Connor and Jim Hastie, have patiently initiated me into the mysteries of laboratory MHD.

Many other people at Culham have been most helpful and hospitable, particularly Terry Martin and Peter Kirby.

Vital financial support was received from the SERC and AEA Culham Laboratory.

Finally, it gives me great pleasure to thank all the friends I have made at St. Andrews, partly for keeping me sane during my research, but mostly just for being there.

Dedication

My parents' support, moral and financial, has been unwavering throughout my studies. As a small token of my gratitude, this thesis is dedicated to them.

Contents

Chapter 1. Introduction.

1.1 Plasmas.

A plasma is an ionised gas, the behaviour of which is dominated by the electromagnetic interactions between its constituent particles. Plasma is probably the dominant form of matter in the universe, since all stars and much interstellar material exist in that state. However, its occurrence on Earth is less common; being restricted to lightning, flames and various man-made plasmas.

The behaviour of plasma is complex and has attracted a great deal of experimental and theoretical investigation. Models which explain a great deal of the experimental observations have been developed. It is necessary to make certain simplifying assumptions when modelling a plasma. To determine the motion of every particle from the inter-particle forces is, of course, impractical. The next most accurate approach is a statistical description based on distribution functions which describe the density of particles in position and velocity space. Although this approach successfully explains much plasma behaviour, it is impractical to apply it to most problems. In particular, the complex geometries encountered in many applications render such an approach infeasible.

1.2 Magnetohydrodynamics.

The approach which we shall use exclusively in this work is the so-called magnetohydrodynamic model (universally referred to as MHD). As the name suggests, this is a combination of the basic laws of electromagnetism with those of fluid dynamics. In MHD, we assume that the plasma can be described in terms of macroscopic quantities such as temperature and density, defined as averages over fluid elements which are small in comparison to length scales of interest for the macroscopic behaviour of the plasma. These elements must, however, be large in comparison to the length scales of microscopic phenomena. Important examples of microscopic

scales are the Debye length, which is the distance over which the electric field of an individual charged particle is screened out, and the ion gyro radius, which is the radius of the orbit which an ion makes around any magnetic field in the plasma. Clearly then, all length scales of interest must be very much larger than these microscopic scales. In order to apply the normal laws of thermodynamics, the plasma should be highly collisional. For many applications, this last constraint is not satisfied. However, the restriction of particle movement across field lines has the effect of enlarging the range of applicability of the MHD approach.

1.3 The MHD equations.

The behaviour of electric and magnetic fields are described by Maxwell's equations:

$$\nabla.\mathbf{B} = 0 \tag{1.1}$$

$$\nabla \times \mathbf{B} = \mu\mathbf{J} + \frac{1}{\mu\varepsilon}\frac{\partial \mathbf{E}}{\partial t} \tag{1.2}$$

$$\nabla \times \mathbf{E} = -\frac{\partial \mathbf{B}}{\partial t} \tag{1.3}$$

$$\nabla.\mathbf{E} = \frac{\rho_c}{\varepsilon} \tag{1.4}$$

E and **B** are the electric and magnetic fields respectively (**B** is, strictly speaking, the magnetic induction; however, we shall adopt the normal practice of referring to it as the field), μ and ε are the permeability and permittivity, usually assumed to be constant and equal to their free space values, and **J** and ρ_c are the current and charge densities. The relativistic term $(\mu\varepsilon)^{-1}\partial E/\partial t$ in (1.2) can be neglected when particle velocities are much less than the speed of light, which is true for most applications (including all those which we shall discuss).

Ohm's Law,

$$\mathbf{J} = \sigma(\mathbf{E} + \mathbf{v} \times \mathbf{B}) \tag{1.5}$$

gives us the current density driven by the electric and magnetic fields in a plasma of conductivity σ moving with velocity $\mathbf{v}$. More general forms of this law are available, but these shall not be required in our analysis. We may eliminate $\mathbf{E}$ and $\mathbf{J}$ from equations (1.2) (neglecting the relativistic term), (1.3) and (1.5) to obtain the induction equation,

$$\frac{\partial \mathbf{B}}{\partial t} = \nabla \times (\mathbf{v} \times \mathbf{B}) - \nabla \times (\eta \nabla \times \mathbf{B}) \qquad (1.6)$$

which describes the evolution of the magnetic field without explicit reference to current or electric field. η, the magnetic diffusivity, is defined by

$$\eta = \frac{1}{\mu\sigma} \qquad (1.7)$$

If η is constant, we may re-arrange (1.6) into its more familiar form

$$\frac{\partial \mathbf{B}}{\partial t} = \nabla \times (\mathbf{v} \times \mathbf{B}) + \eta \nabla^2 \mathbf{B} \qquad (1.8)$$

In most plasma of interest, the second term on the RHS of (1.8) is very much smaller than the first term. Consequently, the behaviour of the plasma is dominated by the first term, which dictates that the field is convected by the fluid. Alternatively, we may state that the plasma is confined by the field. The tendency of the field to diffuse slowly through the plasma (or vice-versa) is represented by the second term. Neglect of this term gives the model known as ideal MHD. In ideal MHD, field lines may not reconnect and energy is not dissipated. Hence, a great deal of physics resides in the smaller 'resistive' term. More will be said of this in Chapter 2.

To complete our description of the plasma, we require some elementary fluid equations. The equation of mass conservation is

$$\frac{D\rho}{Dt} + \rho \nabla.\mathbf{v} = 0 \qquad (1.9)$$

where ρ is the (mass) density of the plasma and D/Dt is the convective derivative defined by

$$\frac{D}{Dt} = \frac{\partial}{\partial t} + \mathbf{v}.\nabla \qquad (1.10)$$

For changes which progress more slowly than the time it takes sound to cross the plasma, we may assume that motion is incompressible, i.e.

$$\nabla.\mathbf{v} = 0 \tag{1.11}$$

Most importantly, the equation of motion of the plasma is (assuming inviscid flow)

$$\rho \frac{D\mathbf{v}}{Dt} = \mathbf{J} \times \mathbf{B} - \nabla p + \mathbf{F_e} \tag{1.12}$$

where p is the plasma pressure and $\mathbf{F_e}$ represents external forces such as gravity.

The fluid pressure is determined by an equation of state, which we shall take to be that of an ideal gas, i.e.

$$p = \rho \frac{k}{m} T \tag{1.13}$$

where m is the mean particle mass, k is Boltzmann's constant and T is the temperature.

When a flow is compressible, an energy equation is required to relate the pressure and the density of the fluid. In the case of an ideal gas, this may be expressed as

$$\frac{\rho^{\gamma}}{\gamma - 1} \frac{D}{Dt}\left(\frac{p}{\rho^{\gamma}}\right) = -L \tag{1.14}$$

where the energy loss function L represents the energy lost by the fluid. γ is the ratio of specific heats, which is 5/3 for an ideal monatomic gas. Where there is no exchange of heat, the flow is described as adiabatic and the RHS of (1.14) is zero. Hence, the energy equation for an adiabatic process is

$$\frac{D}{Dt}\left(\frac{p}{\rho^{\gamma}}\right) = 0 \tag{1.15}$$

Another special case is an isothermal process (one in which there are no changes in temperature). In this case, (1.13) tells us that

$$\frac{p}{\rho} = \text{a constant} \tag{1.16}$$

1.4 Magnetohydrostatics.

If the external forces in (1.12) are just a gravitational field $\rho\mathbf{g}$ and there are no flows, we have a state of magnetohydrostatic

equilibrium governed by

$$\mathbf{J} \times \mathbf{B} - \nabla p + \rho \mathbf{g} = 0 \tag{1.17}$$

Let us compare the magnitude of the terms in this equation. Consider first the hydrostatic balance (no magnetic forces) between the pressure and a gravitational force ρg acting in the negative z-direction of a cartesian system. From (1.17) and (1.12), we obtain

$$\frac{dp}{dz} = -\rho g = -\frac{mg}{kT} p \tag{1.18}$$

which has solution (T constant)

$$p(z) = p(0) \exp\left(\frac{-mgz}{kT}\right) \tag{1.19}$$

Hence, the pressure falls off by a factor e over a vertical distance equal to the scale height H, defined by

$$H = \frac{kT}{mg} \tag{1.20}$$

Comparing the orders of magnitude of the pressure and gravity terms in (1.17), we find

$$\frac{\nabla p}{\rho g} \approx \frac{p_o/L}{\rho_o g} = \frac{H}{L} \tag{1.21}$$

where L is the length scale of our structure and p_o and ρ_o are the average pressure and density. Hence, we may neglect gravity where $L << H$. In this case, (1.17) becomes

$$\mathbf{J} \times \mathbf{B} = \nabla p \tag{1.22}$$

The ratio of fluid pressure to magnetic pressure is equal to the plasma beta β, defined by

$$\beta = \frac{2\mu p}{B^2} \tag{1.23}$$

Where $\beta << 1$, we may neglect the pressure term in (1.22) and consider a force-free field, satisfying

$$\mathbf{J} \times \mathbf{B} = 0 \tag{1.24}$$

B must satisfy (1.1) and **J** is given by (1.2) as

$$\mathbf{J} = \frac{\nabla \times \mathbf{B}}{\mu} \tag{1.25}$$

where we have, as discussed above, neglected the relativistic term. Since μ is constant in this work, we shall normally omit it from our equations.

1.5 Coronal Loops.

A very important example of a plasma is the sun, which is simply a huge (radius = 6.96×10^8m; mass = 1.99×10^{30}kg) ball of plasma, held together by its own gravity. The surface and atmosphere of the sun display many fascinating and complex structures, in which the role of magnetic fields is central. The atmosphere, known as the corona, has a high temperature (1.6×10^6K in the 'quiet corona') and a low density (10^{12}m^{-3} at one solar radius above the surface and falling off rapidly with height). The mechanism by which this temperature is obtained is a long-standing problem in solar physics. X-ray and EUV observations of the corona have revealed the presence of coronal holes - areas of open magnetic field, which have especially low density. Elsewhere, these observations indicate that the corona consists largely of loop structures, which are presumed to outline the magnetic field. These loops are categorised into five main types, the properties of which are given in the following table:

Type	Length (Mm)	Temperature (K)	Density (m^{-3})
Active-Region	10-100	10^4-2.5×10^6	$(0.5\text{-}5) \times 10^{15}$
Interconnecting	20-700	$(2\text{-}3) \times 10^6$	7×10^{14}
Post-Flare	10-100	10^4-4×10^6	10^{17}
Quiet-Region	20-700	1.8×10^6	$(0.2\text{-}1.0) \times 10^{15}$
Simple-Flare	5-50	$\leq 4 \times 10^7$	$\leq 10^{18}$

To understand this classification, it is necessary to consider the sun's visible surface, which is known as the photosphere. The regions of the photosphere where most magnetic activity takes place are termed 'active', the opposite of this term being 'quiet'. The characteristic features of an active region are intense magnetic fields, sunspots, complex overlying magnetic field structures and the occurrence of flares. Sunspots are cooler (hence, darker) regions of the photosphere, with very strong magnetic fields (2-3000G).

Solar flares are violent magnetic storms, visible as a rapid localised brightening in the photosphere. This is often accompanied by effects in the rest of the spectrum and the emission of particles or blobs of plasma. The brightening is thought to be a response to events happening in the overlying coronal field. Flares are divided into two types. The compact flare is a simple brightening and fading in one or more loops. Such loops are referred to as simple-flare loops. The two-ribbon flare is larger in extent and more energetic. The name comes from the two ribbons of H_α (photospheric) emission which are seen in this type of flare. These ribbons are often seen to be connected by a 'post-flare loop'.

An 'interconnecting loop' is one which connects two distinct active regions; the terms 'active region loop' and 'quiet region loop' should be self-explanatory.

In this work we shall examine the structure of the coronal loop, considered as a tube of magnetic flux with its ends rooted in the dense plasma of the photosphere. Since the bulk of the loop is in the corona, its structure is dominated by the magnetic field. The loop evolves through a series of equilibria in response to the movement of its photospheric footpoints. In chapters 4 and 5, we shall examine this evolution when the motion of the footpoints is twisting and when pressure fluctuations occur at the base of the loop. In Chapter 4, the linear behaviour will be studied, whereas Chapter 5 will investigate the non-linear regime and the possibility of loss of equilibrium. A more detailed introduction to solar MHD can be found in the book by Priest (1982).

1.6 Controlled Nuclear Fusion.

The sun's gravity compresses and heats the plasma at its centre to such an extent that nuclear fusion takes place, converting hydrogen into helium and releasing energy. It is this process which is primarily responsible for the sun's energy output. Reproduction of

this process on Earth would constitute an extremely important energy source. Unfortunately, in order to confine the plasma, some alternative to the sun's gravity must be found. The most promising approach so far devised has been magnetic confinement, based on the fact that plasma only diffuses slowly across a magnetic field.

The tokamak, pioneered in the USSR, is the most favoured type of magnetic confinement device. In the tokamak, a large toroidal magnetic field with a small poloidal component is used to confine plasma within a toroidal vessel. The equilibrium of such a plasma is studied in detail in Chapter 2.

The quest for fusion power has led to the discovery of a plethora of plasma instabilities, many of which can be explained by MHD. Particularly important are the resistive instabilities known as the tearing modes. Tearing modes are described in Chapter 2 and their behaviour in tokamaks is investigated in Chapter 3.

A detailed introduction to the role of plasma physics in the controlled fusion programme can be found in the book edited by Gill (1981).

1.7 Motivation and Outline of Thesis.

In Chapter 2, we shall introduce the ideas necessary to our study of tokamak stability. First, we construct a toroidal co-ordinate system, based on the flux surfaces of an axisymmetric equilibrium field. We shall expand the equilibrium equation in different orders of the inverse aspect ratio, with the ordering of field components appropriate to a tokamak. Our field is cylindrical to leading order, with toroidal curvature appearing as a small effect. Thus, we confirm the results of previous workers and establish the notation to be used in Chapter 3. The second part of Chapter 2 provides an introduction to the tearing mode and reviews previous work on the mode in slab and cylindrical geometries.

In Chapter 3, we construct the marginally stable ideal MHD

equation in the co-ordinate system developed in Chapter 2. We then specialise this equation to the case when three tearing modes are coupled in a non-circular cylinder. Finally, we solve the resulting system of equations for the case when only two modes have singular surfaces in the plasma.

The remaining chapters deal with the coronal loop. In Chapter 4, we study the linear effect of twisting on an initially untwisted coronal loop. We observe the characteristic features of twisted cylindrical equilibria and develop a 1-D model appropriate to long loops, which are nevertheless line-tied at the photosphere.. Since coronal loops generally have a high aspect ratio (about 10), we believe this to be a useful approach. Elementary observations are made about the effects of toroidicity, comparing our coronal loop to the tokamak equilibria considered in previous chapters.

Using the 1-D model of Chapter 4, Chapter 5 investigates the non-linear regime in a search for loss of equilibrium, which might explain the heating of the corona or the occurrence of compact flares. Different approaches to the specification of twist and pressure enhancements are examined and compared. Extensive comparisons with 2-D work are made.

Chapter 2. Toroidal Equilibria and Tearing Modes

2.1 Tokamaks.

The tokamak is a toroidal plasma confinement device which has a large toroidal magnetic field B_t and a smaller poloidal magnetic field B_p. The ratio of the major radius of the torus to its minor radius is known as the aspect ratio.

An important quantity in tokamak stability theory is the safety factor q, which is the ratio of the pitch of a magnetic field line to the major radius of the torus. Hence, a field line will make q toroidal transits of its flux surface in one poloidal transit. In a tokamak, q normally rises monotonically from a minimum value q_0 at the magnetic axis to a maximum q_a at the plasma surface. The plasma beta which measures the
ratio of fluid pressure to magnetic pressure is given by

$$\beta = 2\mu_o p/B^2 \qquad (2.1)$$

The plasma beta in a tokamak is rather small, though the poloidal beta (obtained by replacing B by B_p in equation (2.1)) is usually of order 1.

2.2 Toroidal Co-ordinate Systems.

In order to facilitate the study of toroidal pinch devices, such as the tokamak and the reverse field pinch, various authors (Hamada (1962), Greene et al (1971), Bussac et al (1975)) have developed co-ordinate systems based on the magnetic flux surfaces of toroidally axisymmetric equilibria. These co-ordinate systems have the added advantage of making field lines appear straight. As a consequence of toroidicity, the flux surfaces are not concentric circles, but their centres are displaced outwards from the magnetic axis by an amount Δ, known as the Shafranov shift. Here we follow Connor and Hastie (1985) in constructing a system based on flux

surfaces which display both the Shafranov shift and the non-circular distortion of flux surfaces which may be created by external current windings or an appropriately shaped conducting shell. Such co-ordinate systems may also be useful in modelling magnetic structures in the solar corona. For instance, the coronal loop is a semi-toroidal structure with a large aspect ratio (typically 10). Furthermore, reversals in their toroidal field are not observed, suggesting that the poloidal field is small in comparison to the toroidal component. Hence, a tokamak expansion should be an appropriate description of such a loop.

First, we transform from the cylindrical co-ordinate system (R,ϕ,Z) centred on the axis of toroidal symmetry to a system (ρ,ω,ϕ) in which ρ labels flux surfaces and ω is an angle-like variable in the poloidal direction. ρ and ω are not orthogonal. The co-ordinate systems are shown in Figure 2.1.

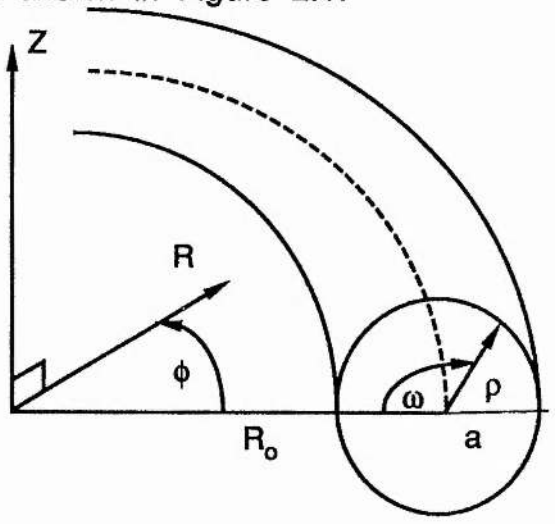

Fig 2.1 Toroidal co-ordinates.

We shall define a transformation

$$R = R(\rho,\omega) \; ; \; Z = Z(\rho,\omega) \qquad (2.2)$$

and the metric tensor g such that the element of length dl is given by

$$(dl)^2 = g_{\rho\rho}(d\rho)^2 + 2g_{\rho\omega}d\rho d\omega + g_{\omega\omega}(d\omega)^2 + R^2(d\phi)^2 \qquad (2.3)$$

The elements of the metric tensor and the Jacobian of the co-ordinate system J are given by

$$g_{\rho\rho} = (\partial R/\partial\rho)^2 + (\partial Z/\partial\rho)^2 \quad ; \; g_{\omega\omega} = (\partial R/\partial\omega)^2 + (\partial Z/\partial\omega)^2$$

$$g_{\rho\omega} = \partial R/\partial\rho \; \partial R/\partial\omega + \partial Z/\partial\rho \; \partial Z/\partial\omega \; ;$$

$$J = R \; (\partial R/\partial\omega \; \partial Z/\partial\rho - \partial R/\partial\rho \; \partial Z/\partial\omega) \quad . \qquad (2.4)$$

Our stability calculations will require explicit expressions for the scale factors of the system $|\nabla\rho|$, $|\nabla\omega|$ and $\nabla\rho.\nabla\omega$ which are related to the elements of the metric tensor by

$$|\nabla\rho|^2 = g^{\rho\rho} \; ; \; |\nabla\omega|^2 = g^{\omega\omega} \; ; \; \nabla\rho.\nabla\omega = g^{\rho\omega} \quad . \qquad (2.5)$$

The pressure p is a function of ρ alone and the magnetic field takes the form

$$\mathbf{B} = R_0 B_0 \; (f(\rho) \; \nabla\phi \; X \; \nabla\rho \; + \; g(\rho) \; \nabla\phi) \qquad (2.6)$$

where R_0 is the major radius of the torus and B_0 is a constant magnetic field (essentially the toroidal field). f and g are dimensionless functions describing the poloidal and toroidal magnetic field components respectively. The equilibrium equation now becomes (Appendix A)

$$\frac{f}{J}\left[\frac{\partial}{\partial\rho}\left(\frac{f g_{\omega\omega}}{J}\right) - \frac{\partial}{\partial\omega}\left(\frac{f g_{\rho\omega}}{J}\right)\right] + \frac{p'}{R_0^2 B_0^2} + \frac{gg'}{R^2} = 0 \qquad (2.7)$$

where primes denote derivatives with respect to ρ .

We shall now expand our equilibrium quantities in increasing powers of the inverse aspect ratio ε ($= a/R_0$ where a is the minor radius) of the torus. The leading order of our expansion will be equivalent to the straight cylinder, which we use as a first approximation to our tokamak. Corrections to this will appear as higher order terms. In a large aspect ratio tokamak, the poloidal field is of order ε in comparison to the toroidal field, which is given in leading order by the constant field B_0 and the plasma beta is order

ε^2. Inserting this ordering into equation (2.7) implies that g' is of order ε^2 . Summarising,

$$p/B_0^2 = \varepsilon^2 p_2 + \ldots , f = \varepsilon f_1 + \ldots , g = 1 + \varepsilon^2 g_2 + \ldots \quad . \qquad (2.8)$$

We choose the following form for our co-ordinate transformation:

$$R = R_0(1 - \varepsilon\rho\cos\omega - \varepsilon^2\Delta(\rho) + \varepsilon^2\Sigma_n [S^n(\rho)\cos(n-1)\omega] + \varepsilon^3 P(\rho)\cos\omega + \ldots) ;$$

$$Z = R_0(\varepsilon\rho\sin\omega + \varepsilon^2\Sigma_n[S^n(\rho)\sin(n-1)\omega] - \varepsilon^3 P(\rho)\sin\omega + \ldots) \quad . \qquad (2.9)$$

Note that ρ has been non-dimensionalised and that S and P are dimensionless. Thus our magnetic surfaces are non-concentric due to the shift $\Delta(\rho)$ and have non-circular shaping terms given by the S^n (S^2 = ellipticity, S^3 = triangularity, etc.). P merely re-labels the flux surfaces for reasons of mathematical convenience. We will later select a form for P which facilitates a further co-ordinate transformation.

Non-dimensionalising with respect to R_o and B_o and expanding equation (2.7) in powers of ε (Appendix B) yields in highest order:

$$p_2' + g_2' + f_1(\rho f_1)'/\rho = 0 \quad , \qquad (2.10)$$

which is the cylindrical equilibrium equation. Here and subsequently R_o and B_o have been suppressed. The $\cos\omega$ term in the second order equation describes the shift of surfaces:

$$\Delta'' + (2(\rho f_1)'/(\rho f_1) - 1/\rho)\Delta' - 2(\rho f_1)'/f_1 - 1 - 2\rho g_2'/f_1^2 = 0 \qquad (2.11)$$

and the higher harmonics describe the surface shaping:

$$S^{n''} + [2(\rho f_1)'/(\rho f_1) - 1/\rho]S^{n'} - (n^2-1)S^n/\rho^2 = 0 \qquad (2.12)$$

We observe that, unless a non-zero value of $S^n(a)$ is imposed, the solution of this equation is simply $S^n = 0$. In the next order of ε, we obtain:

$$P'' + \left(\frac{2(\rho f_1)'}{\rho f_1} - \frac{1}{\rho} \right) P' + \frac{P}{\rho^2} + \frac{3\rho}{2} + \frac{\Delta'}{2} - \rho\Delta'' - \frac{(\Delta')^2}{2} + \frac{3}{2}\Delta'\Delta''$$

$$+ \frac{1}{f_1^2} \left[p_4' + g_4' + g_2 g_2' + \frac{1}{\rho^2} (\rho^2 f_1 f_3)' + \frac{3}{2}\rho^2 g_2' + 2\Delta g_2' \right] +$$

$$\frac{(\rho f_1)'}{2\rho f_1} \left[3\rho^2 - 4\rho\Delta' + 3(\Delta')^2 + 4\Delta + \sum_n \left((n-1)^2 \frac{(S^n)^2}{\rho^2} - 3(S^{n\prime})^2 \right) \right]$$

$$+ \sum_n \frac{n}{\rho} \left[S^{n\prime} + (n-1)\frac{S^n}{\rho} \right]^2 = 0 \qquad (2.13)$$

where (2.12) has been used to eliminate terms in $S^{n\prime\prime}$.

For convenience in our stability analysis, we shall make a further transformation to the co-ordinates (r,θ) given by

$$r^2 = \frac{1}{\pi} \int_0^\rho d\rho \int_0^{2\pi} \frac{J}{R^2} d\omega \; ; \; \theta = 2\pi \frac{\int_0^\omega \frac{J}{R^2} d\omega}{\int_0^{2\pi} \frac{J}{R^2} d\omega} \qquad (2.14)$$

and we may make r equal to ρ by setting

$$P = \frac{r^3}{8} + r\frac{\Delta}{2} - \sum_n \frac{n-1}{2} \frac{(S^n)^2}{r} \qquad (2.15)$$

thus removing the higher order terms in the integrals. θ is given by

$$\theta = \omega + \varepsilon \left[(\Delta' + r)\sin\omega - \sum_n \frac{1}{n} \left(S^{n\prime} - (n-1)\frac{S^n}{r} \right) \sin(n\omega) \right] + \ldots \qquad (2.16)$$

The scale factors of the (r,θ) system are (neglecting second order harmonic terms which we shall not require)

$$|\nabla r|^2 = 1 - \varepsilon \left[2\Delta' \cos\theta - 2 \sum_n S^{n\prime} \cos(n\theta) \right] +$$

$$\varepsilon^2 \left[\frac{(\Delta')^2}{2} + \frac{3r^2}{4} + \Delta + \frac{1}{2} \sum_n (S^{n\prime})^2 + (n^2-1)\frac{(S^n)^2}{r^2} \right] + \ldots.$$

$$|\nabla\theta|^2 = \frac{\varepsilon^{-2}}{r^2}\left\{1+\varepsilon\left[2(\Delta'+r)\cos\theta - 2\sum_n S^{n'}\cos(n\theta)\right]+\right.$$

$$\varepsilon^2\left[\frac{1}{2}(r\Delta''+2\Delta'+r)(r\Delta''+r)+\frac{3}{2}(\Delta'+r)^2+\Delta+\frac{r^2}{4}+\frac{(\Delta')^2}{2}+\right.$$

$$\sum_n\left(\frac{r^2}{2n^2}(S^{n''})^2+\frac{1}{n^2}rS^{n''}\left((n^2-1)\frac{S^n}{r}+S^{n'}\right)+\frac{3n^2+1}{2n^2}(S^{n'})^2-\right.$$

$$\left.\left.\left.\frac{n^2-1}{2n^2}\frac{(S^n)^2}{r^2}+\frac{n^2-1}{n^2}\frac{S^nS^{n'}}{r}\right)\right]+\ldots\right\}$$

$$\nabla r.\nabla\theta = \left[(\Delta''+\frac{\Delta'}{r}+1)\sin\theta - \sum_n\frac{1}{n}(S^{n''}+\frac{S^{n'}}{r}+\frac{n^2-1}{r^2}S^n)\sin(n\theta)\right]+\ldots$$

$$R^2 = 1-\varepsilon\left[2r\cos\theta\right]-\varepsilon^2\left[2\Delta+r\Delta'+\frac{r^2}{2}\right]+\ldots \qquad (2.17)$$

This co-ordinate system has the advantage that the field lines are straight lines in the θ-ϕ plane. In addition, the safety factor q takes the particularly simple form

$$q = \frac{g}{2\pi f}\int_0^{2\pi}\frac{J}{R^2}d\omega = \frac{gr}{f} \qquad (2.18)$$

and the Jacobian is simply

$$J = rR^2 \qquad (2.19)$$

Of particular importance in tokamaks is the instability known as the tearing mode. This is believed to be involved (see, e.g. Wesson (1981)) in the disruptive instability which results in rapid plasma cooling and current collapse, as well as small magnetic (Mirnov) oscillations and millisecond oscillations in soft x-ray emission (sawtooth oscillations). A general description of the tearing mode follows.

2.3 Tearing Modes.

Consider the induction equation for a plasma of uniform

resistivity η:

$$\frac{\partial \mathbf{B}}{\partial t} = \nabla \times (\mathbf{v} \times \mathbf{B}) + \eta \nabla^2 \mathbf{B} \qquad (2.20)$$

The ratio of the terms on the right-hand side is given,in order of magnitude, by the magnetic Reynolds number $R_M = lv/\eta$ where v is a typical flow speed and l a typical length scale for variations in the plasma. For plasmas of interest in solar and laboratory physics, R_M is normally very large, so that field lines are frozen into the plasma and diffusive effects due to the $\eta \nabla^2 B$ term are negligible in the bulk of the plasma. Whereas ideal instabilities grow on the Alfven timescale $t_A = l/v_A$, resistive diffusion occurs on the much slower diffusive timescale $t_D = l^2/\eta$. The ratio of these times S $(=t_D/t_A)$ is called the Lundquist number and is often used in preference to R_M. However, if sufficiently small lengthscales can be created, the field may diffuse through the plasma locally. In any situation where reconnection occurring in a small region of the plasma can lower the energy of the plasma as a whole, there is the possibility of a non-ideal instability. Hence, resistive instabilities may occur in plasma which is ideally stable, since the constraint that field lines may not reconnect has been removed. In fact, any dissipative mechanism (e.g. viscosity, electron inertia) will permit such instabilities. Such instabilities grow on a hybrid timescale $t_H = t_A(t_D/t_A)^{\alpha}$, $0 < \alpha < 1$.

Of primary interest among such modes is the tearing mode. In this instability, current gradients provide free energy, which may only be released if the topology of the field is allowed to change. The perturbed field reconnects at singular layers where the perturbation causes no local line-bending, forming magnetic islands which grow on a hybrid timescale.

First, we will examine tearing in a slab geometry. We shall

derive an estimate of ε_1 the width of the resistive layer and γ the growth rate of the instability by simple order of magnitude estimates (following Bateman (1978)). Consider a field

$$\mathbf{B}_o = B_{oy}(x)\,\hat{\mathbf{y}} \qquad (2.21)$$

which reverses sign at x=0; the plane x=0 is referred to as a neutral sheet or singular layer. Since the magnetic field is weak in the vicinity of this layer, the stabilising effect of magnetic tension will be reduced there. In our derivation, we shall make the simplifying assumption that the perturbed field and velocity have no component in the z-direction and that all quantities are constant in that direction. We apply a velocity perturbation

$$\mathbf{v}_1 = \left(v_{1x}(x)\cos(ky)\,\hat{\mathbf{x}} + v_{1y}(x)\sin(ky)\,\hat{\mathbf{y}} \right) e^{\gamma t} \qquad (2.22)$$

where k is the wavenumber of the perturbation in the direction parallel to the field. Hence, fluid moves into the neutral sheet from both sides, then the streams collide and move parallel to the sheet, before recoiling and streaming away. This type of flow is characteristic of tearing behaviour. The initial field and the velocity perturbation are shown in Figure 2.2. The parallel flows close to the sheet are not shown.

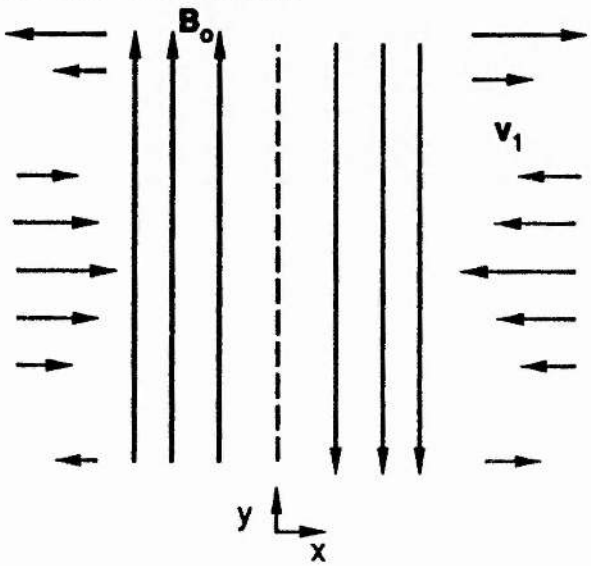

Fig. 2.2 Initial field and tearing flow

Correspondingly, we have a magnetic field perturbation

$$\mathbf{B}_1 = \left(B_{1x}(x)\sin(ky)\,\hat{\mathbf{x}} + B_{1y}(x)\cos(ky)\,\hat{\mathbf{y}} \right) e^{\gamma t} \qquad (2.23)$$

The development of the instability will be determined by the perturbed form of Maxwell's equations

$$\nabla \times \mathbf{B}_1 = \mathbf{J}_1 \tag{2.24}$$

$$\nabla \times \mathbf{E}_1 = -\frac{\partial \mathbf{B}_1}{\partial t} \tag{2.25}$$

$$\nabla . \mathbf{B}_1 = 0 \tag{2.26}$$

Ohm's Law

$$\mathbf{E} = -\mathbf{v} \times \mathbf{B} + \eta \mathbf{J} \tag{2.27}$$

and the equation of motion with one driving term due to the perturbed current

$$\rho \frac{\partial \mathbf{v}_1}{\partial t} = -\mathbf{J}_1 \times \mathbf{B}_o \tag{2.28}$$

We shall neglect less important driving terms due to ∇p_1 and $\mathbf{J}_o \times \mathbf{B}_1$. Since motions are much slower than the sound velocity, density inhomogeneities will be smoothed out, so the motion may be assumed incompressible., i.e.

$$\nabla . \mathbf{v}_1 = 0 \tag{2.29}$$

From (2.23), (2.24) and (2.26) we may deduce the perturbed current

$$J_{1z}(x) = \frac{1}{k} B''_{1x} - kB_{1x} \tag{2.30}$$

and (2.27) gives us the electric field

$$E_{1z} = -v_{1x} B_{oy} + \eta J_{1z} \tag{2.31}$$

From (2.25) we obtain

$$E_{1z} = -\frac{1}{k} \frac{\partial B_{1x}}{\partial t} \tag{2.32}$$

and combining these two equations for E_{1z} gives us the appropriate form of the induction equation

$$\frac{\partial B_{1x}}{\partial t} = k v_{1x} B_{oy} - \eta k J_{1z} = k v_{1x} B_{oy} - \eta \left(B''_{1x} - k^2 B_{1x} \right) \tag{2.33}$$

Since η is small in hot fusion plasmas, the second term on the RHS will be negligible in most of the plasma; the exception being in a thin boundary layer close to $B_{oy} = 0$. Here the value of $\partial^2 B_{1x}/\partial x^2$ will be very large. Consequently, the ideal solution for B_{1x}, which is

appropriate outside the boundary (resistive) layer, will require a discontinuity in its first derivative across the layer. This discontinuity, when normalised by dividing by B_{1x}, gives the important quantity

$$\Delta' = \frac{B'_{1x}(\varepsilon_1) - B'_{1x}(-\varepsilon_1)}{B_{1x}(0)} \qquad (2.34)$$

not to be confused with the derivative of the Shafranov shift. Since the Δ' is obtained purely from the ideal solution in the outer region, it is independent of the model chosen for the resistive layer. Hence, the same ideal solution may be used with layer models of varying sophistication, including additional physical effects. For any given model, we may derive the appropriate inner solution, which gives Δ' as a function of the growth rate . Thus, the growth rate may be obtained from the matching condition

$$\Delta'_{(outer)} = \Delta'_{(inner)}(\gamma) \qquad (2.35)$$

It should be noted that, for simple resistive MHD, the outer solution is sufficient to determine stability, since $\Delta'_{(inner)}(0) = 0$. Modes with $\Delta' > 0$ are unstable, those with $\Delta' < 0$ are stable. This is due to the fact that Δ' has the same sign as the energy released by the field in the outer region. We shall proceed to derive our simple estimates of γ and ε_1, assuming Δ' to be a given quantity obtained from the outer solution. It follows from the above that the typical size of $\partial^2 B_{1x}/\partial x^2$ in the boundary layer is given by

$$B''_{1x} \approx \frac{\Delta' B_{1x}}{\varepsilon_1} \qquad (2.36)$$

Hence, (2.30) gives us

$$J_{1z} \approx \frac{\Delta' B_{1x}}{k\varepsilon_1} \qquad (2.37)$$

The resistive layer is the region where the current and flow terms in the induction equation (2.33) are of comparable importance. It follows that

$$\gamma B_{1x} \approx v_{1x} k B_o \approx \eta k J_{1z} \qquad (2.38)$$

Equating the first and last terms in (2.38) and using (2.37) to eliminate J_{1z}, we have

$$\gamma \approx \frac{\eta \Delta'}{\varepsilon_1} \tag{2.39}$$

To estimate the growth rate, we balance the rate of increase of the kinetic energy in the boundary layer against the rate at which work is done on the fluid by the driving force. The driving force is given by equation (2.28) as

$$\rho \frac{\partial v_{1x}}{\partial t} = -J_{1z} B_o \tag{2.40}$$

which does work

$$\mathbf{v}_1 . \mathbf{F} \approx v_{1x} B_o J_{1z} \approx \frac{v_{1x} B_{1x} B_o \Delta'}{k\varepsilon_1} \tag{2.41}$$

on the fluid, where we have made use of (2.37). The rate of change of kinetic energy is

$$\frac{d(K.E)}{dt} \approx \frac{\gamma p}{2} \left(v_{1x}^2 + v_{1y}^2 \right) \tag{2.42}$$

We assume that the wavelength k^{-1} along the field is very large in comparison to the resistive layer width. Hence, in order to maintain incompressibility, we must have

$$v_{1y} \approx \frac{v_{1x}}{k\varepsilon_1} \gg v_{1x} \tag{2.43}$$

It follows that

$$\frac{d(K.E)}{dt} \approx \frac{\gamma p}{2(k\varepsilon_1)^2} v_{1x}^2 \tag{2.44}$$

Since B_o goes through zero at x=0, we shall estimate its typical magnitude in the layer by

$$B_o \approx B_o' \varepsilon_1 \tag{2.45}$$

Equating (2.41) to (2.44) and using (2.45) to eliminate B_o, we obtain

$$\gamma \approx \frac{2\Delta' B_o' k\varepsilon_1^2 B_{1x}}{\rho v_{1x}} \tag{2.46}$$

which, together with (2.39) gives us γ and ε_1 as

$$\gamma \approx \left(\frac{2(kB_o')^2 \eta^3 \Delta'^4}{\rho} \right)^{\frac{1}{5}} \tag{2.47}$$

and

$$\varepsilon_1 \sim \left(\frac{\rho \Delta' \eta^2}{2(kB_0')^2} \right)^{\frac{1}{5}} \qquad (2.48)$$

Note, in particular, that γ scales as $\eta^{3/5}$, so that the growth of the instability is 3/5 resistive and 2/5 Alfvenic. Also, the width of the layer is very small in comparison to the scale of the plasma as a whole, due to the $\eta^{2/5}$ factor in (2.48). Furth et al. (1963) solved the full eigenvalue problem for Δ' in a slab and gave a more exact analysis of the inner region than that given above. Assuming B_{1x} to be approximately constant in the inner region (the 'constant-Ψ approximation'), they deduced the scaling

$$\gamma \sim t_d^{-\frac{3}{5}} t_a^{-\frac{2}{5}} \qquad (2.49)$$

which agrees with our order of magnitude calculation. (2.49) is valid provided that k is neither so small that B_{1x} cannot be considered constant, nor so large that tension forces stabilise the mode. They also considered the case for which k is very small, finding that the growth rate of the fastest mode scaled as $(t_d t_a)^{-1/2}$. The instability grows fastest with long, narrow islands, which minimise tension stabilisation.

We have described the Δ'-matching/boundary layer method, which has been used extensively in the study of tearing modes. An alternative method is to solve the full resistive equations in the entire volume of the plasma (e.g. Wesson (1966)), without making any assumptions about the boundary layer.

The reconnected magnetic field resulting from the instability is shown in fig. 2.3. Note the formation of magnetic islands and the fact that B_{1x} has the same sign moving perpendicularly across the field structure.

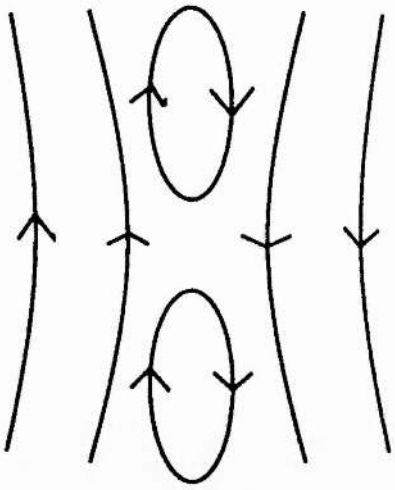

Fig. 2.3 Reconnected Magnetic Field.

Consider now the situation in a tokamak. The tearing modes have a spatial variation given by $f(r)\exp(i(m\theta - n\phi))$, so that each mode is characterised by poloidal and toroidal fourier mode numbers m and n respectively. Tearing modes of number (m,n) occur when their resonant surfaces (at radius r_s where $q(r_s) = m/n$, also known as the mode rational surface) lie inside the plasma. It is at these surfaces that the helical plasma distortions follow the shape of the field lines. In the cylindrical limit, the problem may be solved by a straightforward extension of the slab method, as in Furth et al. (1973). The outer solution is obtained by solving the ideal MHD equation for the perturbed radial field, subject to boundary conditions at the centre and surface of the plasma column. This yields a Δ' at the mode-rational surface, corresponding to that at the neutral sheet in the slab case. For modes with $m \geq 2$, the inner solution behaves like the slab case. However, the fastest-growing mode, having m=1, requires special treatment (e.g. the constant-Ψ approximation is not usually valid.). This mode is more closely related to its ideal counterpart, the m=1 ideal internal kink; the ideal mode is often unstable, which can give rise to an infinite Δ'. The complete dispersion relationship for the m=1 mode, incorporating its ideal and resistive limits, was derived by Coppi et al. (1976). The mode has a much faster growth rate than the $m \geq 2$

tearing modes and is usually unstable if there is a q=1 surface in the plasma.

Another interesting variant of the tearing mode is the double tearing mode, studied by Stix (1976) and Rechester and Stix (1976), where a single mode has two resonant surfaces close to each other in the plasma. This requires a non-monotonic q-profile, caused by skin currents, which sometimes occur in the early phase of tokamak discharges. If the surfaces are close enough together, the magnetic islands can drive each other's growth, resulting in an enhanced growth rate. In such a case, there are large plasma motions everywhere between the islands.

When toroidicity is taken into account, the tearing problem is considerably complicated by the coupling of modes of different m, due to the θ-dependence of the equilibrium fields. We shall address this problem in the next chapter.

The $m \geq 2$ tearing mode grows exponentially at the rate given above until the island width becomes comparable to the resistive layer width. At this stage, the non-linear effects create additional forces, which act against the original plasma perturbation. The islands then continue to grow at a linear rate, until they reach a saturation width of a few-tenths of the plasma radius. White et al. (1977) have shown that the non-linear growth of the island width W is given by

$$\frac{dW}{dt} = 1.66\,\eta\left(\Delta'(W) - \alpha W\right) \qquad (2.50)$$

where $\Delta'(W)$ is taken across the island width instead of the layer width. Thus, the island width grows linearly until αW becomes comparable to $\Delta'(W)$. α must be obtained from the ideal outer solution. The presence of such saturated islands enhances transport processes in the plasma. In the case of the m=1 mode, the island may continue to grow until it has occupied the entire centre of the plasma column. Another non-linear possibility is the coupling of

modes of different m and n at large island sizes. Waddell et al. (1978,1979) have found this effect in numerical simulations, resulting in island growth beyond the saturation value given by (2.50)

The tokamak phenomena mentioned earlier are all believed to be associated with the non-linear results of tearing mode activity. The sawtooth oscillations are thought to be due to the formation and collapse of m=1 islands close to the magnetic axis. The Mirnov oscillations correspond to the movement around the torus of an island formed by a saturated mode with $m \geq 2$. Disruptions develop from m=2 activity, probably involving non-linear coupling to other modes.

Chapter3. Coupled Tearing Modes in Tokamaks

3.1 Introduction and Mathematical Development.

In a planar or cylindrical field configuration, the tearing mode stability problem has been treated successfully by the asymptotic matching (Δ') procedure and also by solution of the full resistive MHD equations. However, in a toroidal geometry, the problem is complicated by the coupling of modes of different poloidal mode number m. A mode m will generate sidebands characterised by m±1. Further, if the magnetic surfaces have non-circular cross-sections, coupling to still other modes can occur. In such more complicated situations, the equivalent of the $\Delta'_{(outer)}$ is a relation between the various Δ'_m at their resonant surfaces (Connor et al. (1988)). We believe this approach to have two advantages over solving the full equations. Firstly, it is difficult for resistive codes to operate at high values of S. Secondly, such codes have limited ability to include more sophisticated layer models than simple resistive MHD.

The first step in our procedure is to construct the marginally stable ideal MHD equations in the (r,θ,ϕ) co-ordinate system developed in the previous chapter.

The linearised marginal ideal MHD equations for an incompressible plasma displacement ξ are:

$$\nabla(\delta p) = \delta \mathbf{J} \times \mathbf{B} + \mathbf{J} \times \delta \mathbf{B} \tag{3.1}$$

$$\delta \mathbf{J} = \nabla \times \delta \mathbf{B} \tag{3.2}$$

$$\delta p = -\xi . \nabla p \tag{3.3}$$

$$\nabla . \delta \mathbf{B} = 0 \tag{3.4}$$

where p, **J** and **B** are the equilibrium pressure,current and magnetic field respectively and δp, $\delta \mathbf{J}$ and $\delta \mathbf{B}$ are the corresponding perturbed quantities. Assuming the perturbed quantities are proportional to

$e^{-in\phi}$, we may eliminate δB_r and δB_θ from (3.1)-(3.4), obtaining (Appendix C) the two coupled equations

$$\frac{\partial}{\partial r}\left[\left(\frac{\partial}{\partial\theta} - inq\right)y\right] = \frac{\partial}{\partial\theta}\left(Q\frac{\partial z}{\partial\theta}\right) + Sz - \frac{\partial}{\partial\theta}\left[T\left(\frac{\partial}{\partial\theta} - inq\right)y + Uy\right] \quad (3.5)$$

and

$$\left(\frac{\partial}{\partial\theta} - inq\right)\frac{\partial z}{\partial r} = -\left(\frac{\partial}{\partial\theta} - inq\right)T^*\frac{\partial z}{\partial\theta} + U\frac{\partial z}{\partial\theta} - \left(\frac{\partial}{\partial\theta} - inq\right)V\left(\frac{\partial}{\partial\theta} - inq\right)y$$

$$+ W\left(\frac{\partial}{\partial\theta} - inq\right)y + Xy \quad (3.6)$$

where the dependent variables are $y = f\xi^r$ and $z = R^2\delta B^\phi$. Q, S, T, U, V, W and X are the equilibrium quantities (T^* is the complex conjugate of T):

$$Q = \frac{1}{inr|\nabla r|^2}\ ;\ S = inr\ ;\ T = \frac{\nabla r.\nabla\theta}{|\nabla r|^2} - \frac{1}{inr|\nabla r|^2}\frac{g'}{f}\ ;\ U = \frac{R^2}{|\nabla r|^2}\frac{p'}{f^2}\ ;$$

$$V = \frac{1}{r|\nabla r|^2}\left[\frac{in}{R^2} + \frac{1}{in}\left(\frac{g'}{f}\right)^2\right]\ ;\ W = 2\frac{g'}{f}\frac{p'}{f^2}\frac{R^2}{|\nabla r|^2} - \frac{d}{dr}\left(\frac{g'}{f}\right)\ ;$$

$$X = inr\frac{p'}{f^2}\left[\frac{\partial}{\partial\theta}\left(T^*R^2\right) + \frac{\partial}{\partial r}\left(R^2\right) - R^2\frac{r}{f}\frac{d}{dr}\left[\frac{f}{r}\right]\right] \quad (3.7)$$

In a circular cylinder, modes depending on $e^{im\theta}$ are eigenmodes and it is, therefore, straightforward to solve (3.5) and (3.6) in this limit. However, in the more general equilibrium developed in the previous chapter, modes of different m are coupled by the θ-dependence of the scale factors. If we Fourier analyse (3.5) and (3.6) in the poloidal direction, we obtain the infinite set of coupled equations:

$$\frac{\partial}{\partial r}\left[(m-nq)y_m\right] = \sum_{j=-\infty}^{\infty} A_m^j\, y_j + B_m^j\, z_j \quad (3.8)$$

$$\frac{\partial z_m}{\partial r} = \sum_{j=-\infty}^{\infty} C_m^j\, y_j + D_m^j\, z_j \quad (3.9)$$

In the large aspect ratio expansion developed in the previous chapter, coupling to modes $j \neq m$ is of order ε. Hence, we expect a

principal mode m to generate sidebands of order ε. These sidebands will then couple back to the principal mode with an effect of $O(\varepsilon^2)$. We may, thus, examine the effect of toroidicity on a mode m up to $O(\varepsilon^2)$, by including $O(\varepsilon)$ terms in $A^j{}_m$, etc. ($j \neq m$) and $O(\varepsilon^2)$ corrections to $A^m{}_m$, etc. If we refrain from imposing shaping terms, then the only coupling to this order is that to modes m±1. (The effect on the central mode of modes m±2 coupling to m±1 is negligible.) Previous authors (Carreras et al. (1981), Izzo et al. (1985), Connor et al. (1988)) have examined the effect of this coupling between a mode m and its adjacent modes m±1, due to the Shafranov Shift Δ and the toroidal curvature. We shall, instead, concentrate on the effect of non-circularity, assuming our equilibrium to have just one shaping term $S^{(k)}$. In effect, we are neglecting the toroidal curvature of our tokamak (treating it as a straight cylinder) in order to isolate the effect of its non-circular cross-section. The parameter ε now represents the degree of ellipticity, triangularity , etc. of our tokamak. In this case, a mode m is coupled to modes m±k. The scale factors of our chosen equilibrium are

$$|\nabla r|^2 = 1 + \varepsilon\left[2S'\cos(k\theta)\right] + \varepsilon^2\left[\frac{(S')^2}{2} + (k^2-1)\frac{S^2}{2r^2}\right];$$

$$|\nabla\theta|^2 = \frac{\varepsilon^{-2}}{r^2}\left\{1 + \varepsilon\left[-2S'\cos(k\theta)\right] + \varepsilon^2\left[\frac{r^2}{2k^2}(S'')^2 + \right.\right.$$

$$\left.\left.\frac{r}{k^2}S''\left((k^2-1)\frac{S}{r} + S'\right) - \frac{k^2-1}{2k^2}\frac{S^2}{r^2} + \frac{k^2-1}{k^2}\frac{SS'}{r}\right]\right\};$$

$$\nabla r.\nabla\theta = \left[-\frac{1}{k}\left(S'' + \frac{S'}{r} + \frac{k^2-1}{r^2}S\right)\sin(k\theta)\right];$$

$$R^2 = 1 \qquad (3.10)$$

where the superscript k has been dropped for legibility. Equations (3.5) and (3.6) become the set of six coupled equations consisting of

$$\frac{d\Psi_m}{dr} = \frac{m^2 A}{nr} z_m - \varepsilon \frac{m}{nr} S' \left[(m-k)\, z_{m-k} + (m+k)\, z_{m+k} \right] +$$

$$\left[\frac{g'}{nr\, f} (m - nq) - \frac{p'}{f^2} \right] \frac{Am\Psi_m}{m - nq} +$$

$$\varepsilon \left[\left(\frac{B}{2} - \frac{g'}{nr\, f} S' \right) (m - k - nq) + S' \frac{p'}{f^2} \right] \frac{m\Psi_{m-k}}{m - k - nq} +$$

$$\varepsilon \left[- \left(\frac{B}{2} + \frac{g'}{nr\, f} S' \right) (m + k - nq) + S' \frac{p'}{f^2} \right] \frac{m\Psi_{m+k}}{m + k - nq} \qquad (3.11)$$

and

$$\frac{dz_m}{dr} = \left[\frac{p'}{f^2} - \frac{g'}{nr\, f} (m - nq) \right] \frac{Amz_m}{m - nq} +$$

$$\varepsilon \left[\left(\frac{g'}{nr\, f} S' + \frac{B}{2} \right) (m - nq) - \frac{p'}{f^2} S' \right] \frac{m-k}{m - nq} z_{m-k} +$$

$$\varepsilon \left[\left(\frac{g'}{nr\, f} S' - \frac{B}{2} \right) (m - nq) - \frac{p'}{f^2} S' \right] \frac{m+k}{m - nq} z_{m+k} +$$

$$\left[\left(\frac{n}{r} - \frac{1}{nr} \left(\frac{g'}{f} \right)^2 \right) A (m - nq)^2 + \left(2 \frac{g'}{f} \frac{p'}{f^2} A - \frac{d}{dr} \left(\frac{g'}{f} \right) \right) (m - nq) \right.$$

$$\left. - \frac{nrp'}{f^2} \left(\frac{r}{f} \frac{d}{dr} \left(\frac{f}{r} \right) + \frac{p'}{f^2} A \right) \right] \frac{\Psi_m}{(m - nq)^2}$$

$$+ \varepsilon \left[\left(\left(- \frac{n}{r} S' + \frac{S'}{nr} \left(\frac{g'}{f} \right)^2 \right) (m - nq) - 2 \frac{g'}{f} \frac{p'}{f^2} S' \right) (m - k - nq) + \right.$$

$$\left. \frac{nrp'}{f^2} \left(\frac{p'}{f^2} S' - B \right) - 2S' \frac{g'}{f} \frac{p'}{f^2} \right] \frac{\Psi_{m-k}}{(m - k - nq)\,(m - nq)}$$

$$+\varepsilon\left[\left(\left(-\frac{n}{r}S'+\frac{S'}{nr}\left(\frac{g'}{f}\right)^2\right)(m-nq)-2\frac{g'}{f}\frac{p'}{f^2}S'\right)(m+k-nq)+\right.$$

$$\left.\frac{nrp'}{f^2}\left(\frac{p'}{f^2}S'-B\right)+2S'\frac{g'}{f}\frac{p'}{f^2}\right]\frac{\Psi_{m+k}}{(m+k-nq)(m-nq)} \qquad (3.12)$$

and the four equations obtained by replacing m in the above by m±k and dropping terms in $\Psi_{m\pm2k}$, $z_{m\pm2k}$, since their effect on the central mode is negligible. $\Psi_m = (m-nq)y_m$ is the perturbed poloidal flux function and we have defined for brevity:

$$A = 1+\varepsilon\left(\frac{3}{2}(S')^2-\frac{(k^2-1)}{2}\frac{S^2}{r^2}\right);\quad B=\frac{1}{k}\left(S''+\frac{S'}{r}+(k^2-1)\frac{S}{r^2}\right) \qquad (3.13)$$

(3.11) and (3.12) simplify considerably when we neglect pressure, becoming

$$\frac{d\Psi_m}{dr}=\frac{m^2A}{nr}z_m-\varepsilon\frac{m}{nr}\left[(m-k)z_{m-k}+(m+k)z_{m+k}\right]+\frac{g'mA}{nrf}\Psi_m$$

$$+\varepsilon\left(\frac{B}{2}-\frac{g'}{nrf}S'\right)m\Psi_{m-k}-\varepsilon\left(\frac{B}{2}+\frac{g'}{nrf}S'\right)m\Psi_{m+k} \qquad (3.14)$$

and

$$\frac{dz_m}{dr}=-\frac{g'mA}{nrf}z_m+\varepsilon\left(\frac{g'}{nrf}S'+\frac{B}{2}\right)(m-k)z_{m-k}+$$

$$\varepsilon\left(\frac{g'}{nrf}S'-\frac{B}{2}\right)(m+k)z_{m+k}+\left[\left(\frac{n}{r}-\frac{1}{nr}\left(\frac{g'}{f}\right)^2\right)A-\frac{d}{dr}\left(\frac{g'}{f}\right)\frac{1}{m-nq}\right]\Psi_m$$

$$+\varepsilon\left(-\frac{n}{r}S'+\frac{S'}{nr}\left(\frac{g'}{f}\right)^2\right)\left[\Psi_{m-k}+\Psi_{m+k}\right] \qquad (3.15)$$

3.2 Tearing at Two Singular Surfaces.

When there is more than one mode with a singular surface in the plasma, the equivalent of the Δ' is a relationship between the various Δ'_m, where Δ'_m is the jump in the logarithmic derivative of Ψ_m at the m singular surface. The simplest case is an equilibrium containing only two singular surfaces, corresponding to modes m and

m+k, when the relationship represents a hyperbola in the Δ'_m-Δ'_{m+k} plane, given by

$$\left(\Delta'_m - \alpha\right)\left(\Delta'_{m+k} - \beta\right) = \lambda \qquad (3.16)$$

Clearly, the asymptotes of the hyperbola are the lines $\Delta'_m = \alpha$ and $\Delta'_{m+k} = \beta$, while λ is a measure of the curvature of the hyperbola. The three quantities α,β and λ, derived from the ideal MHD solutions, are the equivalent of the single quantity Δ' in the slab or circular cylinder cases.

The growth rate is given by the intersection of this curve with another derived from a resistive layer model

$$\Delta'_m = F_1(\gamma) \; ; \; \Delta'_{m+k} = F_2(\gamma) \qquad (3.17)$$

Since γ is the same for all components of a coupled mode, it parametrises a curve in Δ'_m-Δ'_{m+k} space. It is an advantage of this method of solution, that, having obtained α, β and λ, we may study different physical effects in the resistive layer by matching to corresponding functions F_1, F_2. In particular, note that the effect of toroidal curvature on the resistive layer physics is generally stabilising (Glasser et al.(1975)).

However, it should be noted that the stability condition in simple resistive MHD is that the hyperbola does not enter the first quadrant. This condition is satisfied if and only if all of the following hold:

$$\alpha < 0, \; \beta < 0, \; \alpha\beta - \lambda > 0 \qquad (3.18)$$

3.3 Method of Solution.

In order to solve equations (3.14) and (3.15), the package RDILP (Resistive Diffuse Linear Pinch), originally written by P.Kirby of Culham Laboratory, was modified. RDILP uses the NAG routine D02RAF, which solves ODE's by the adaptive finite difference method of Lentini and Pereyra (1977). This method solves boundary value problems by finite differences, using a mesh which may be modified during solution. Extra mesh points are chosen to distribute

the local truncation error approximately equally over the mesh. This has the effect of making the mesh finer in regions of difficulty. Hence, for our problem, we would expect more points to be added near to the singular surfaces. The equations were solved in 3 separate regions, separated by the two singular surfaces. Since the equations are singular at r=0, a false origin δ was used. A value of $\delta=10^{-3}$ was used, since this value was found to give negligibly different results from $\delta=10^{-5}$. The solutions were converged to a distance δ_1 from the singular surfaces. Hence, the 3 regions of solution were:

$$1: \delta \le r \le r_m-\delta_1 \; ; \; 2: r_m+\delta_1 \le r \le r_{m+k}-\delta_1 \; ; \; 3: r_{m+k}+\delta_1 \le r \le 1 \qquad (3.19)$$

Each of these regions was mapped onto [0,1] and the NAG routine was given a 19th order system to solve on this interval. The Ψ_i were taken to be continuous across the singular surfaces, but z_m and z_{m+k} were allowed to be discontinuous at their respective singular surfaces. The ratio $\Delta'_m : \Delta'_{m+k}$ was set and the Δ'_{m+k} calculated as an eigenvalue, generating a point on the hyperbola on each run. The remaining boundary conditions imposed were that each of the Ψ_i should be zero at r=0 and r=1 (i.e. conducting wall limited plasma) and the normalisation $z_m = -1$ at r=1. The equilibrium was specified by an analytic form of the function q(r), from which the various quantities g'/f etc. were derived. For the shaping terms, the surface value of S was set equal to unity and equation (2.12) was solved using the boundary value method to obtain a numerical grid of S values.

3.4 Results.

Initially, we examined the the 2-parameter class of q-profiles

$$q = (\mu+1)\, q_o \left(1 - \left(1 - r^2 \right)^{\mu+1} \right)^{-1} \qquad (3.20)$$

where μ and q_o are the parameters. Initial results (using $\delta_1=10^{-4}$ and

typically 200 points in each region) showed that α and β were close to the uncoupled values of Δ'_m and Δ'_{m+k}, while λ increased roughly as ε^2. As an example, consider the case q_o=2.1 and μ=2.5, for which the radial profiles of q and the derivative of the axial current are shown in fig. 3.1. The singular surfaces for the modes (4,1) and (6,1) are r_4=0.703 and r_6=0.902. The uncoupled Δ's are Δ'_4= -6.5 and Δ'_6= -16.3. The corresponding uncoupled eigenfunctions are shown in figures 3.2 and 3.3. When these modes were coupled by elliptic (k=2) shaping, the following results were obtained:

Values of Δ'_6. $\varepsilon =$	0.1	0.2	0.3
Δ'_4/Δ'_6			
0.1	-16.3	-72.9	-79.8
0.5	-16.1	-37.6	-42.2
0.75	-17.4	-20.2	-23.8
1.0	-16.8	-18.3	-21.1
2.0	-16.7	-17.9	-20.4
5.0	-16.6	-17.8	-20.1
10.0	-16.6	-17.7	-20.0

The eigenfunctions for various values of ε and Δ'_4/Δ'_6 are shown in Figs. 3.4-3.8. Note that all modes shown are stable, as indicated by the upward pointing 'corners' on Ψ_4 and Ψ_6 at their respective singular surfaces. The corresponding information for the hyperbolae is:

ε	α	β	λ	$\alpha\beta-\lambda$
0.1	-6.7	-16.6	1.7	109.5
0.2	-7.2	-17.7	7.3	120.1
0.3	-7.7	-19.9	16.6	136.6

The hyperbolae are shown in Figs. 3.9-3.11, where crosses are points used to determine the hyperbola and circles have been used

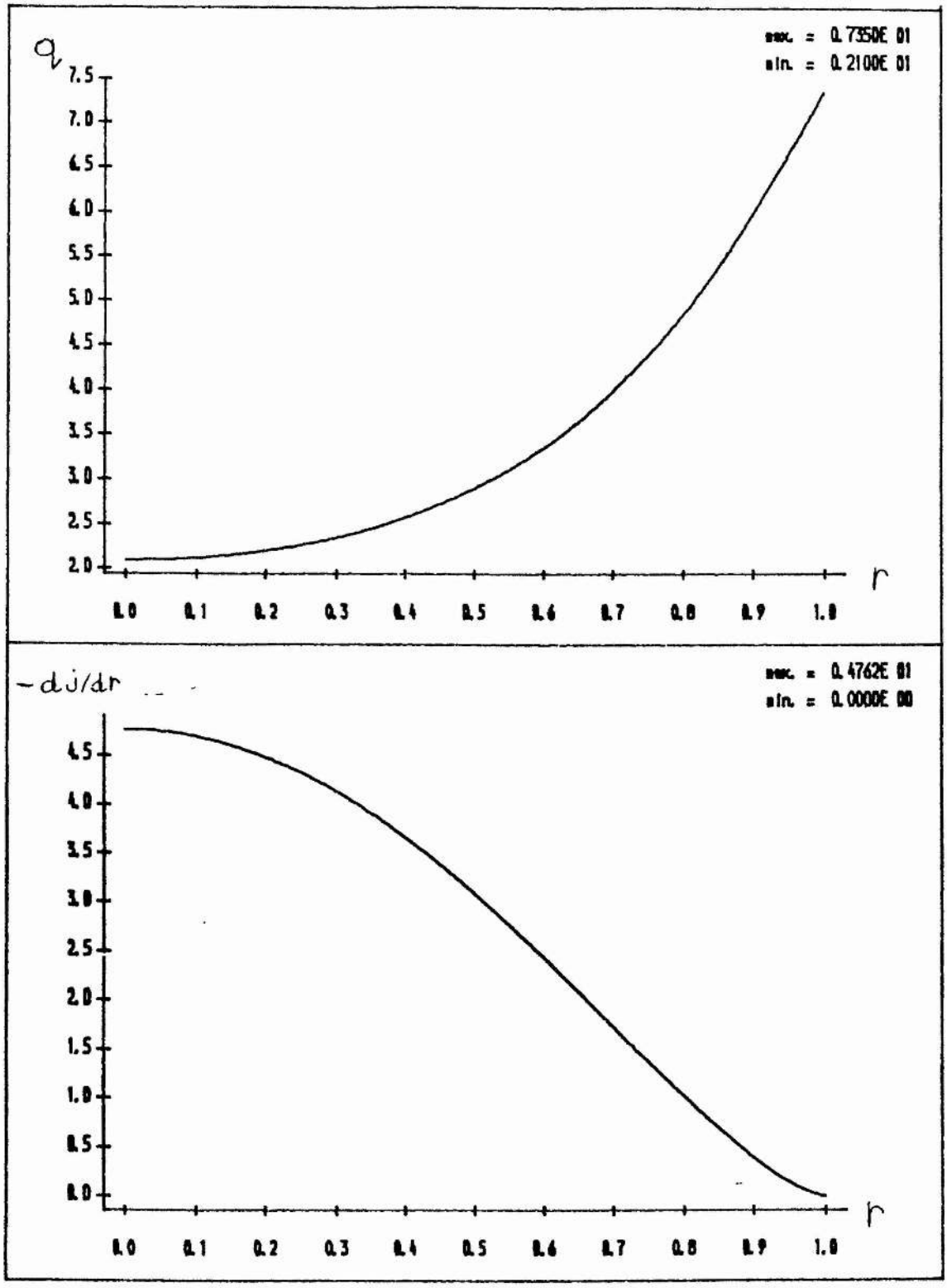

Figure 3.1. q and -dj/dr for q_o=2.1, μ=2.5.

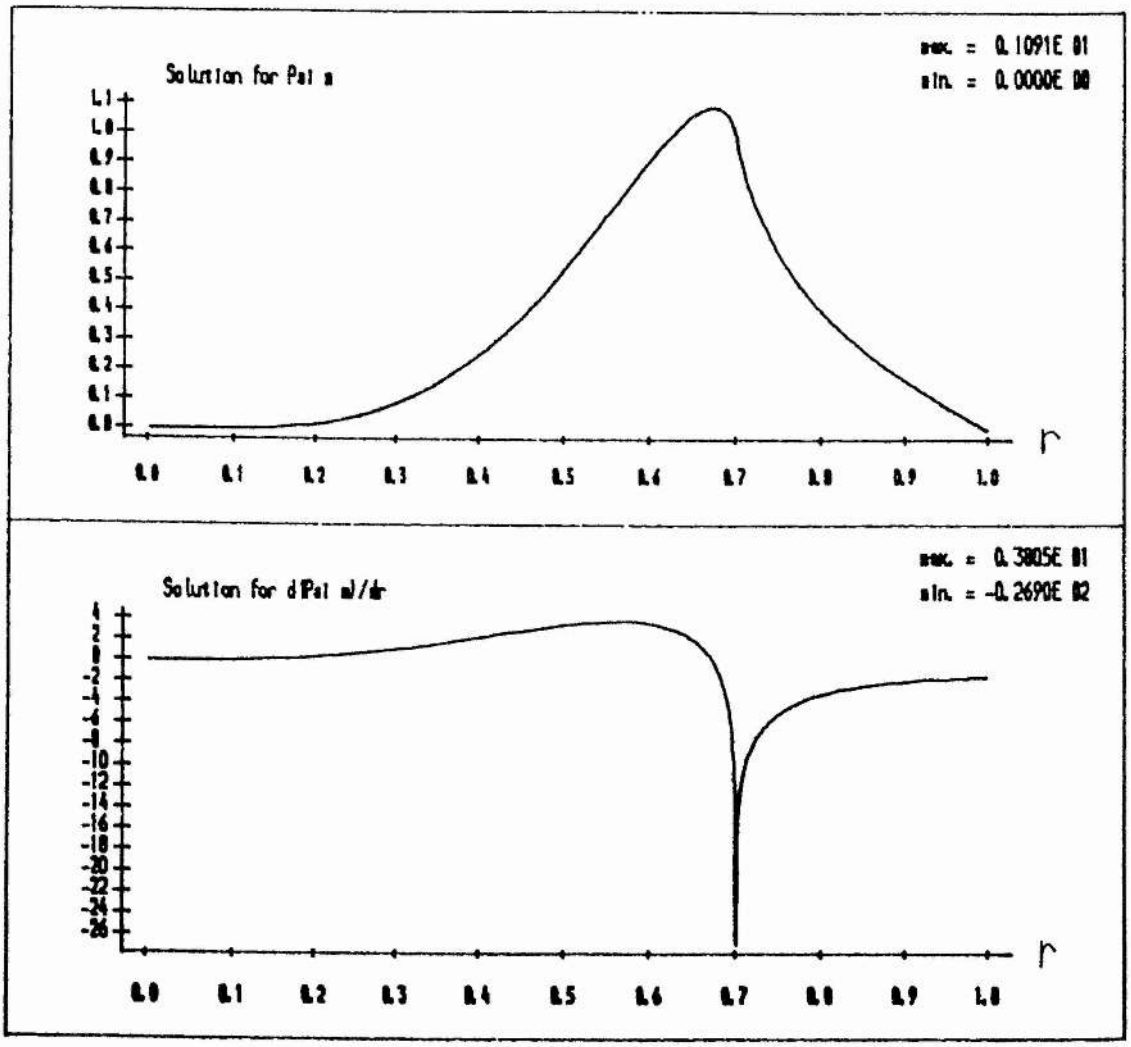

Figure 3.2. Uncoupled tearing eigenfunction for m=4 and q shown in fig 3.1.

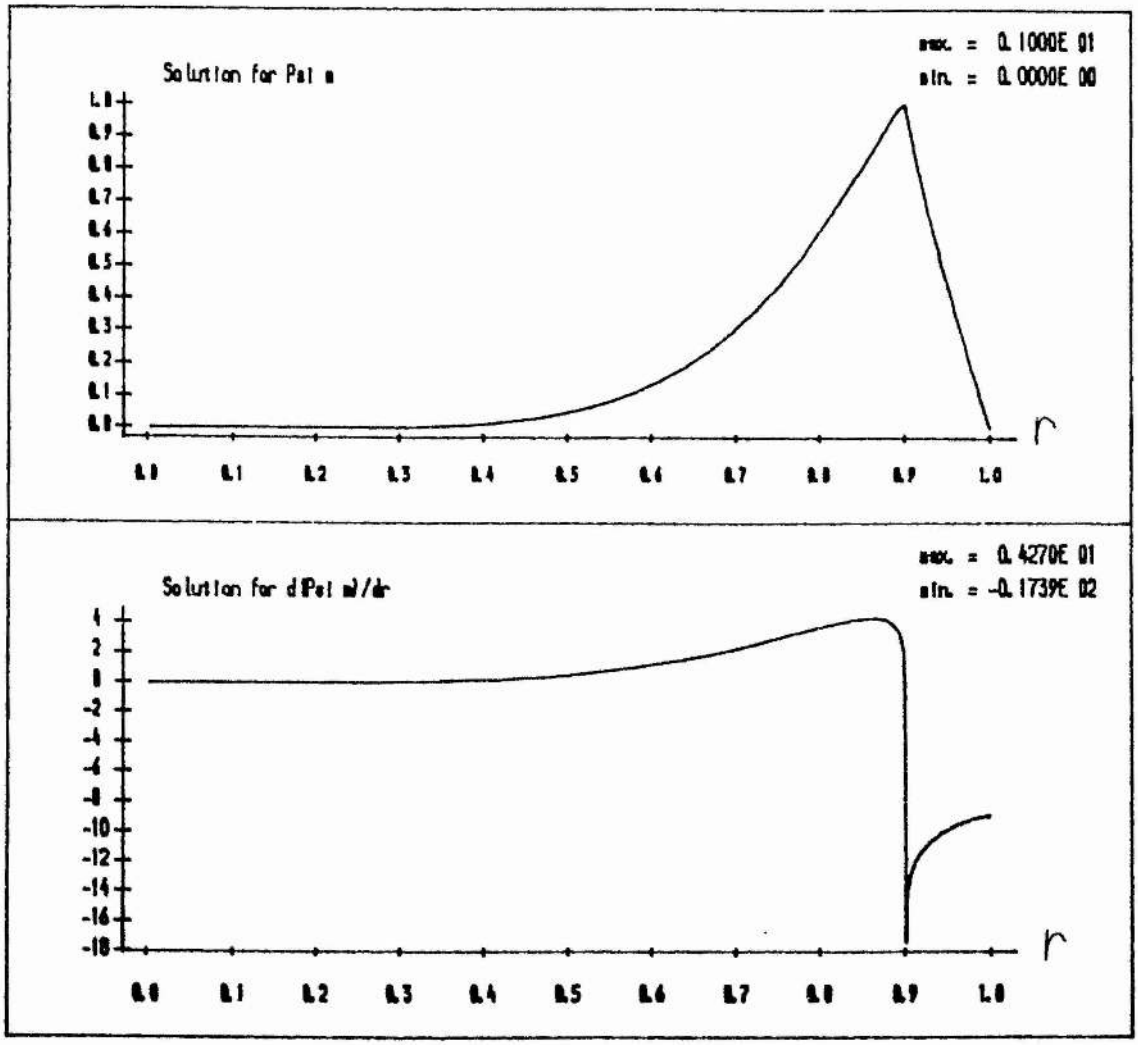

Figure 3.3. Uncoupled tearing eigenfunction for m=6 and q shown in fig 3.1.

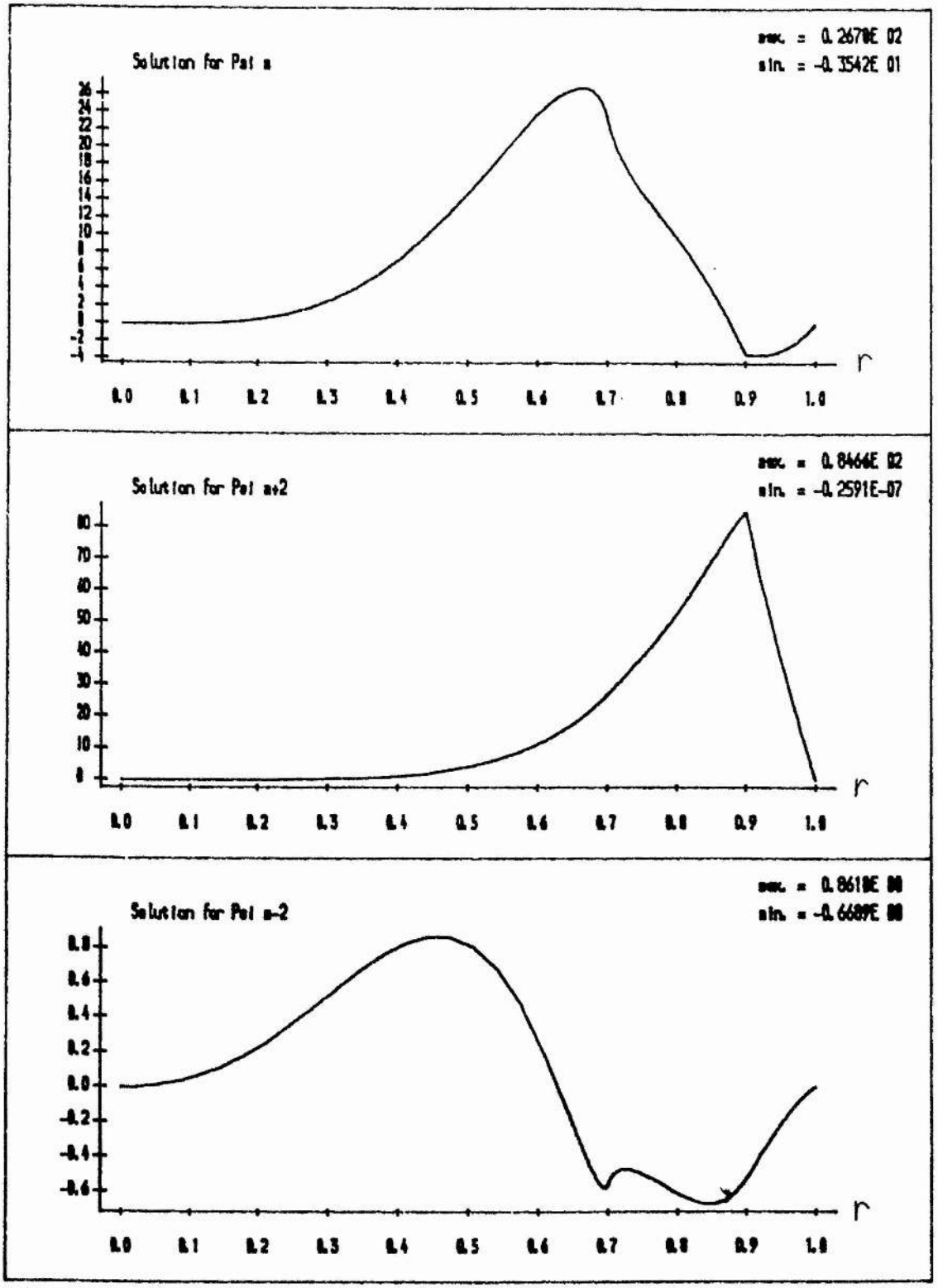

Figure 3.4.(a) Coupled tearing for central mode m=4. Ψ functions for q shown in figure 3.1. ; $\varepsilon = 0.1$, $\Delta_4'/\Delta_6' = 0.2$.

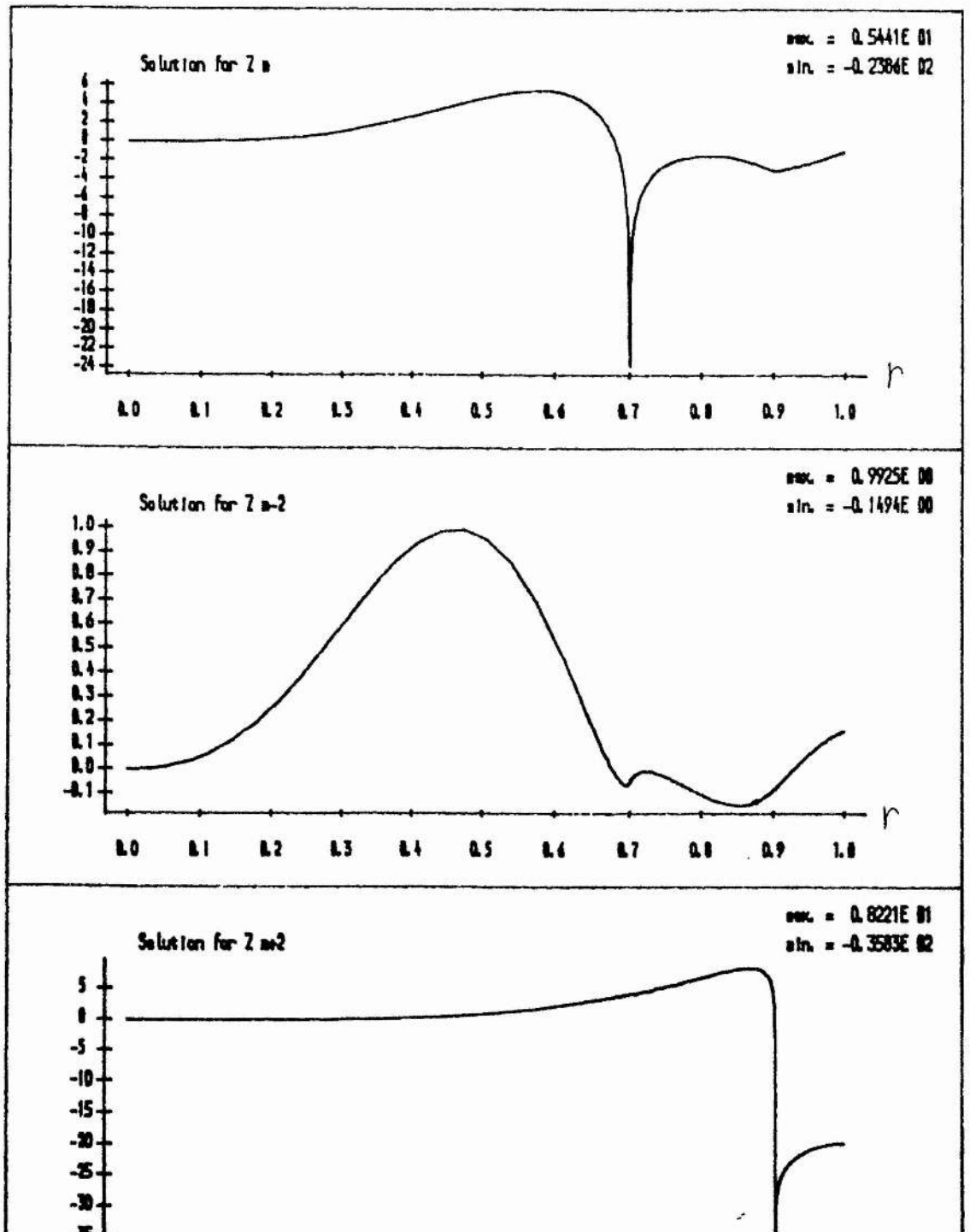

Figure 3.4.(b) Coupled tearing for central mode m=4. z functions for q shown in figure 3.1. ; $\varepsilon = 0.1$, $\Delta_4'/\Delta_6' = 0.2$.

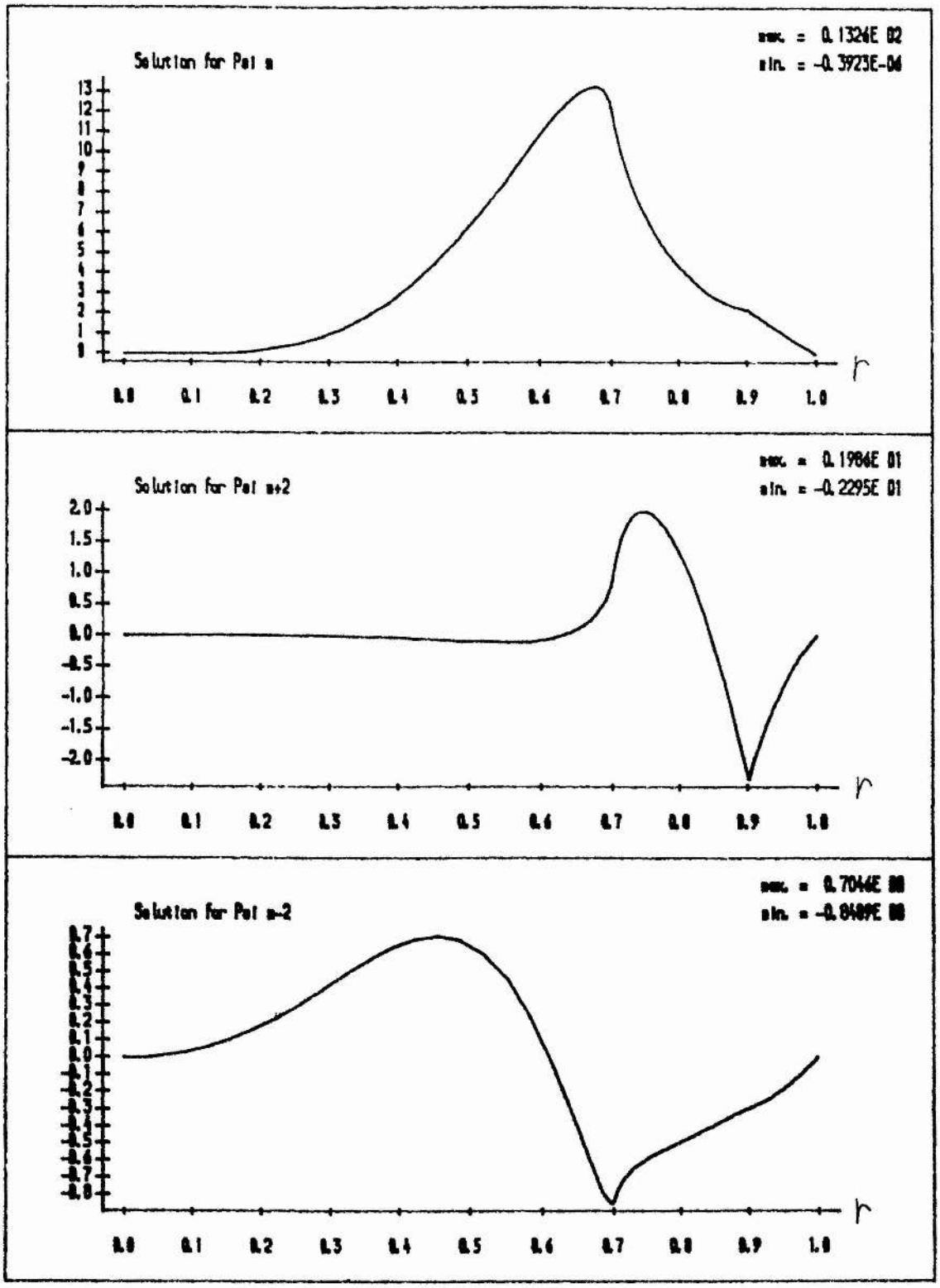

Figure 3.5.(a) Coupled tearing for central mode m=4. Ψ functions for q shown in figure 3.1. ; $\varepsilon = 0.2$, $\Delta_4'/\Delta_6' = 0.2$.

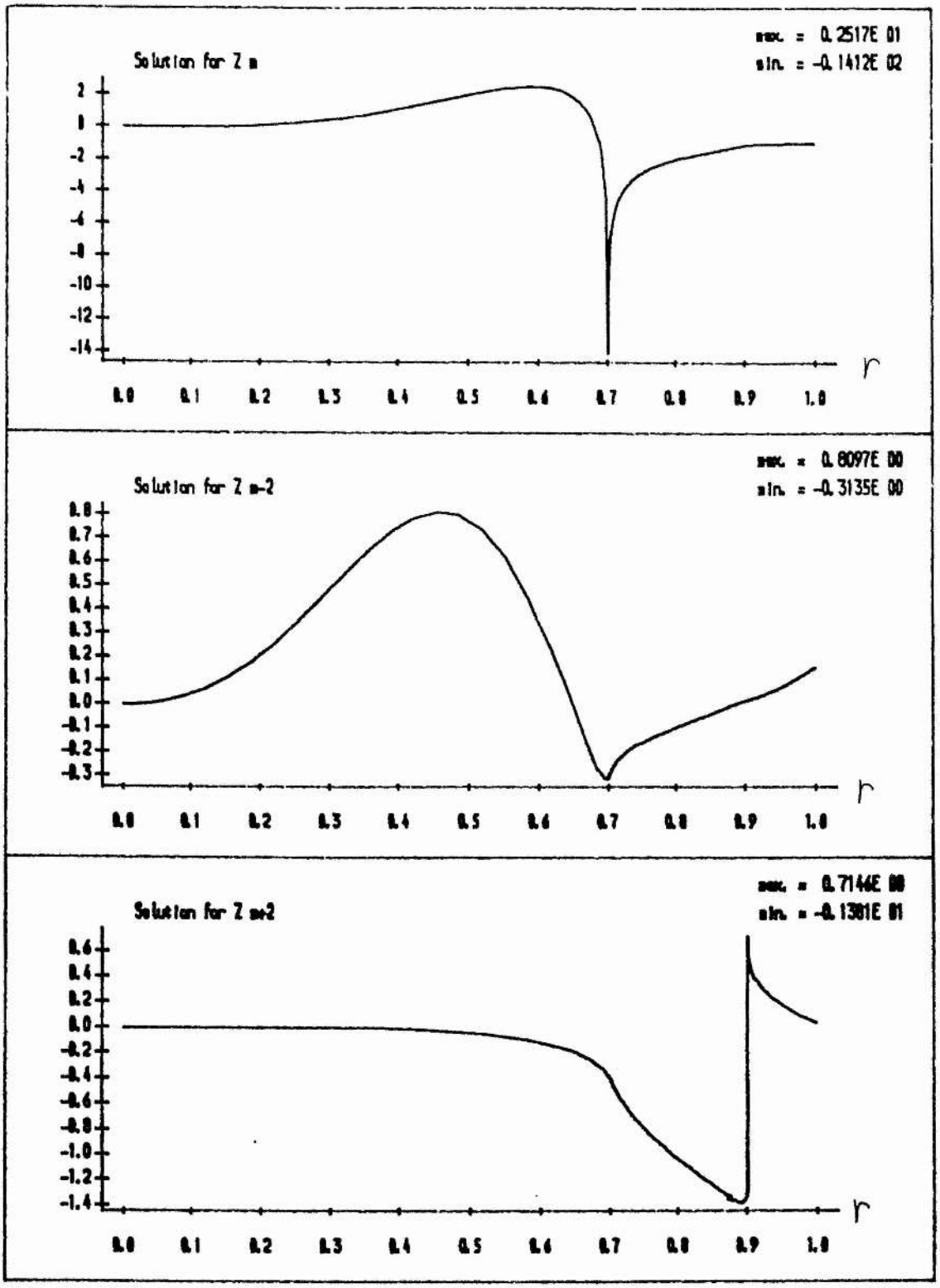

Figure 3.5.(b) Coupled tearing for central mode m=4. z functions for q shown in figure 3.1. ; $\varepsilon = 0.2$, $\Delta_4'/\Delta_6' = 0.2$.

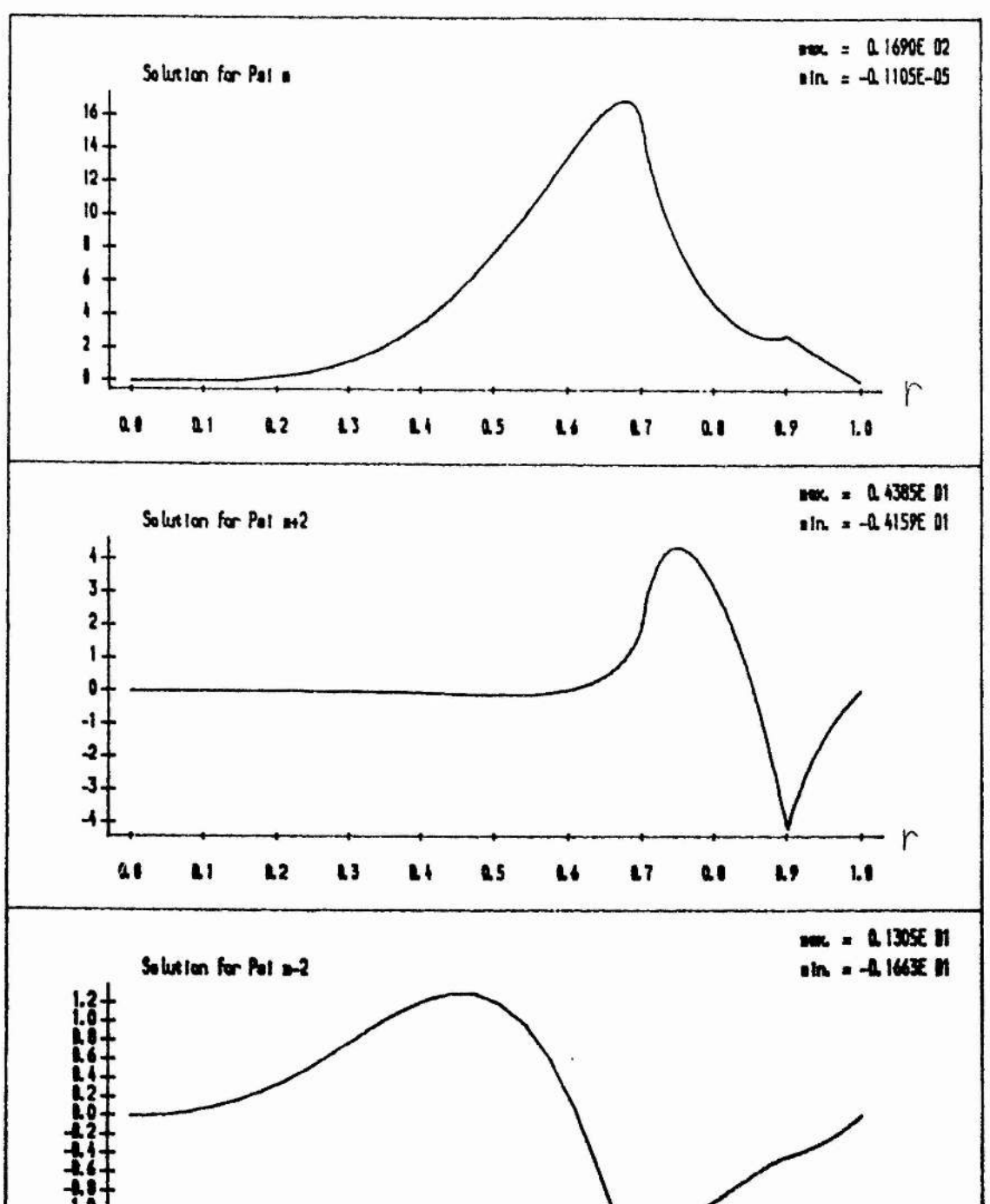

Figure 3.6.(a) Coupled tearing for central mode m=4. Ψ functions for q shown in figure 3.1. ; $\varepsilon = 0.3$, $\Delta_4'/\Delta_6' = 0.2$.

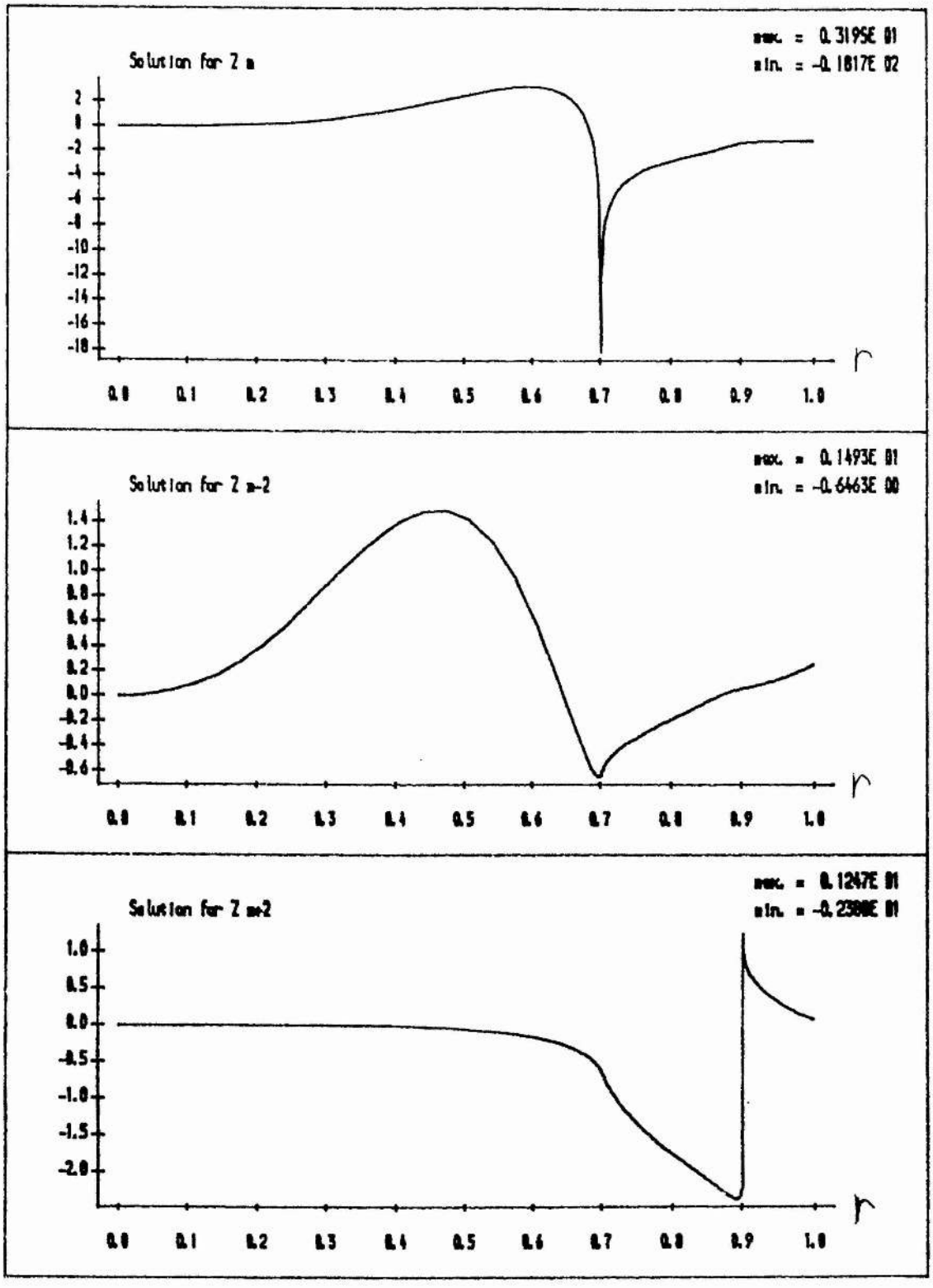

Figure 3.6.(b) Coupled tearing for central mode m=4. z functions for q shown in figure 3.1. ; $\varepsilon = 0.3$, $\Delta_4'/\Delta_6' = 0.2$.

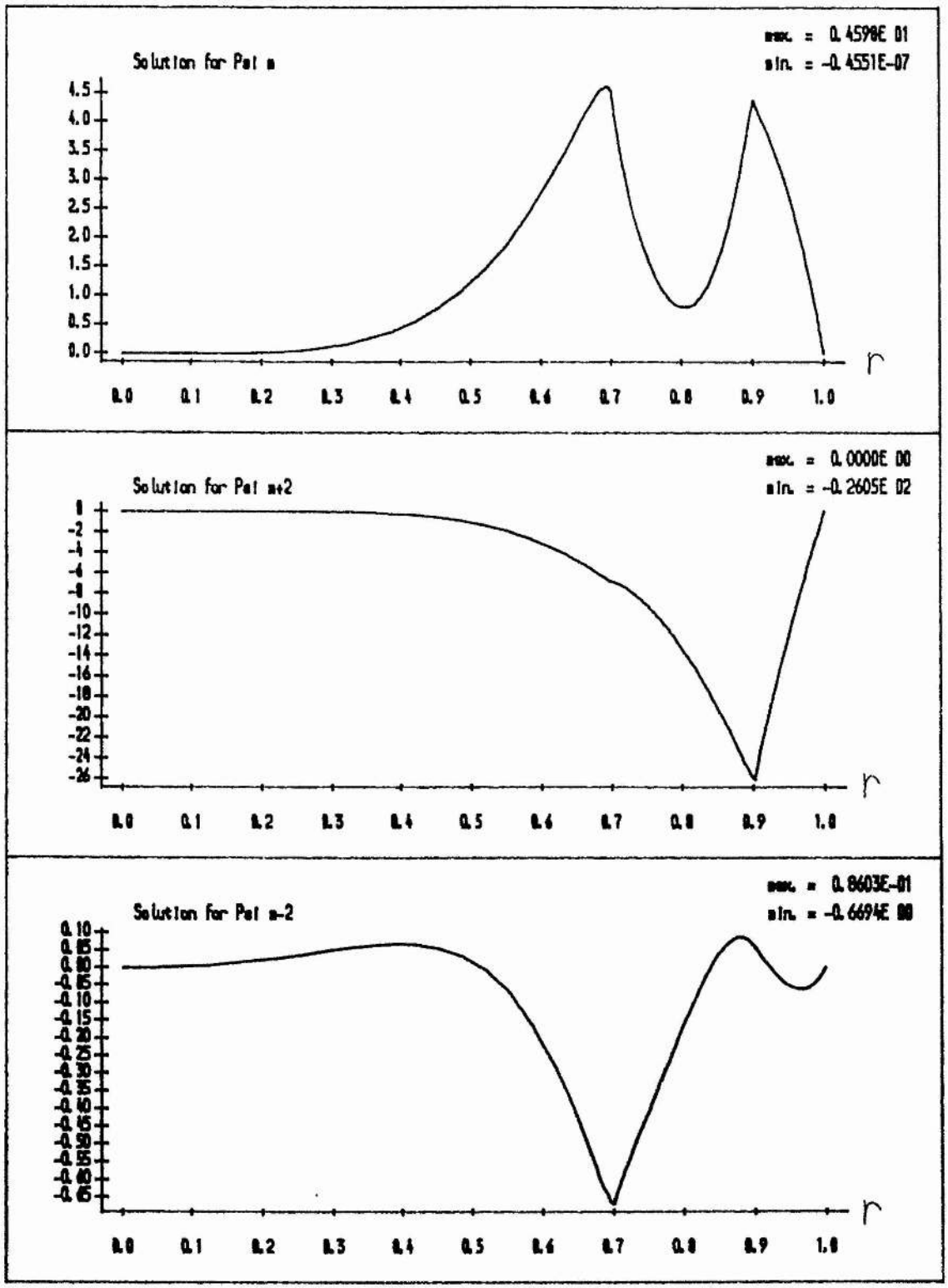

Figure 3.7.(a) Coupled tearing for central mode m=4. Ψ functions for q shown in figure 3.1. ; $\varepsilon = 0.2$, $\Delta_4'/\Delta_6' = 1.0$.

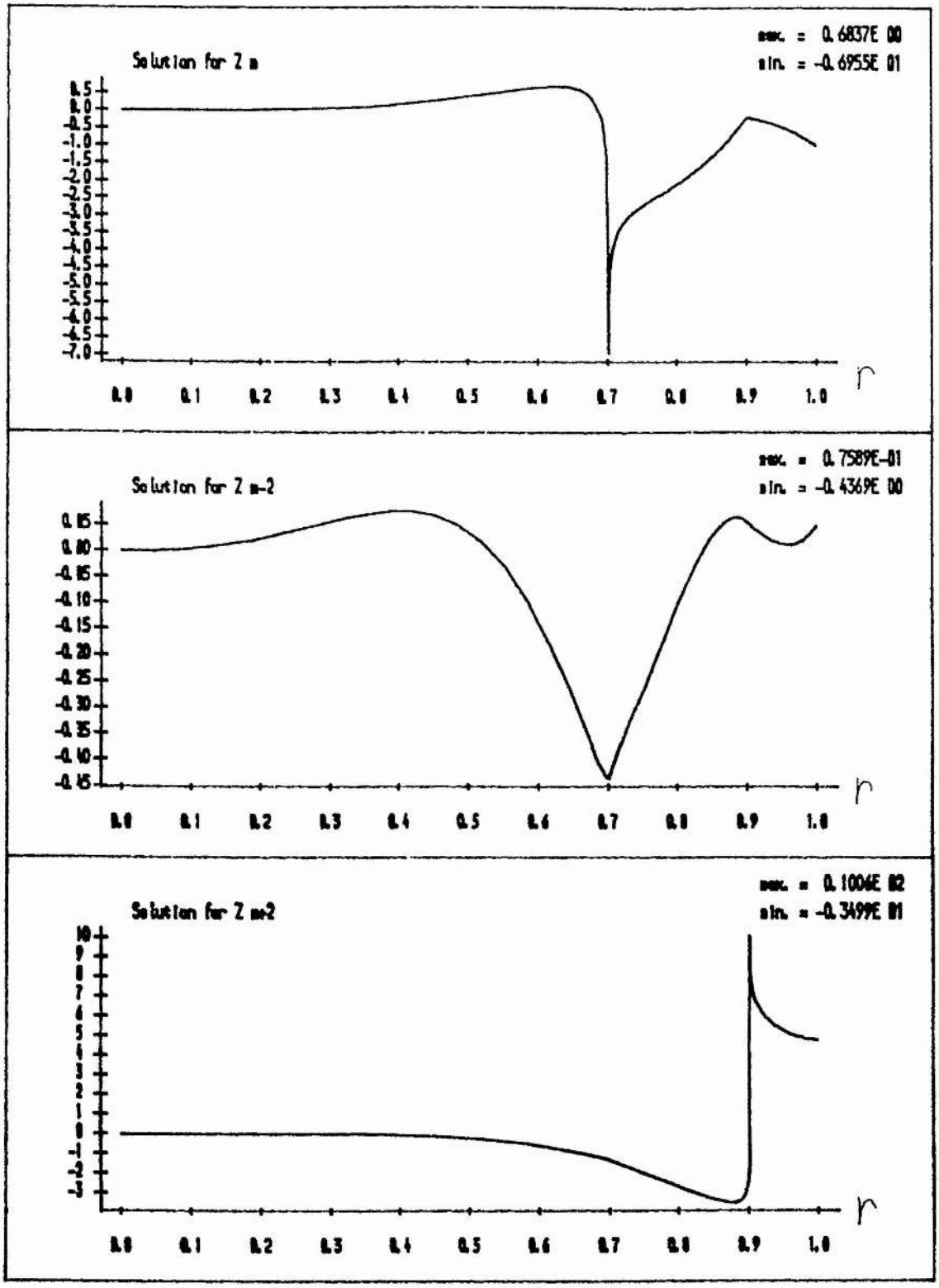

Figure 3.7.(b) Coupled tearing for central mode m=4. z functions for q shown in figure 3.1. ; $\varepsilon = 0.2$, $\Delta_4'/\Delta_6' = 1.0$.

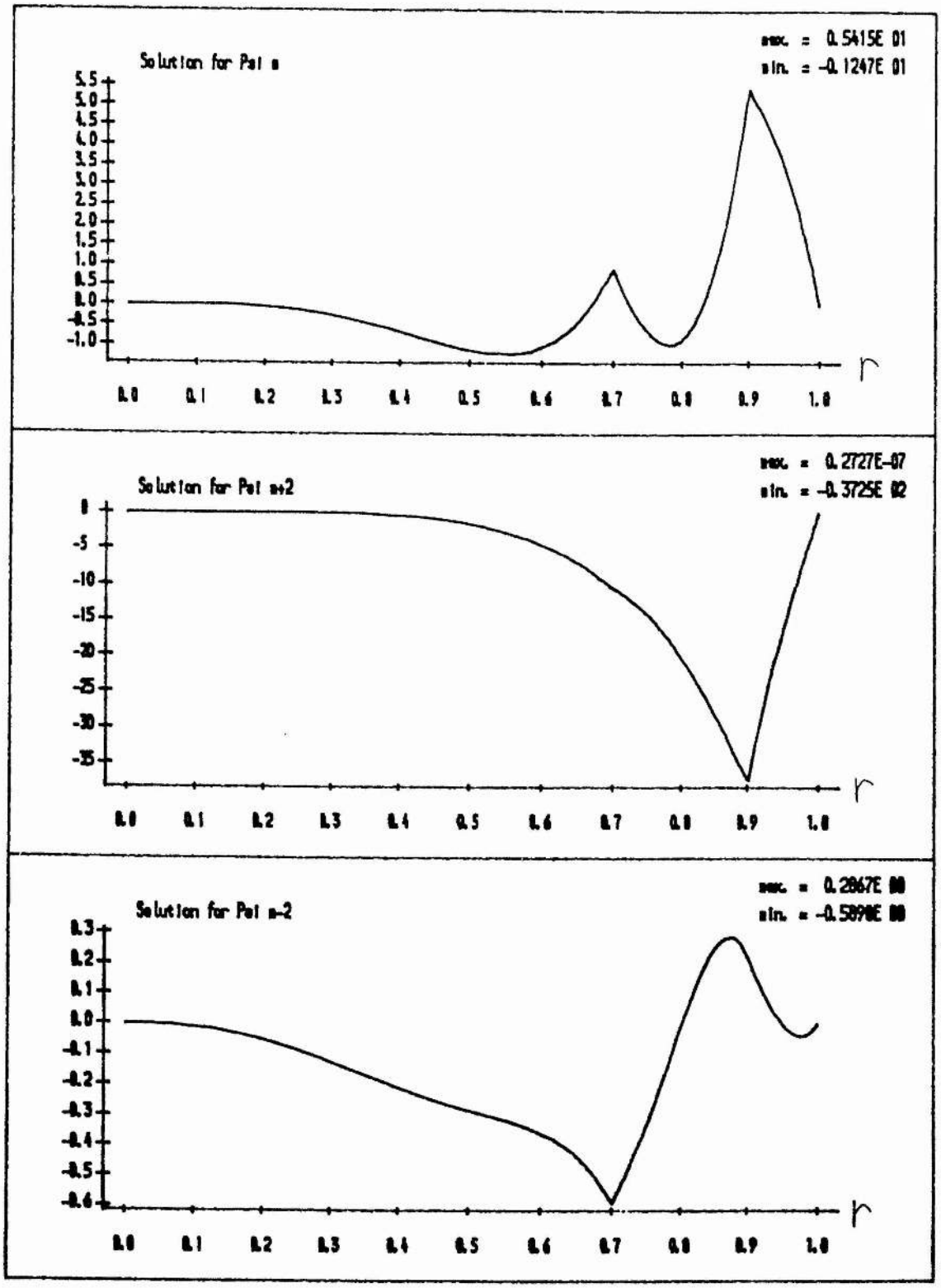

Figure 3.8.(a) Coupled tearing for central mode m=4. Ψ functions for q shown in figure 3.1. ; $\varepsilon = 0.2$, $\Delta_4'/\Delta_6' = 5.0$.

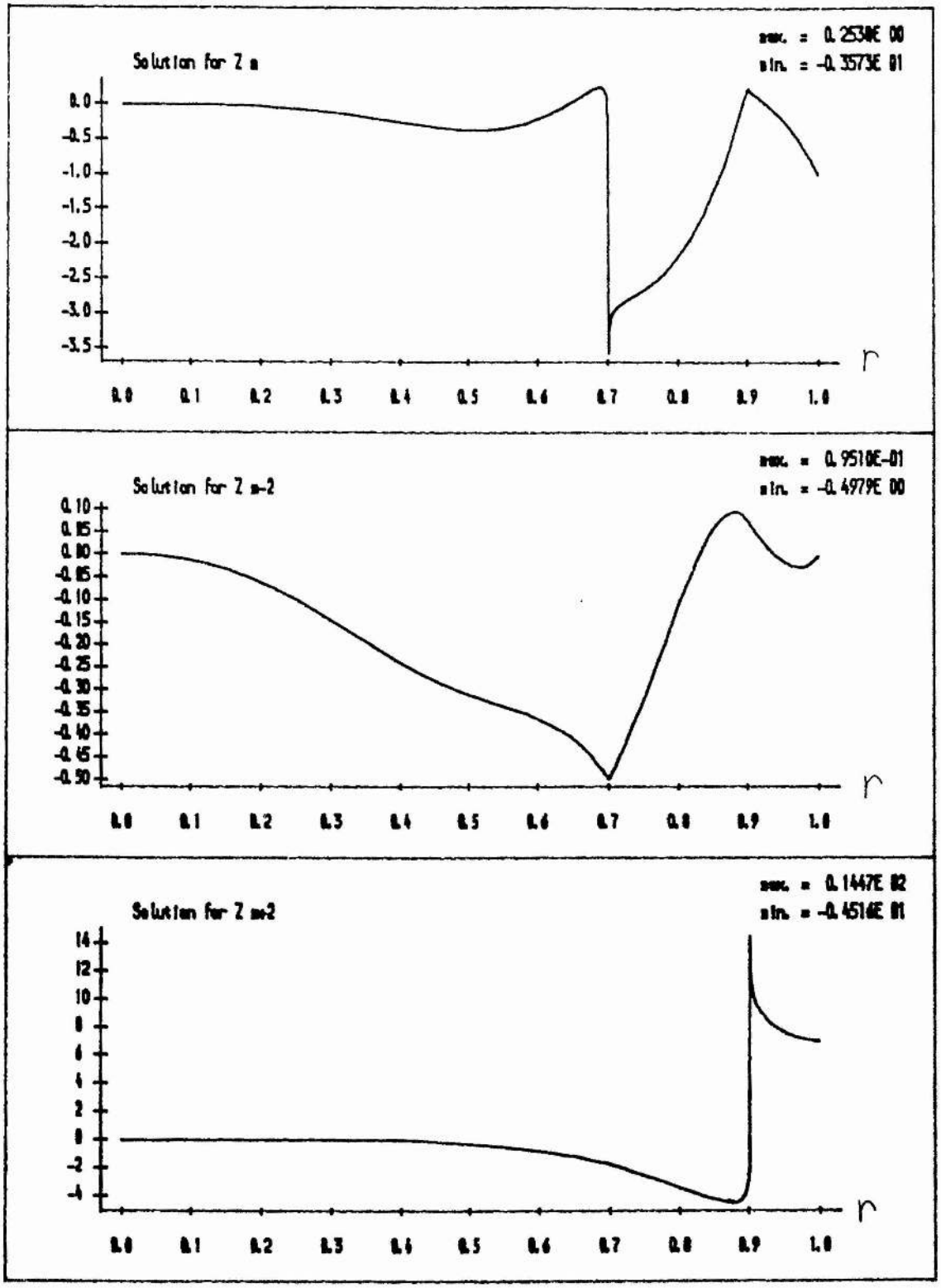

Figure 3.8.(b) Coupled tearing for central mode m=4. z functions for q shown in figure 3.1. ; $\varepsilon = 0.2$, $\Delta_4'/\Delta_6' = 5.0$.

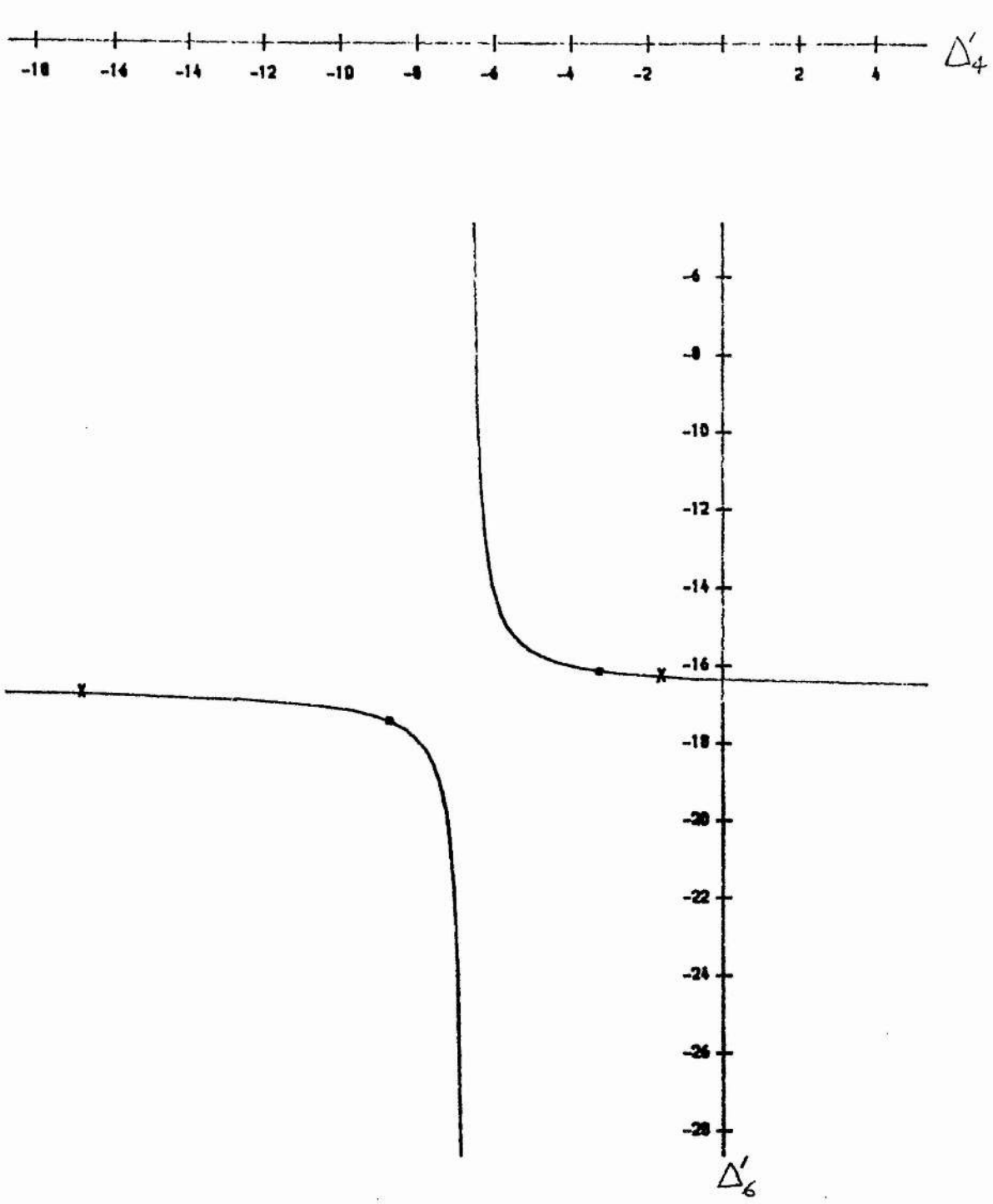

Figure 3.9. Coupled tearing for central mode m=4 and q shown in fig. 3.1.

Hyperbola for $\varepsilon = 0.1$.

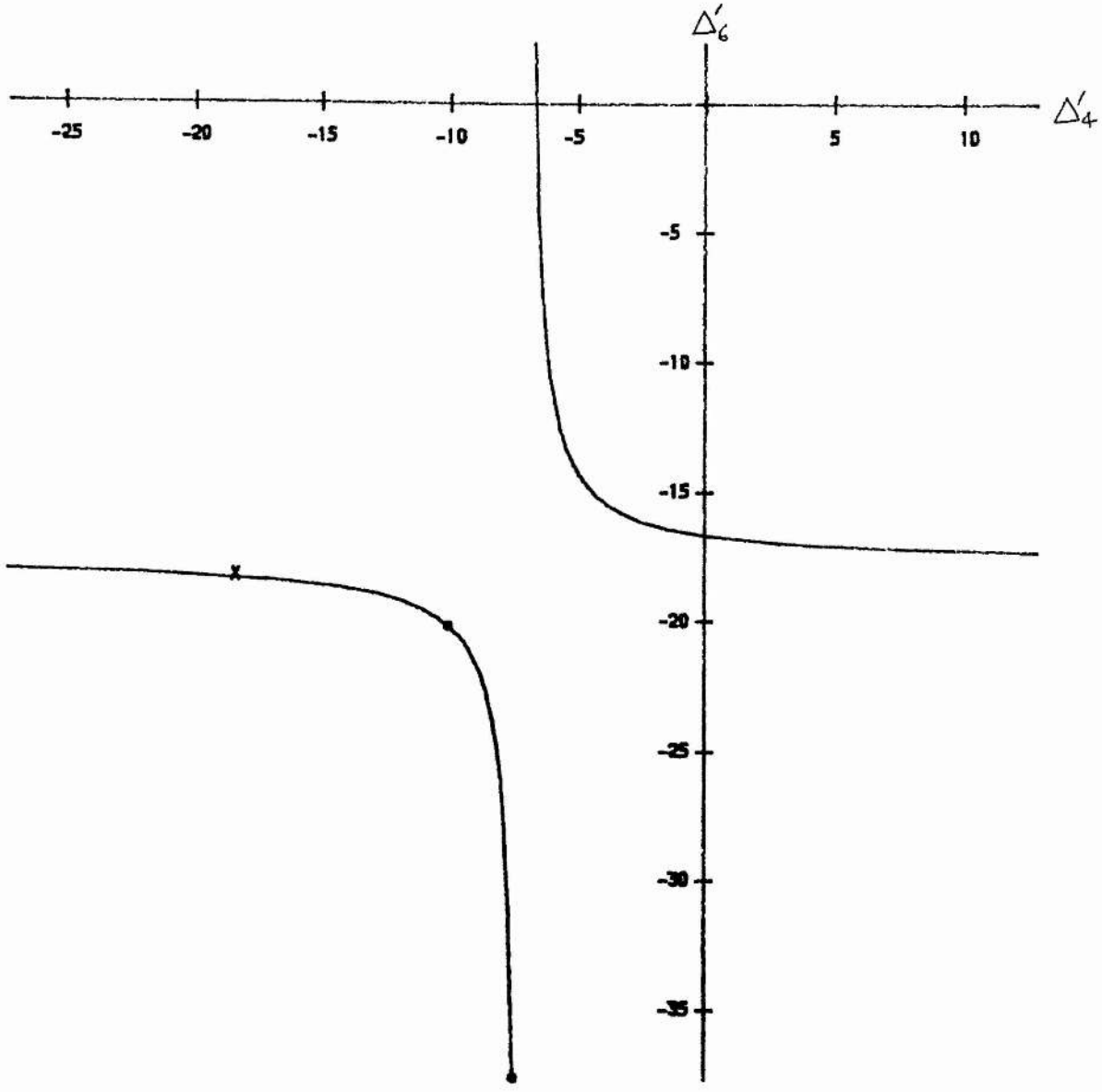

Figure 3.10. Coupled tearing for central mode m=4 and q shown in fig. 3.1.

Hyperbola for $\varepsilon = 0.2$.

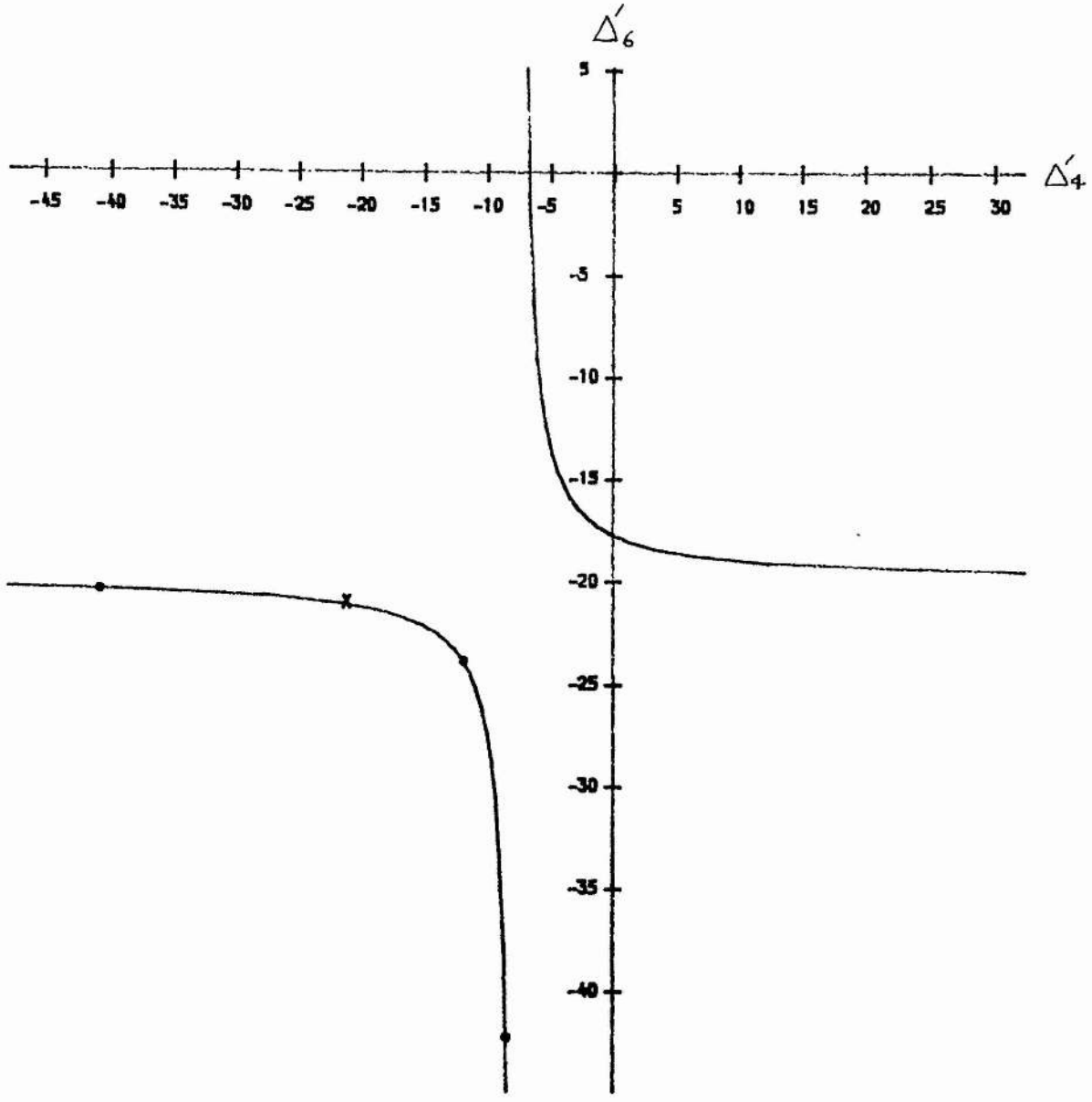

Figure 3.11. Coupled tearing for central mode m=4 and q shown in fig. 3.1.

Hyperbola for $\varepsilon = 0.3$.

as check points. Some points do not appear in the plotted regions. It is evident that ellipticity is stabilising in this case, since α and β decrease with increasing ε, while $\alpha\beta-\lambda$ increases. The destabilising effect of increasing λ is not significant in this case. Hence, we were led to seek an equilibrium for which the uncoupled Δ's were both small and negative, in order that increasing ε would be likely to create an instability by making $\alpha\beta - \lambda$ negative. Due to the stabilising effect of magnetic tension, modes with high m and n are very stable, hence we chose to concentrate on the mode (m,n) = (2,1) , which is coupled to the modes (0,1) and (4,1) by elliptic (k=2) shaping. In addition, profiles with a very high q(a) are not likely to occur in a real tokamak (except in the current rise phase, when higher m tearing modes are possible), but a profile containing q=2 and q=4 is not unreasonable. Note that, for the special case m-k=0, Ψ_{m-k} is identically zero and drops out of our analysis.

3.5 Modified Current Profile.

Consider again the q-profile (3.20), which corresponds to a current profile

$$j(r) = \frac{2}{q_0}\left(1 - r^2\right)^{\mu} \qquad (3.21)$$

In order to obtain an appropriate equilibrium, we shall add exponentially localised bumps near the singular surfaces, giving the following class of profiles

$$j(r) = \frac{2}{q_0}\left(1 - r^2\right)^{\mu} + A_1 \exp\left(-\frac{(r-r_1)^2}{\alpha_1^2}\right) + A_2 \exp\left(-\frac{(r-r_2)^2}{\alpha_2^2}\right) \qquad (3.22)$$

For these later runs, δ_1 was converged to 10^{-5}, requiring typically 390 points in each interval. Take, for instance, the profile specified by $q_0 = 1.1$ $\mu = 4$, shown in Fig. 3.12. The uncoupled Δ's for our chosen modes are $\Delta'_2 = 8.9$ and $\Delta'_4 = -11.1$ at the singular surfaces $r_2 = 0.552$ and $r_4 = 0.852$. If we make the profile drop less

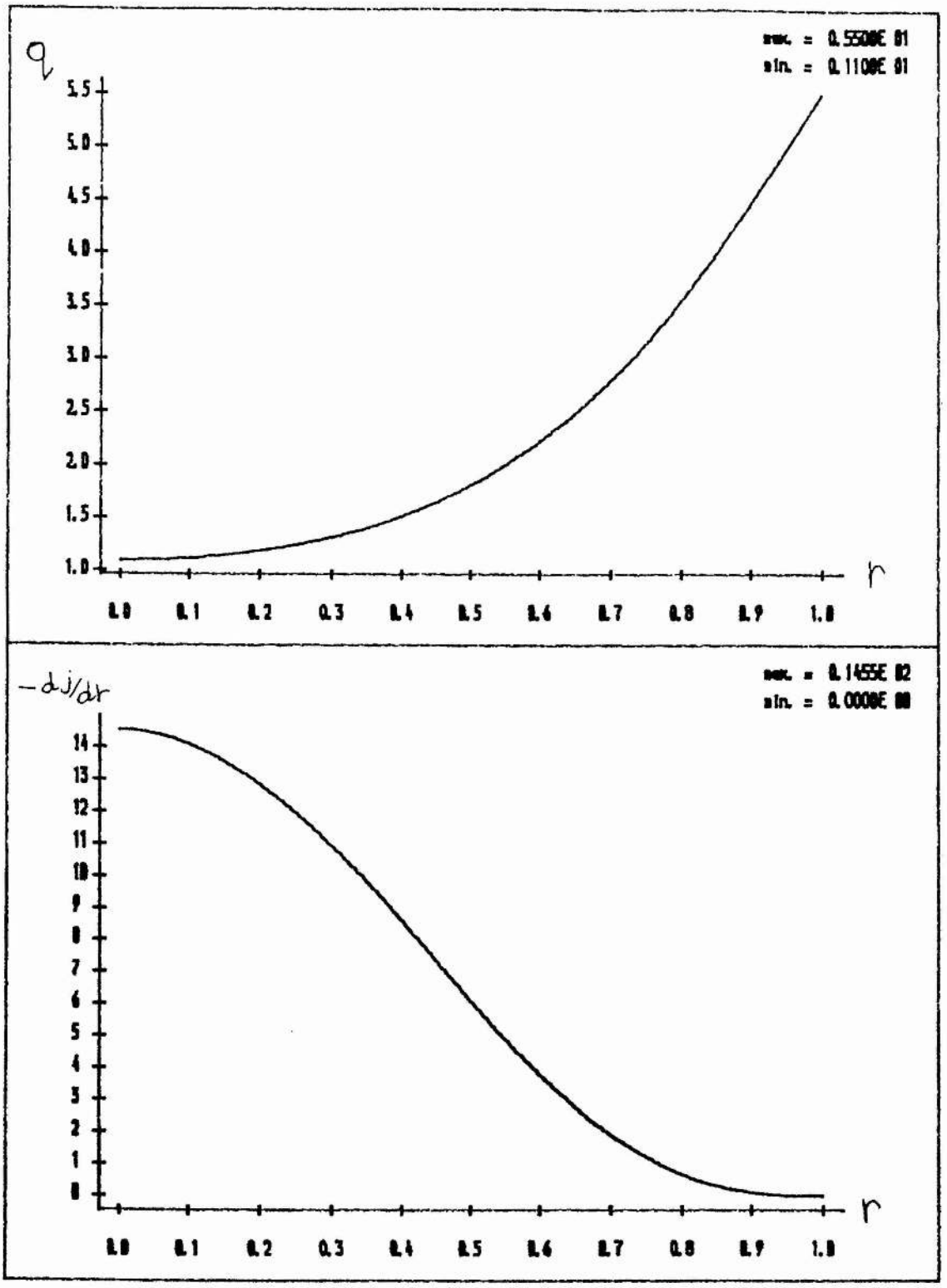

Figure 3.12. q and -dj/dr for q_o=1.1, μ=4.

steeply through the m=2 singular surface and more steeply through the m=4, we may stabilise m=2 and destabilise m=4. Taking the values $A_1 = 1.265$, $A_2 = 6.6$, $r_1 = 0.57$, $r_2 = 0.832$, $\alpha_1 = 0.03$ and $\alpha_2 = 0.02$ gives the desired result $\Delta'_2 = -1.20$ and $\Delta'_4 = -1.05$. The new profile is shown in diagram 3.13; note that the j-profile is non-monotonic (the derivative shown changes sign) in a narrow region near r_4, but the q-profile is almost unchanged. The new singular radii are $r_2 = 0.553$ and $r_4 = 0.864$. The results of our code for this equilibrium are shown below

ε	α	β	λ	$\alpha\beta - \lambda$
0.0	-1.20	-1.05	0.0	1.26
0.1	-1.20	-0.74	0.63	0.26
0.15	-1.15	-0.37	1.47	-0.41
0.2	-1.08	0.09	2.76	-2.86

The hyperbolae are shown in Figs. 3.14-3.16 and the unstable eigenfunctions for $\varepsilon = 0.15$, $\Delta_2'/\Delta_4' = 0.2, 1.0$ and 5.0 are shown in Fig.s. 3.17-3.19. It can be seen that, at a value of ε between 0.1 and 0.15 ($\varepsilon \approx 0.12$), the upper branch of the hyperbola enters the first quadrant and instability becomes possible. These are typical values of ellipticity for real tokamaks.

3.6 Discussion.

We have shown that coupling to an m=4 mode, due to elliptic distortion of the plasma surfaces, may drive an m=2 mode unstable. The class of equilibria involved was somewhat contrived, but not unreasonable and the instability occurred at realistic values of the ellipticity. We expect that the inclusion of finite equilibrium pressure gradients would allow more instabilities, since they represent a new source of energy to drive such instabilities. The pressure gradient terms in (3.11) and (3.12) cause singularities at

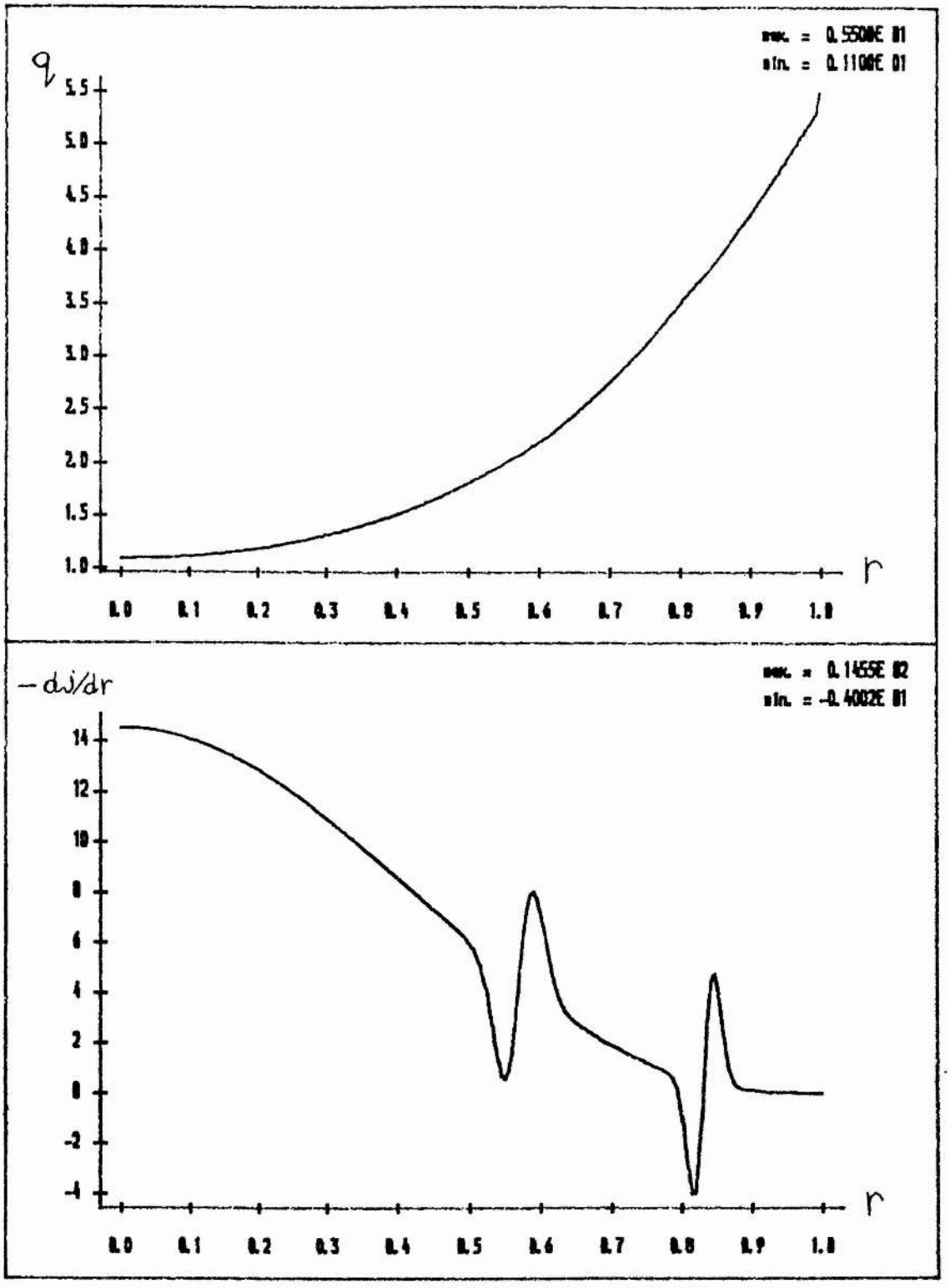

Figure 3.13. q and -dj/dr for q_o=1.1, μ=4, with

exponentially localised modifications.

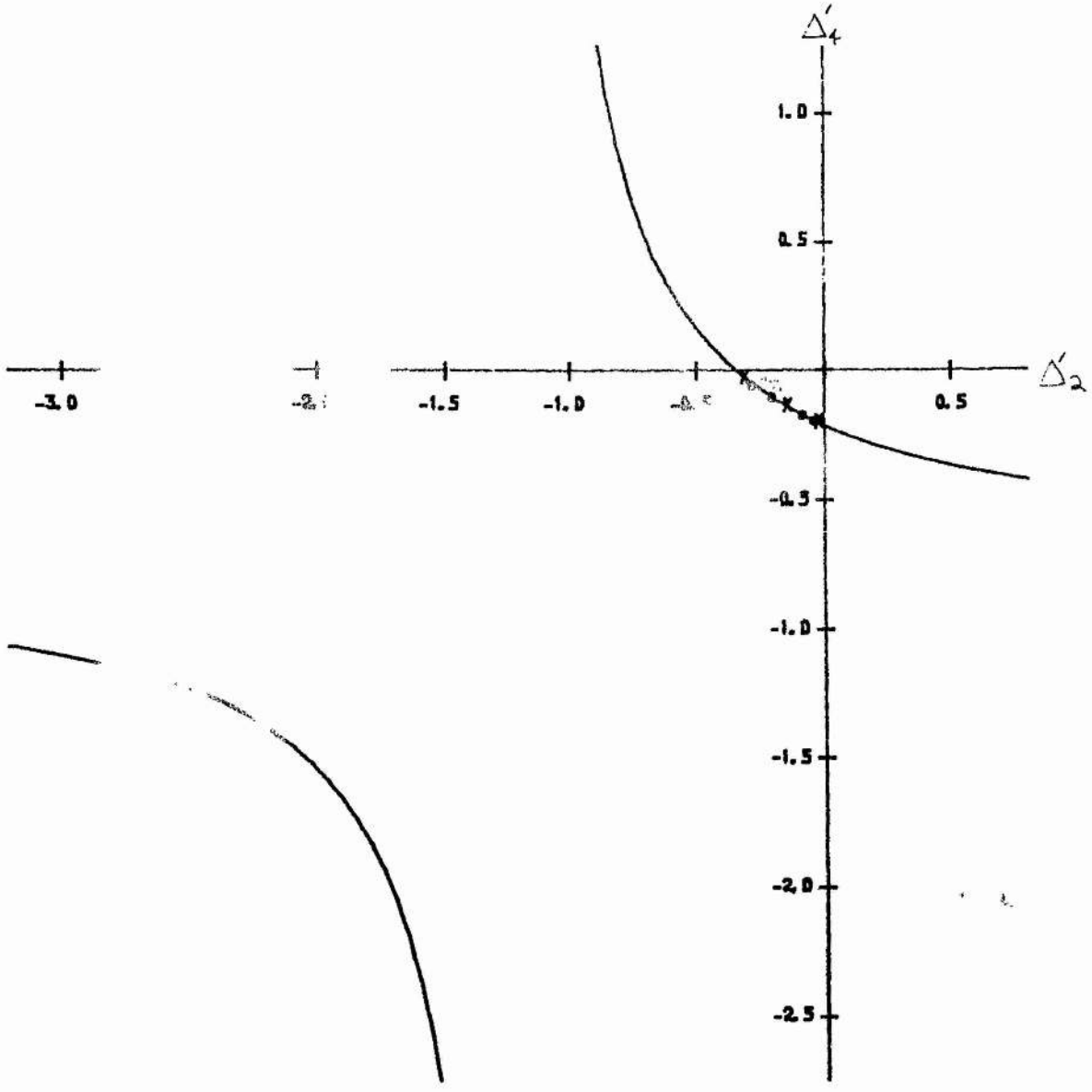

Figure 3.14. Coupled tearing for central mode m=2 and q shown in fig. 3.1

Hyperbola for $\varepsilon = 0.1$.

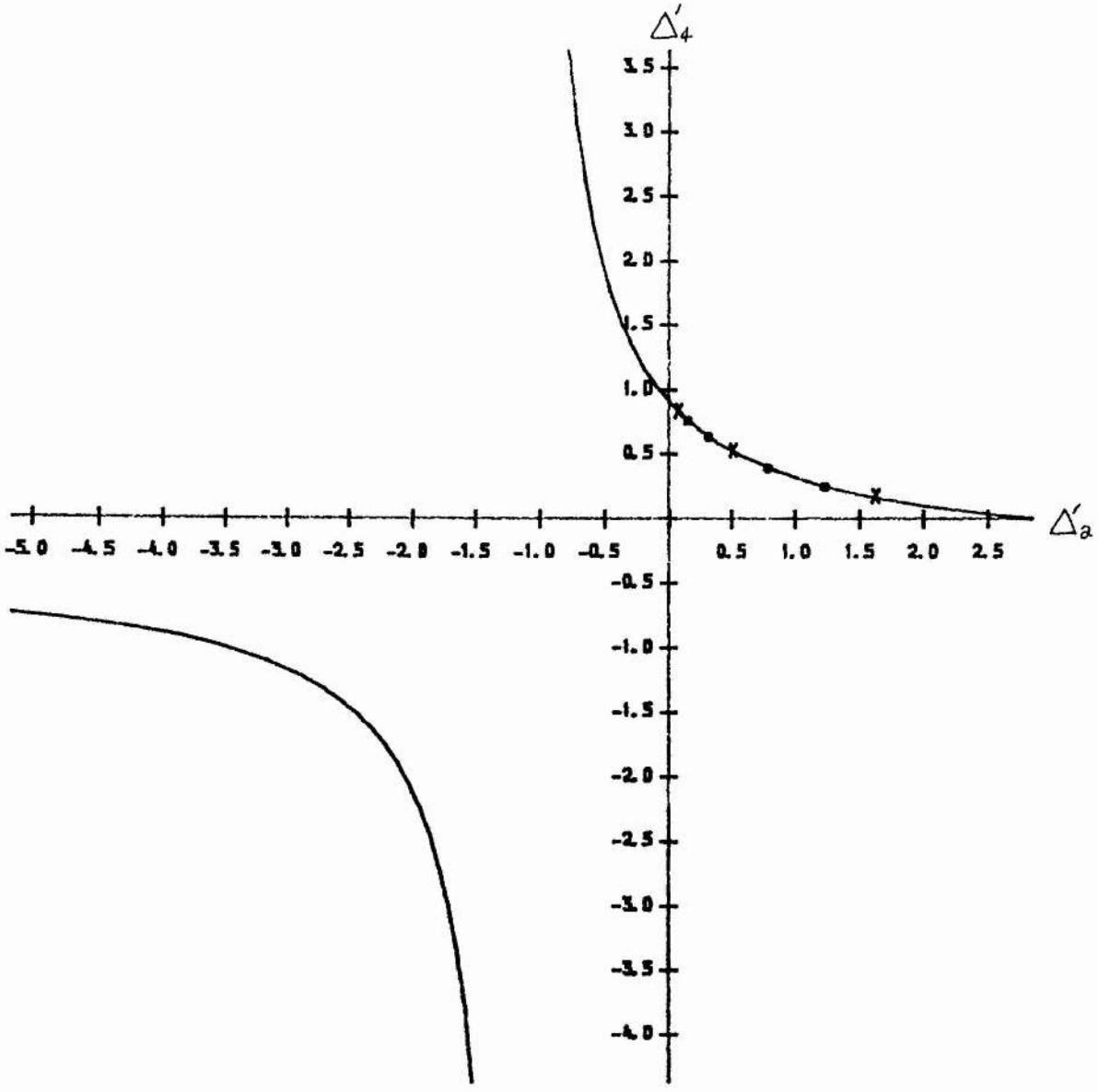

Figure 3.15. Coupled tearing for central mode m=2 and q shown in fig. 3.13.

Hyperbola for $\varepsilon = 0.15$.

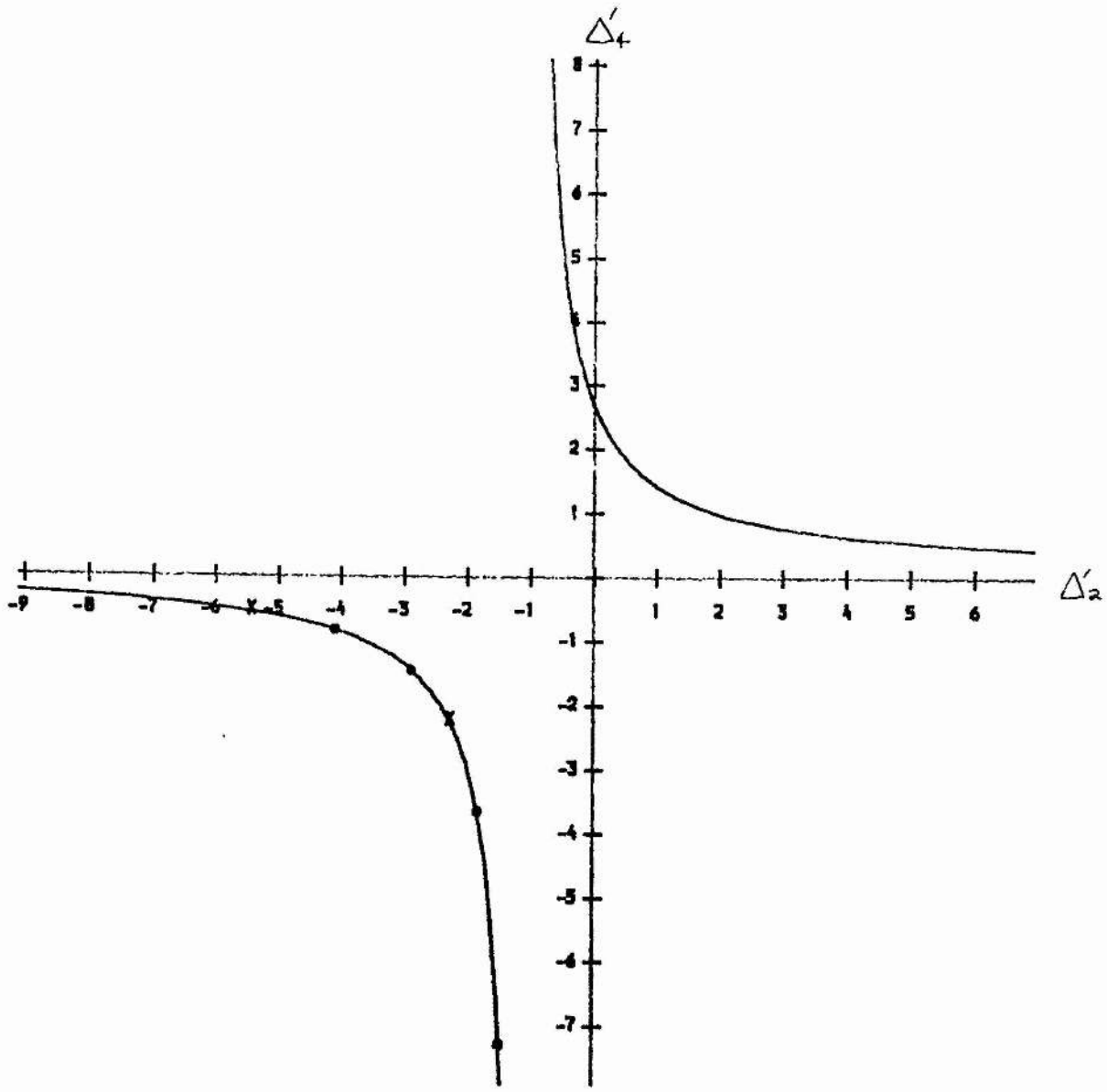

Figure 3.16. Coupled tearing for central mode m=2 and q shown in fig. 3.13.

Hyperbola for $\varepsilon = 0.2$.

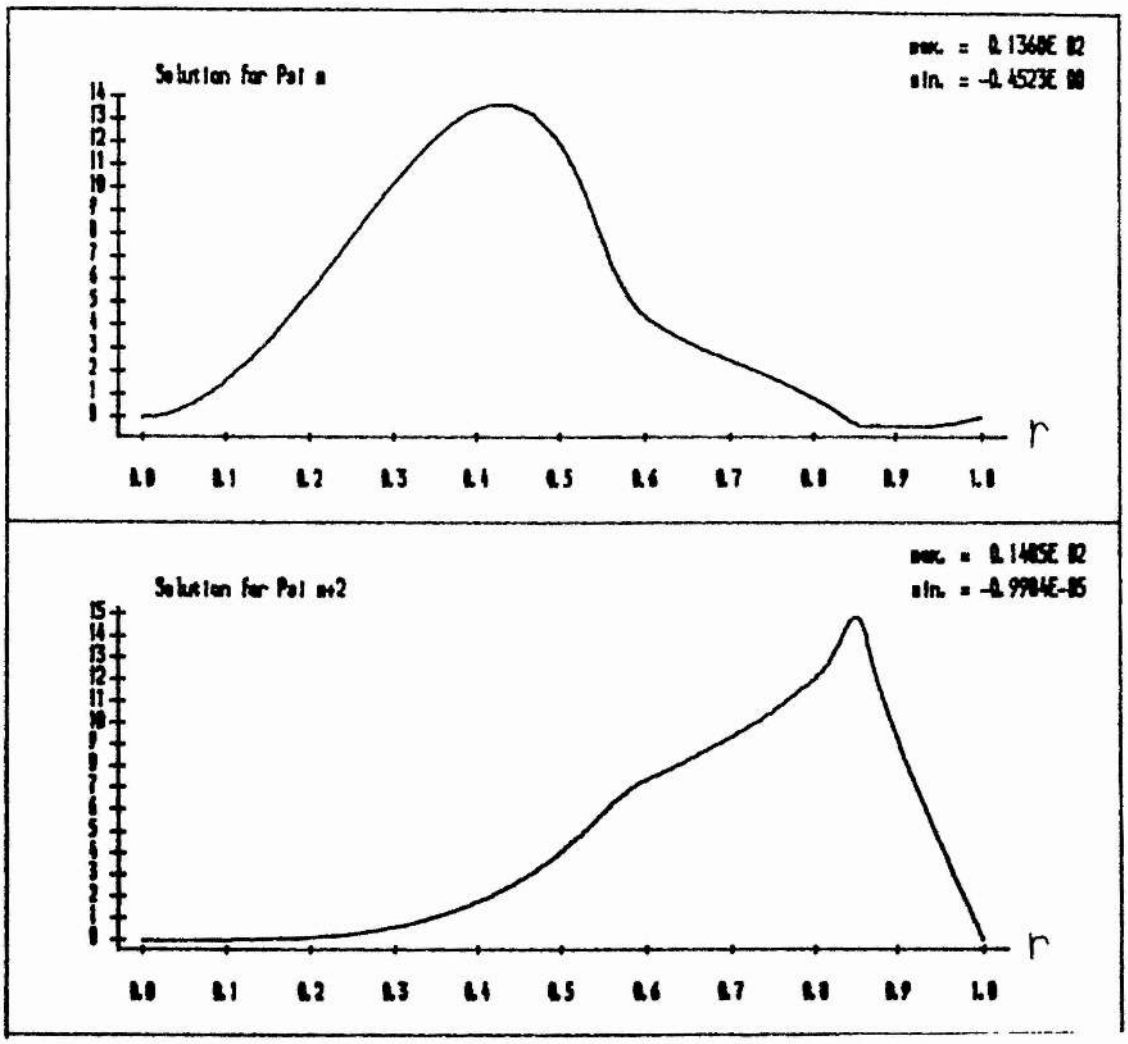

Figure 3.17(a). Coupled tearing: Ψ functions for central mode m=2 and q shown in fig. 3.13.; ε=0.15, Δ_4'/Δ_2'=0.2.

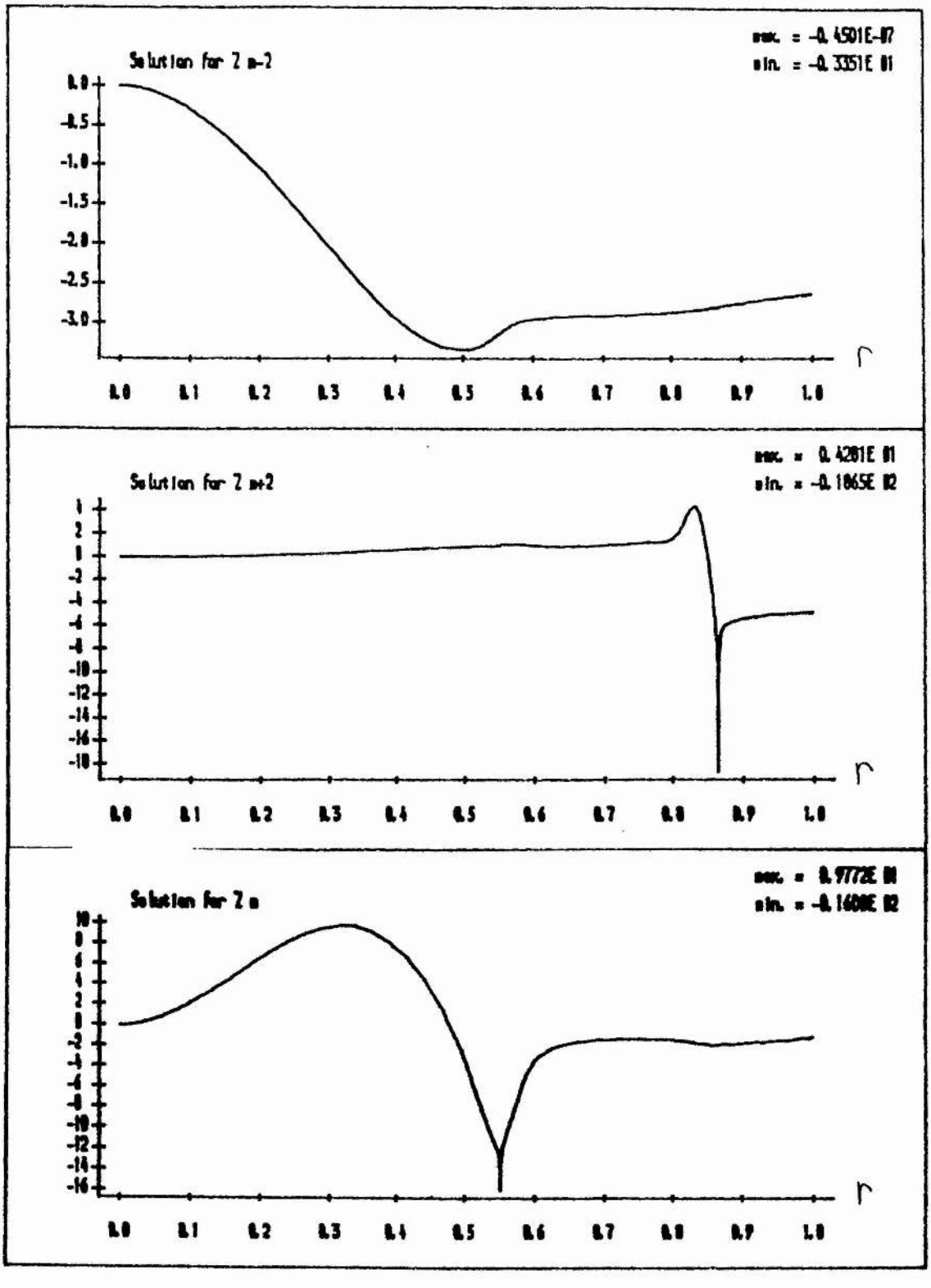

Figure 3.17(b). Coupled tearing: z functions for central mode m=2 and q shown in fig. 3.13.; ε=0.15, Δ_4'/Δ_2'=0.2.

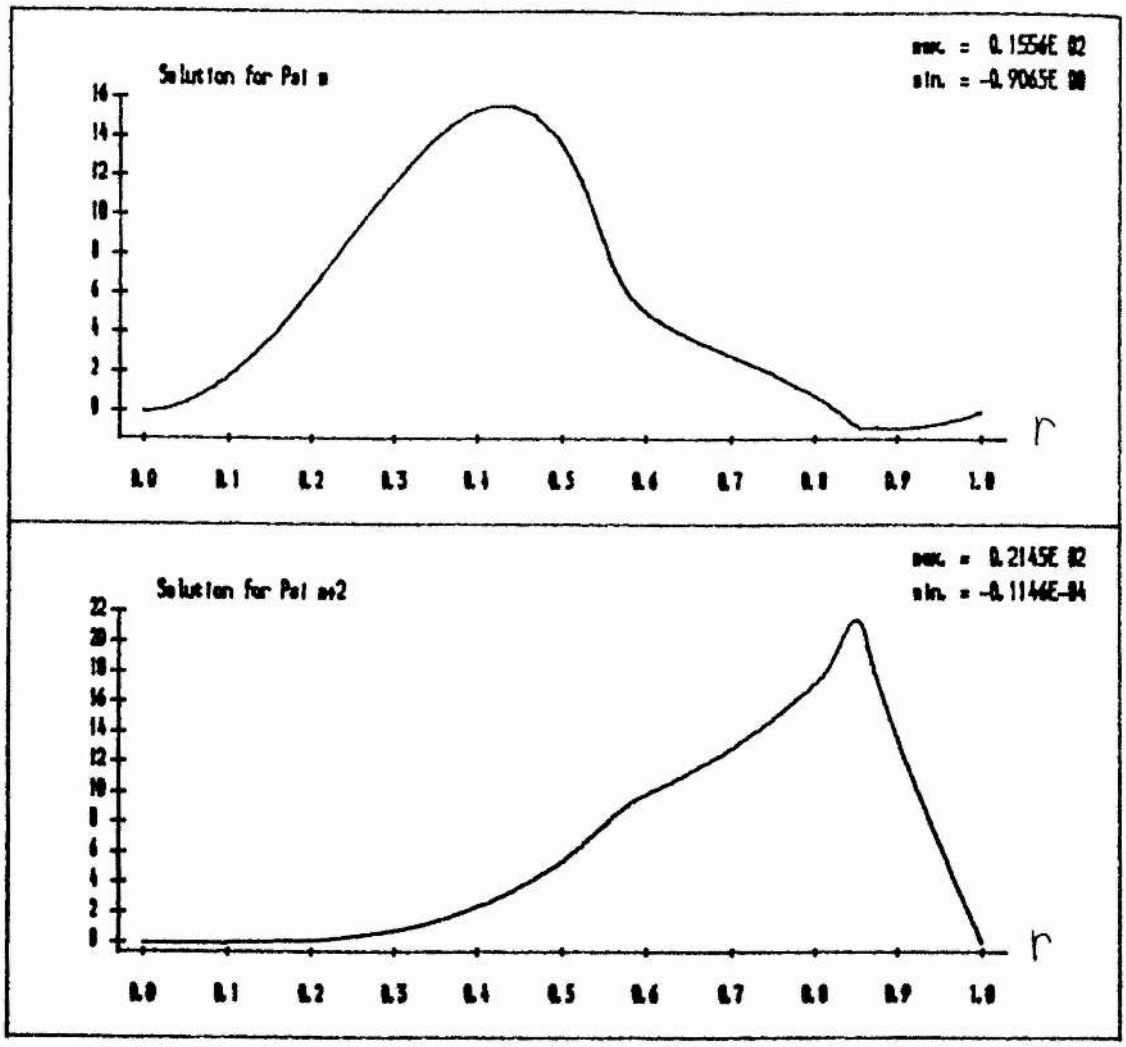

Figure 3.18(a). Coupled tearing: Ψ functions for central mode m=2 and q shown in fig. 3.13.; ε=0.15, Δ_4'/Δ_2'=1.0.

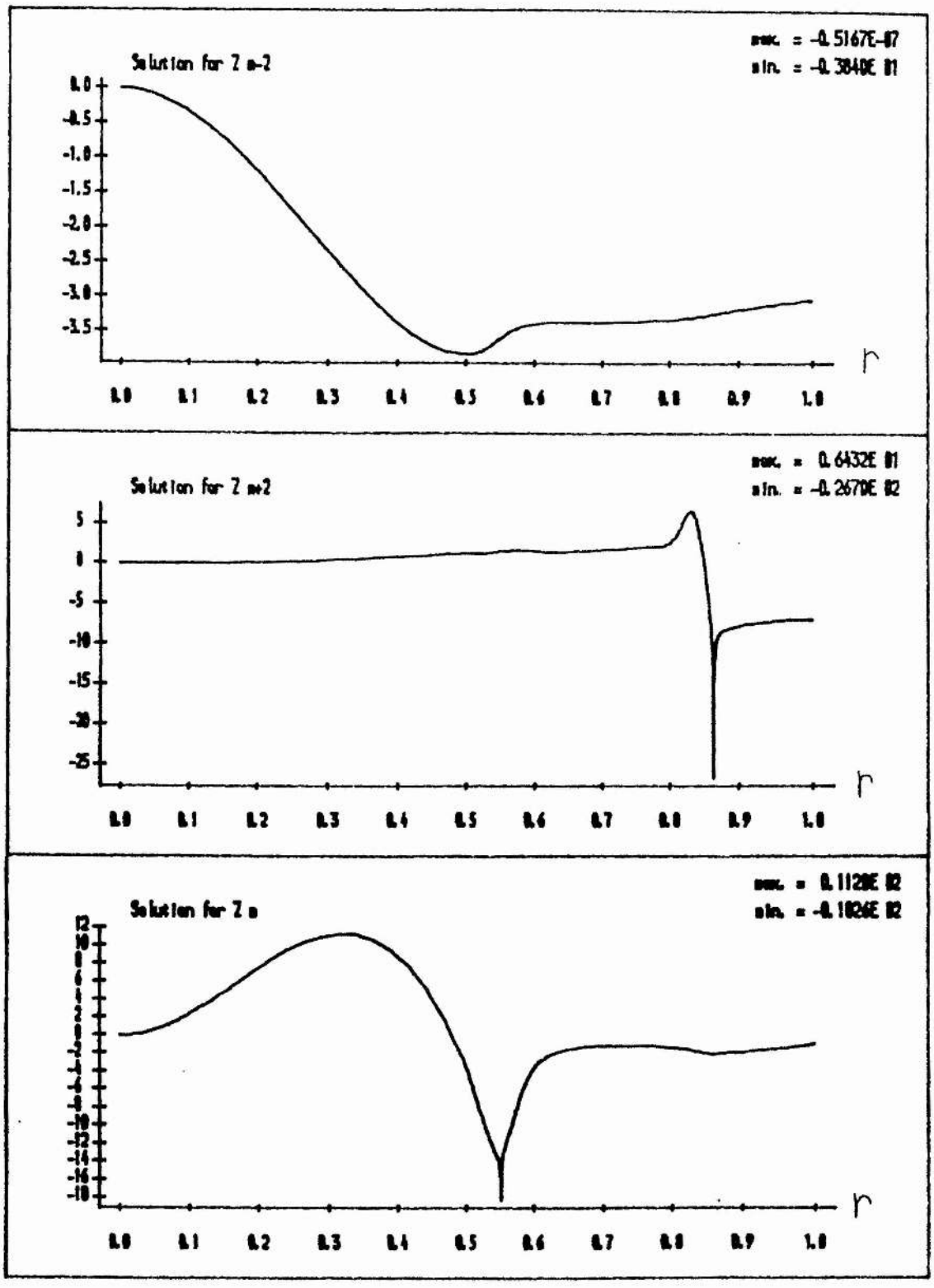

Figure 3.18(b). Coupled tearing: z functions for central mode m=2 and q shown in fig. 3.13.; ε=0.15, Δ_4'/Δ_2'=1.0.

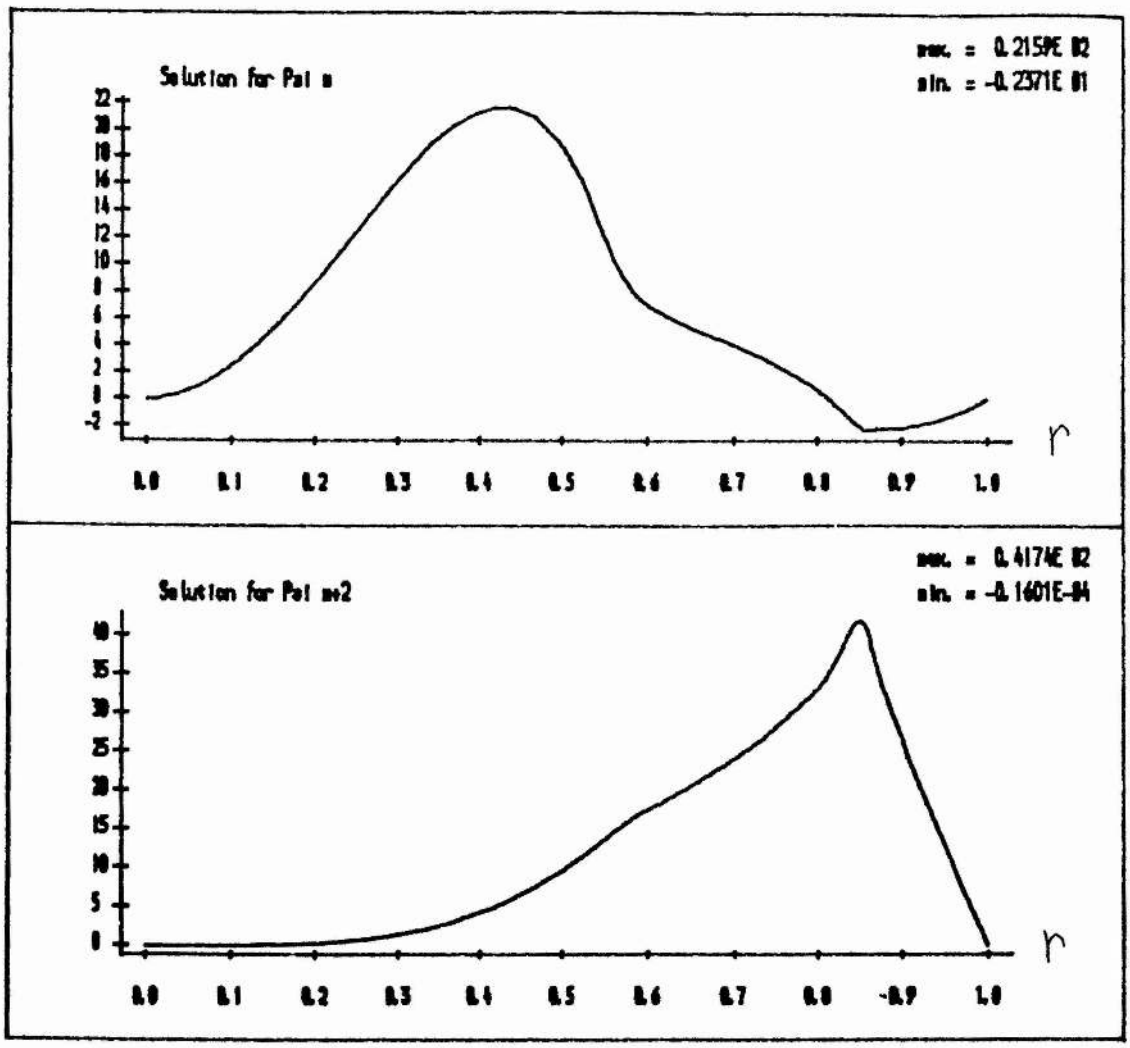

Figure 3.19(a). Coupled tearing: Ψ functions for central mode m=2 and q

shown in fig. 3.13.; ε=0.15, Δ_4'/Δ_2'=5.0.

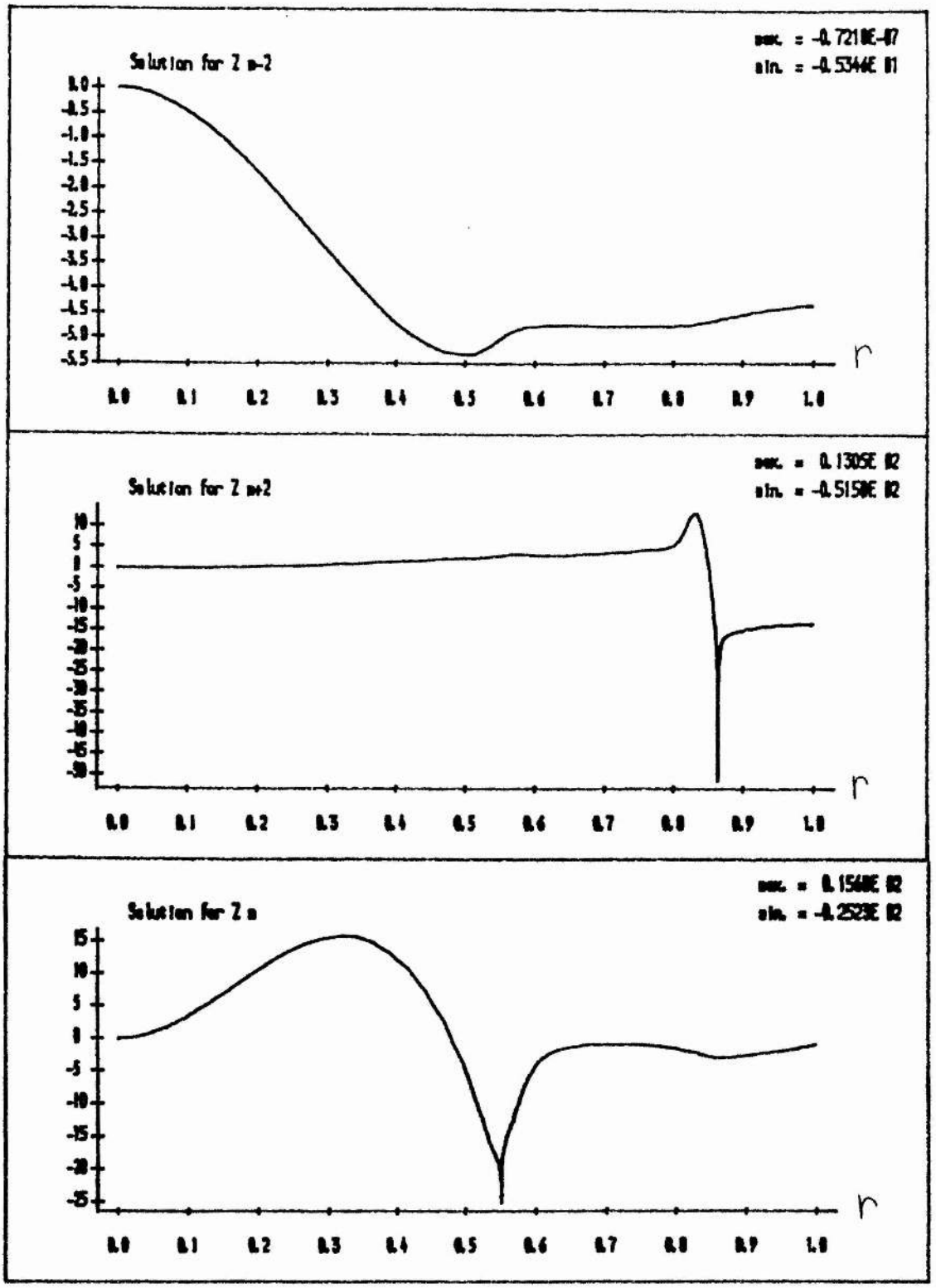

Figure 3.19(b). Coupled tearing: z functions for central mode m=2 and q shown in fig. 3.13.; ε=0.15, Δ_4'/Δ_2'=5.0.

both surfaces in all 6 equations. Hence, all 3 modes may have discontinuous derivatives at the two singular surfaces.

Unfortunately, the method of solution was rather costly in terms of computational resources. The inclusion of more poloidal modes and/or singular surfaces in the plasma, though a straightforward extension, would be impractical. The code was approximately forty times slower than comparable shooting codes, developed for the case of toroidal coupling (Martin). However, the finite difference code need only be run once to obtain a solution. Shooting codes should be converged by several runs at different step-lengths to ensure an accurate solution. The method used also has the advantage of giving global error estimates, which indicate the overall quality of the solution.

4.1 Introduction and Review of Previous Work.

The magnetic field of the solar corona is thought to consist of flux which has emerged from the denser photosphere. Consequently, the evolution of coronal magnetic fields is determined by the motions of photospheric footpoints in response to fluid motion generated, for example, by convection. Since the bulk of the corona is effectively perfectly conducting, the topology of the magnetic field will only change if current sheets are formed. In addition, the low coronal plasma beta means that any static magnetic field must be force-free to a large extent.

Observations of coronal loops indicate that they are essentially toroidal in shape and have a constant cross-section along their length. Furthermore, the length is typically ten times the width and so the aspect ratio is usually large. The commonly used simplification is to restrict attention to straight cylindrical loops with the main justification for this approach being that an expansion of the toroidal force-free equation, in powers of the inverse aspect ratio, generates the straight cylinder as the leading approximation.

Parker (1979) has investigated the twisted flux tube confined by an external pressure. Consider an axisymmetric flux tube which is also uniform along its length. In this case, we can deduce from

$$\nabla.\mathbf{B} = 0 \qquad (4.1)$$

that the field has no radial component. The appropriate form of the equilibrium equation is

$$\frac{B_\theta^2}{r} + \frac{d}{dr}\left(p + \frac{B_\theta^2 + B_z^2}{2}\right) = 0 \qquad (4.2)$$

and we may specify the equilibrium by a generating function F(r), equal to the total pressure. The field components are

$$\frac{B_z^2}{2} = F(r) + \frac{r}{2}\frac{dF}{dr} - p(r) \; ; \; B_\theta^2 = -r\frac{dF}{dr} \qquad (4.3)$$

and F satisfies $F \geq 0$, $dF/dr \leq 0$ and $d(r^2F)/dr \geq 0$.

For a force-free flux tube of radius R, confined by a constant external pressure P_e, we may show that

$$\langle B_z^2 \rangle = F(R) = P_e \qquad (4.4)$$

where <A> denotes the value of A, averaged over the volume of the tube. The introduction of twist to the field will cause the initially uniform B_z to decline from a maximum on the axis. However, since $\langle B_z^2 \rangle$ is constant, this must result in a decrease in $\langle B_z \rangle$. Since longitudinal flux is conserved, the flux tube as a whole must expand when twisted. However, $B_z(0)$ increases with increasing twist, indicating a compression of the field near the axis of the flux tube. Parker also considered a flux tube confined by a pressure varying along its length. The tube expands where the pressure is lower and contracts where it is higher. Modelling a flux tube with uniform pressure in $z < -h$ and a different uniform pressure in $z > h$, it is possible to obtain information from the conservation of longitudinal flux and the constancy of rB_θ along a field line. Where the tube undergoes extreme expansion, the twist becomes very large and where it undergoes extreme compression, the twist becomes very small. Browning and Priest (1983) examined the 2-D slender flux tube, including a radial field B_r. They were able to extend Parker's results to this case, noting that the expansion caused by a small twist was a second order quantity.

Zweibel and Boozer (1985) considered a 2-D cylindrical flux tube, line-tied at its photospheric footpoints. Using flux co-ordinates, they established a general formulation for the response of such a flux tube to slow photospheric motions. The resulting non-linear partial differential equation was, however, rather difficult to solve. They, instead, examined the simpler

problem of a linear twisting generated at the footpoints. As an example, they solved the case of a Gaussian twist profile, extending to infinity, with a decay length of 0.07 times the loop length. (In our analysis, we prefer profiles where the twist is limited to a finite radius, believing these to be more physically relevant.) They found an inward movement of field lines at small radii, but little movement of field lines beyond the decay radius of the Gaussian. We shall solve the Grad-Shafranov equation, an approach which is simpler than that of Zweibel and Boozer, but which is equivalent in the linear regime.

4.2 Mathematical Development.

We wish to investigate the response of an initially uniform cylindrical field to twisting of its endpoints. The gradual twisting of the magnetic footpoints results in the field evolving through a series of equilibrium configurations, satisfying

$$(\nabla \times \mathbf{B}) \times \mathbf{B} = \mu \nabla p \qquad (4.5)$$

with force-free fields being obtained when the right-hand side of (4.5) is negligible. Any axisymmetric field (i.e., independent of the azimuthal co-ordinate, θ) may be expressed in terms of a flux function A, such that

$$B_r = -\frac{1}{r}\frac{\partial A}{\partial z} \; ; \; B_\theta = \frac{1}{r}K(A) \; ; \; B_z = \frac{1}{r}\frac{\partial A}{\partial r} \; ; \; p = P(A) \qquad (4.6)$$

where K and P are arbitrary functions of A. The function K is determined by the footpoint displacement and, in the linear case, it is straightforward to derive its form. This field automatically satisfies (4.1) and the three components of (4.6) reduce to the single Grad- Shafranov equation:

$$\frac{\partial^2 A}{\partial r^2} - \frac{1}{r}\frac{\partial A}{\partial r} + \frac{\partial^2 A}{\partial z^2} + K\frac{dK}{dA} + r^2\mu\frac{dP}{dA} = 0 \qquad (4.7)$$

A is a useful quantity, since the projections of the field lines on the r-z plane are given by contours of constant A. The above equation for A is, in general, non-linear. We shall solve the linearised form of (4.7) with P(A) = 0. However, we may include P(A) by a simple

extension of the methods used and, where appropriate, the necessary alterations are indicated.

An initially uniform axial field B_o of length L corresponds to

$$A_o = B_o \frac{r^2}{2} \tag{4.8}$$

Now, by twisting the endpoints of the field (i.e., by having a non-zero azimuthal displacement, ξ_θ, at the footpoints) a small azimuthal component can be added. Define the azimuthal field at the endpoints by

$$B_\theta|_{z=0} = B_\theta|_{z=L} = \varepsilon B_o f(r) \tag{4.9}$$

where ε is a small parameter, which describes the amount of twist. For small twist B_θ is directly proportional to the footpoint displacement, ξ_θ, by

$$B_\theta = B_o \frac{\partial \xi_\theta}{\partial z} \tag{4.10}$$

where, from the linearised equations of motion, it can be shown that the azimuthal displacement is

$$\xi_\theta = \varepsilon f(r) z \tag{4.11}$$

(4.6) requires that

$$B_\theta|_{z=0} = \frac{1}{r} K\left(B_o \frac{r^2}{2}\right) \tag{4.12}$$

Thus, in this case, the function f(r) determines the form of K. Expressing A as $A_o + \varepsilon^2 A_1$, the linearised form of (4.7) becomes

$$\frac{\partial^2 A_1}{\partial r^2} - \frac{1}{r}\frac{\partial A_1}{\partial r} + \frac{\partial^2 A_1}{\partial z^2} + \left(K \frac{dK}{dA}\right)\Big|_{A=A_o} = 0 \tag{4.13}$$

subject to the boundary conditions

$$A_1|_{z=0} = A_1|_{z=L} = 0 \tag{4.14}$$

With the additional boundary condition

$$A_1|_{r=a} = 0 \tag{4.15}$$

for some radius a, we may solve (4.13) by a Fourier-Bessel series. The outer radius a is taken as finite but large for computational reasons. Varying the outer radius does not alter the results once a is larger than the radius of the tube. The complementary function for

(4.13) is

$$A_1 = rJ_1(\lambda r)\left[C_1 \cosh(\lambda z) + C_2 \sinh(\lambda z)\right] \qquad (4.16)$$

where J_1 is the Bessel function of the first kind (Abramowitz and Stegun (1972)). In order to satisfy the boundary condition (4.15) the values of λ are restricted and the ratio C_1/C_2 is determined by (4.14). Hence, the following series for A_1 automatically satisfies the boundary conditions

$$A_1 = r\sum_{n=1}^{\infty} a_n J_1(Nr)\left(\frac{\cosh N(z-L/2)}{\cosh(NL/2)} - 1\right) \qquad (4.17)$$

where $N = \alpha_n/a$ and α_n is the nth zero of J_1. Substituting (4.17) into (4.13) and using the orthogonality property of J_1 gives

$$a_n = \frac{-2}{J_0^2(\alpha_n)\,\alpha_n^2}\int_0^a f(r)\,\frac{d(rf(r))}{dr}\,J_1(Nr)\,dr \qquad (4.18)$$

In a similar way, the effects of a small change in the base pressure can be simulated. If

$$p|_{z=0} = p|_{z=L} = \varepsilon^2 p(r) \qquad (4.19)$$

then the function P(A) is easily determined and the only change to the above analysis is that f(r) d(rf(r))/dr is replaced by $r\mu$ dp/dr in (4.18).

Having calculated a solution for A_1, we may determine the flux surfaces by calculating the movement of the initially straight field lines from

$$A(r_o+\delta r) \approx A_o(r_o) + \varepsilon^2 A_1(r_o) + \delta r\, A_o'(r_o) \qquad (4.20)$$

Since the flux function is constant along a field line, the change in radius is simply given by

$$\delta r = -\varepsilon^2 \frac{A_1}{r} \qquad (4.21)$$

The linearisation is invalidated if the field lines cross anywhere, so we require

$$r_o + dr + \delta r(r_o+dr) > r_o + \delta r(r_o) \qquad (4.22)$$

Hence, ε must never be so large as to violate the condition

$$\frac{\partial(\delta r)}{\partial r} > -1 \qquad (4.23)$$

4.3 Example Twist Profiles and Results.

As a first example, consider the following form of f(r):

$$f(r) = \begin{cases} r(1-r^2), & r \le 1, \\ 0, & r > 1. \end{cases} \qquad (4.24)$$

This represents a twist (= f(r)/r) within a finite radius, decreasing monotonically from r = 0 out to r = 1. In this case, (4.18) may be evaluated analytically to yield the result

$$a_n = \frac{8N^{-6}}{J_0^2(\alpha_n)\alpha_n^2}\left[J_0(N)(192N-12N^3) + J_1(N)(-384+72N^2-N^4)\right]$$

$$= \frac{-8N^{-2}}{J_0^2(\alpha_n)\alpha_n^2} J_5(N) \qquad (4.25)$$

using the Bessel function addition formula. In general, a numerical integration scheme is required to evaluate the a_n. Taking the outer radius as 5 is found computationally convenient and agrees well with results for higher values of a. Truncation of the series at fifty terms is ample for convergence at this value. Typical field line plots are shown in Figure 4.1. The rather large value $\varepsilon = 2.8$ has been taken in order to make the effects easily visible. The field lines move inwards within the radius of the twist, but are virtually unaffected outside it, except for a very small expansion near the ends of the loop, just outside the twisted region. The compression is a maximum at the middle of each flux surface, with the largest effect at a radius of 0.378. The radial variation of the maximum compression is shown in Figure 4.2. As one would expect, shortening the tube reduces the amount of compression and increasing its length has the opposite effect. The most striking feature of the solutions is that variations in radius are restricted to narrow boundary layers near the ends of the tube, while the majority of the tube has almost constant cross-section.

Our results are qualitatively similar to those of Zweibel and

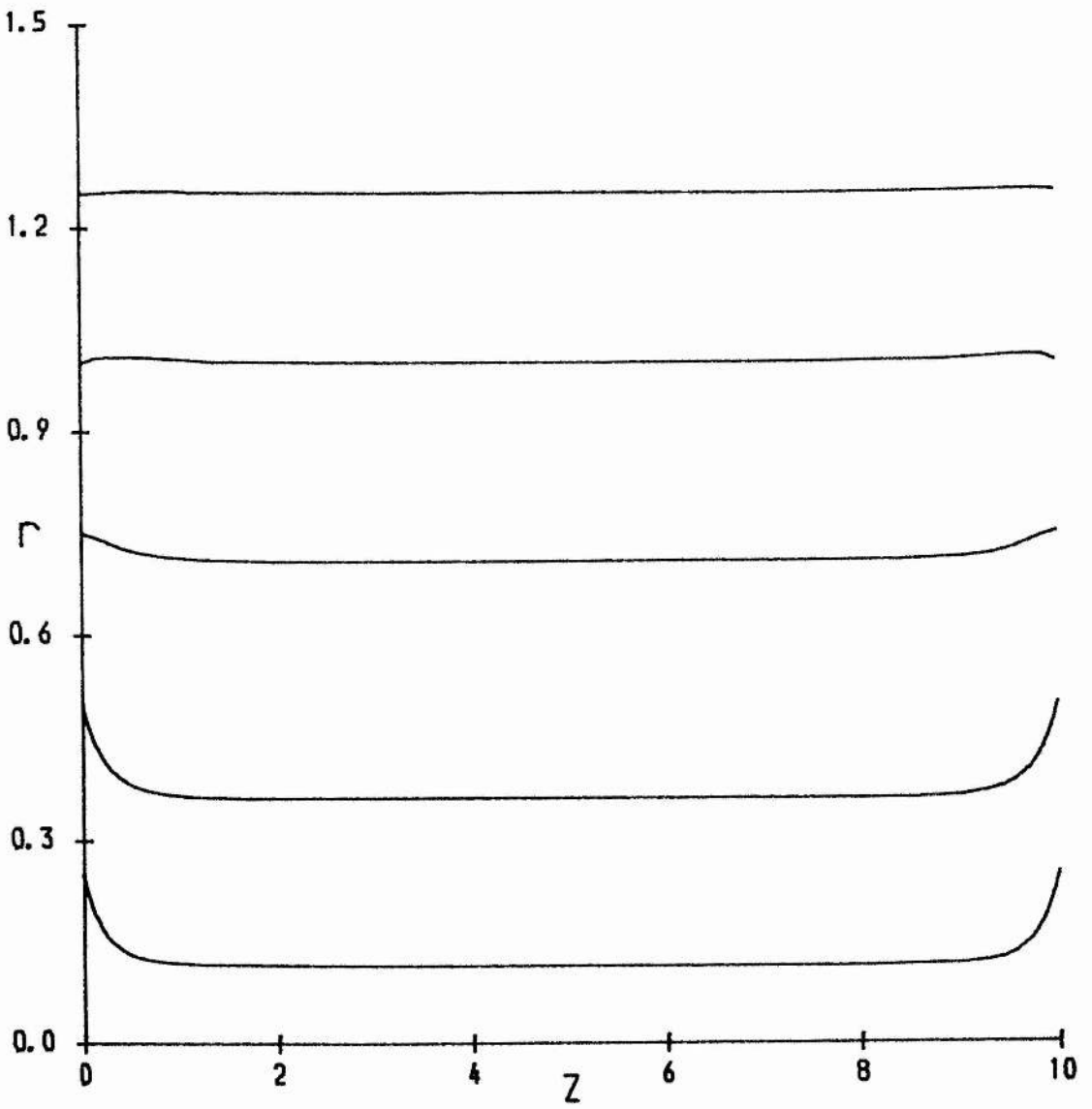

Figure 4.1. Flux surfaces for twist given by Equation (4.24).

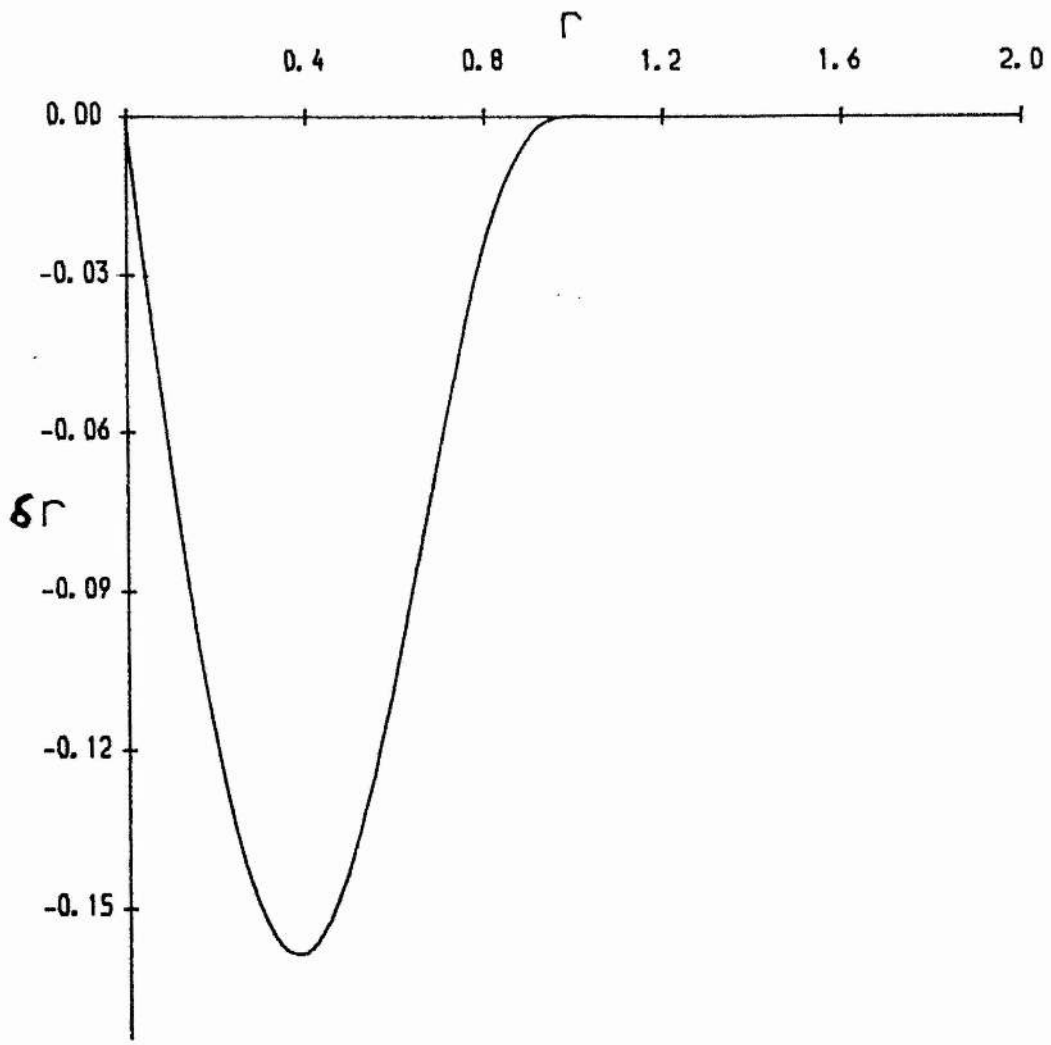

Figure 4.2. The change in radius, δr, of the flux surfaces in Figure 4.1 from the equilibrium value at the middle of the loop.

Boozer. As a check on our method, we apply it to their Gaussian twist profile, which corresponds to

$$f(r) = \frac{12.7\pi}{L} r \exp(-r^2/2) \qquad (4.26)$$

where the length of the tube was L=20. The resulting flux surface plot (Figure 4.3) is identical to their results. The maximum compression occurs at r=0.7 and there is very little effect outside the decay radius of the Gaussian ($r = \sqrt{2}$). The presence of boundary layers in the z-direction is again clearly evident. A more general Gaussian twist profile with its maximum displaced from r=0 is given by

$$f(r) = r \exp[-(r-\rho)^2/2] \qquad (4.26)$$

This profile produces results which are qualitatively similar to the undisplaced Gaussian. However as ρ is made larger, the compression increases, due to the larger azimuthal fields corresponding to the same value of twist. In addition the position of maximum compression moves outwards. For example, when ρ=1, the maximum compression occurs at r=1.13.

4.4 Comparison with Early Work.

It is interesting to compare these results with Parker's 1-D model. The compression of the inner part of the field is obvious, but the expected expansion of the outer part of the tube is not apparent. This is, however, consistent with the Browning and Priest result that this is a small quantity for a weakly-twisted, slender flux tube. The modification to B_θ caused by the compression can be obtained from the relation

$$K(A) = K(A_o) + A_1 \frac{dK}{dA_o} \qquad (4.28)$$

Hence, the twist per unit length of the new configuration is given by

$$\frac{\partial \Phi}{\partial l} = \frac{B_\theta(r_o)}{r_o B_o} \left(1 + \varepsilon^2 r \frac{\partial}{\partial r}\left(\frac{\delta r}{r}\right)\right) \qquad (4.29)$$

which represents an increase in the twist, with most twist at the middle of each flux surface. The effect is most pronounced where

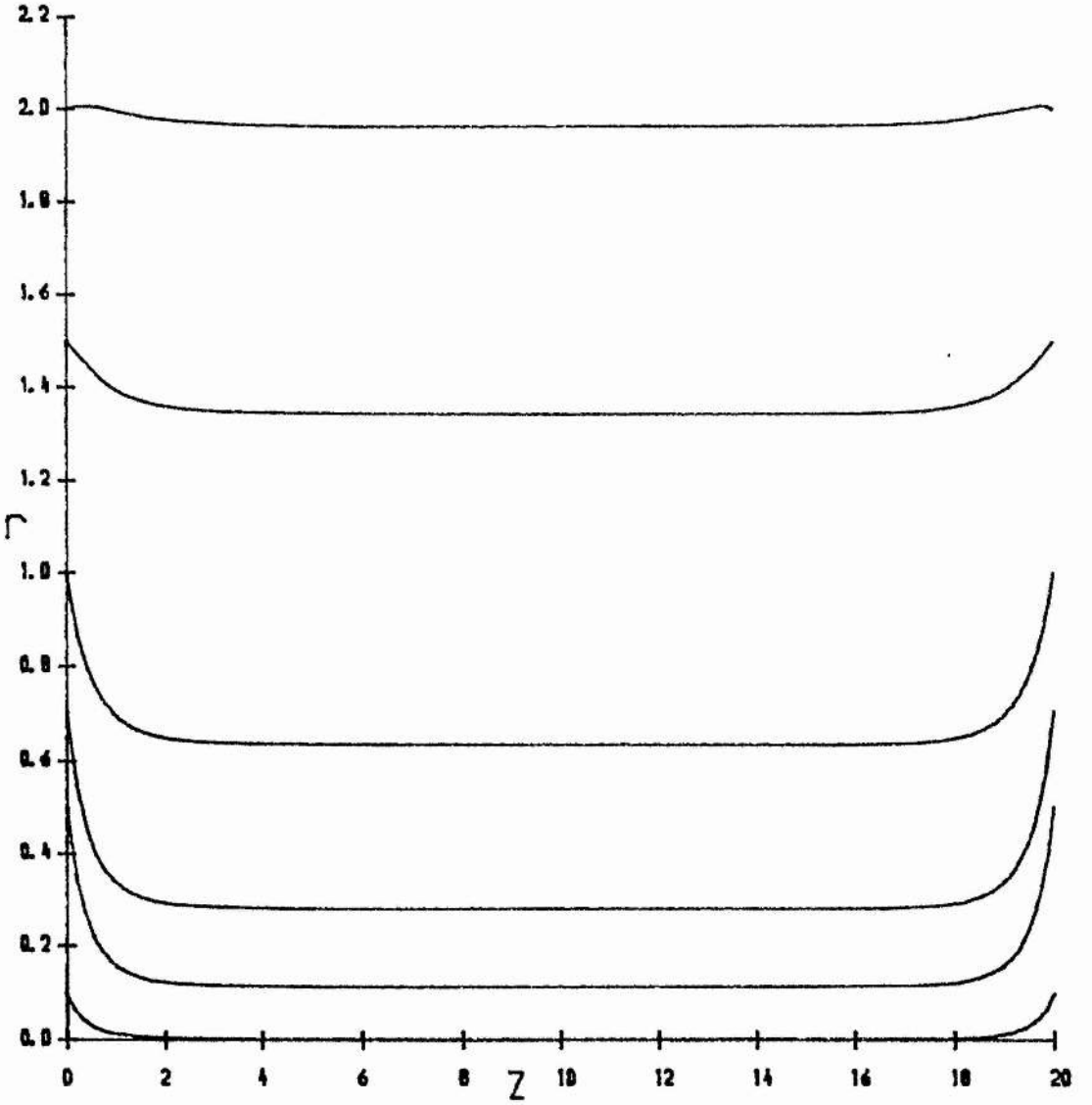

Figure 4.3. Flux surfaces for Gaussian twist.

$\partial(\delta r)/\partial r$ is positive. This behaviour contrasts with Parker's result that twist accumulates on the thicker part of the tube, in order to balance tension forces. However, Parker's result occurs in the asymptotic limit of a large difference in radius, whereas the linear analysis necessarily presupposes a small variation in radius. In addition, the force balance for a continuous variation of radius is more complex than a simple balance of tension. Hence, there is no contradiction.

4.5 Boundary Layer and 1-D Approach.

The Fourier-Bessel approach is particularly helpful in explaining the boundary layer structure of the solutions. From (4.17), it can be seen that, for large values of NL/2, the z dependence decays exponentially away from the boundary. An estimate of the boundary-layer thickness is easily obtained. The coefficients a_n initially increase in magnitude as n increases, until a maximum is reached at say, n = m. For larger values of n, the coefficients rapidly decrease in magnitude. Taking N corresponding to the largest coefficient and, hence, the dominant term in the solution, the structure of the boundary layer is represented by

$$\frac{\cosh N(z-L/2)}{\cosh(NL/2)} = \cosh(Nz) - \tanh(NL/2)\sinh(Nz) \qquad (4.30)$$

Since $\tanh(NL/2) \approx 1$, for large L, δr reaches 90% of its maximum value after a distance $z \approx 2/N$. Thus, for $L >> 1$, the boundary layer thickness is independent of the loop-length.

The above comments are best illustrated by a simple example. Assume that f(r) is selected in such a way that all $a_n = 0$ except for a_1 (The required function is, in fact

$$f(r) = \left[J_0(\alpha_1 r/a) - \frac{2a}{\alpha_1 r} J_1(\alpha_1 r/a) \right]^{\frac{1}{2}} \qquad (4.31)$$

which is of no particular physical significance.). (4.17) reduces to

$$A_1 = a_1 r J_1(Nr) \left(\frac{\cosh N(z-L/2)}{\cosh(NL/2)} - 1 \right) \qquad (4.32)$$

where N is simply α_1/a. The z-dependence of A_1 is shown in Figure 4.4 for length to width ratios between L = 1 and L = 10. It is seen, for example, that with L = 4, approximately 27% of the loop's length is constant in radius (A_1 within 1% of maximum value), whereas for L = 10, over 70% is straight. In general, the dominant coefficient in the series is not the first but occurs for a higher value of n. Since $N=\alpha_n/a$, it becomes larger for larger n and the boundary layer will be correspondingly narrower than in the above example. Hence, it is clear that a large fraction of a long loop is independent of the axial co-ordinate, z. The reason the boundary layer exists is that the variations that occur on the boundary on the scale of the loop radius can only 'propagate' the same distance into the loop. Hence, if the loop is much longer than its radius, the main variations will occur at the boundaries and the central part of the loop will remain straight. This is in agreement with a prediction made by Parker (1972).

The existence of the boundary layer allows us to model the main part of the loop as a 1-D flux tube, which has a flux function determined by the solution of (4.13) with the z-derivative set to zero. In other words, A_1 is given by the particular integral

$$A_1 = \int r \int \frac{G(s)}{s}\, ds dr \qquad (4.33)$$

where G(s) = -f d(sf)/ds for a twisted loop or -sμ dp/ds for the case of increased base pressure. The change in radius from the line-tied edges to the central part of the tube is given by (4.21).

This model may be checked against the 2-D results obtained earlier. For f(r) given by (4.24), the solution satisfying continuity of A_1 and its derivative at r = 1 is

$$A_1 = \begin{cases} \frac{r^2}{12}(1-r^2)^3, & r \le 1, \\ 0, & r > 1. \end{cases} \qquad (4.34)$$

The maximum compression can be shown to occur at $r^2 = 1/7$. This result agrees with Figure 4.2 and the fashion in which the 2-D

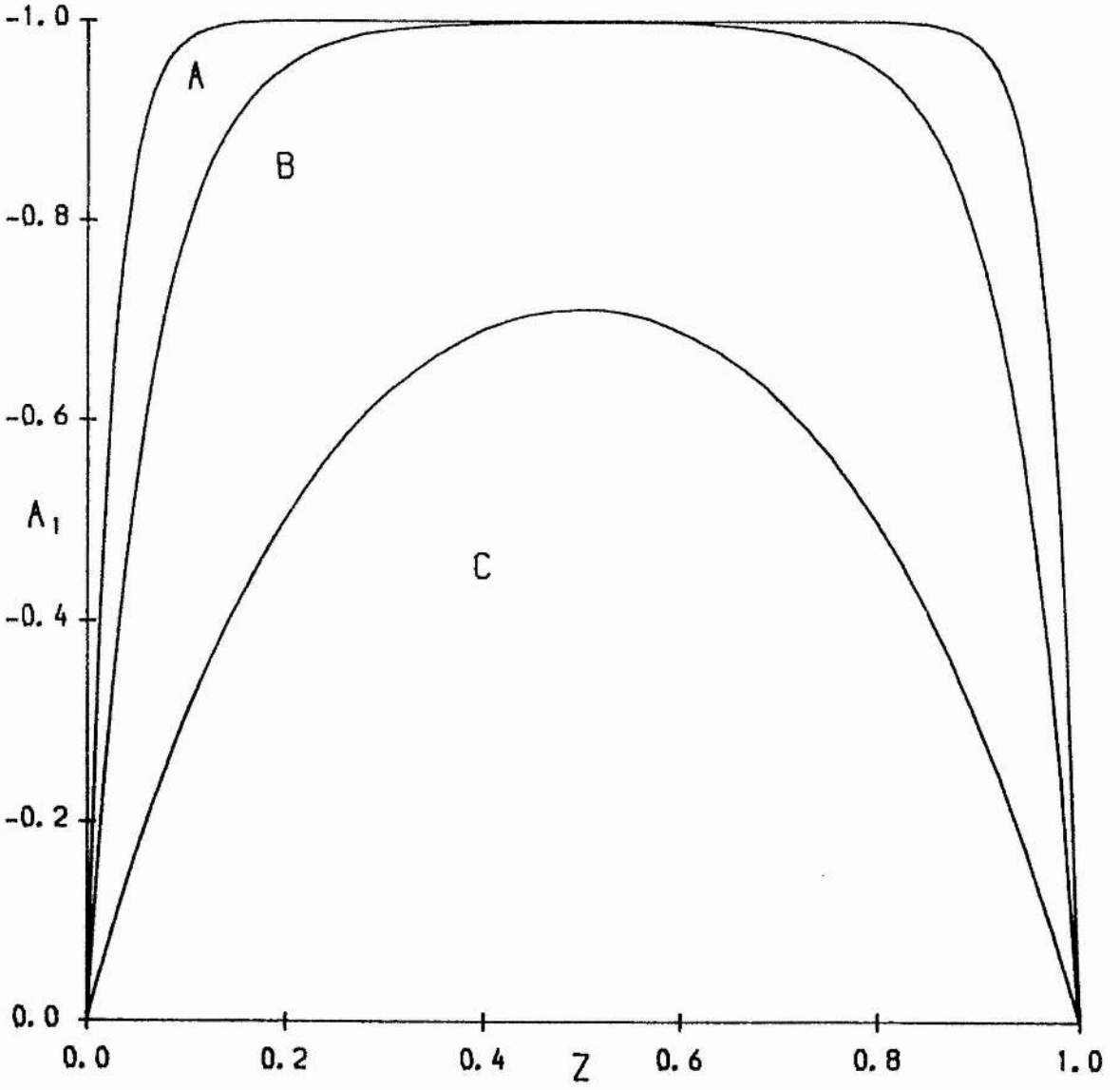

Figure 4.4. The axial dependence of the perturbed flux function A_1 for various loop lengths, namely, A: L=10, B: L=4, C: L=1. The boundary layer structure is clearly seen as L increases.

solution approaches this result as L becomes larger is shown in Figure 4.5. Zweibel and Boozer's result is also well-matched by the 1-D method, the result for A_1 being

$$A_1 = \frac{r^2}{4} \exp(-r^2) \tag{4.35}$$

Using this method, we may make analytic progress on a variety of other profiles. Firstly, consider the profile defined by

$$f(r) = \begin{cases} r\left(1 - [r - r_{max}]^2\right), & r \le 1 + r_{max} \\ 0, & r \ge 1 + r_{max} \end{cases} \tag{4.36}$$

This reduces to (4.24) when r_{max} =0. The change in radius of the field line over most of the loop is given by

$$\delta r = \frac{1}{r}\left(h(r) - h(1+r_{max}) \frac{r^2}{(1+r_{max})^2} \right), \quad r \le 1 + r_{max} \tag{4.37}$$

where

$$h(r) = \frac{(1 - r_{max}^2)^2}{4} r^4 + \frac{2r_{max}}{3}(1 - r_{max}^2) r^5 + (3 r_{max}^2 - 1)\frac{r^6}{4} - \frac{2r_{max}}{5} r^7 + \frac{r^8}{12} \tag{4.38}$$

This profile is similar to the displaced Gaussian twist and the variation of δr with r is shown in Figure 4.6. Again, the position and amount of maximum compression increase as r_{max} increases. Typically, we note that as r_{max} increases from 0 to 1.0, the position of maximum compression increase from r=0.378 to r=0.9 and δr increases by a factor of 18. Secondly, consider

$$f(r) = \begin{cases} r^{n+1}(1 - r^2) / [r_{max}^n (1 - r_{max}^2)], & r \le 1, \\ 0, & r \ge 1. \end{cases} \tag{4.39}$$

which confines the twist to remain within a radius of one, but allows the position of maximum twist to vary as n changes. The radius of maximum twist is $r_{max} = \sqrt{[n/(n+2)]}$. The change in radius of the tube is

$$\delta r = \frac{r}{4 r_{max}^n (1 - r_{max}^2)} \left[\frac{r^{2(n+1)} - 1}{n+1} - 2\frac{r^{2(n+2)} - 1}{n+2} + \frac{r^{2(n+3)} - 1}{n+3} \right] \tag{4.40}$$

out to r=1 and is zero beyond. Figure 4.7 shows the effect of

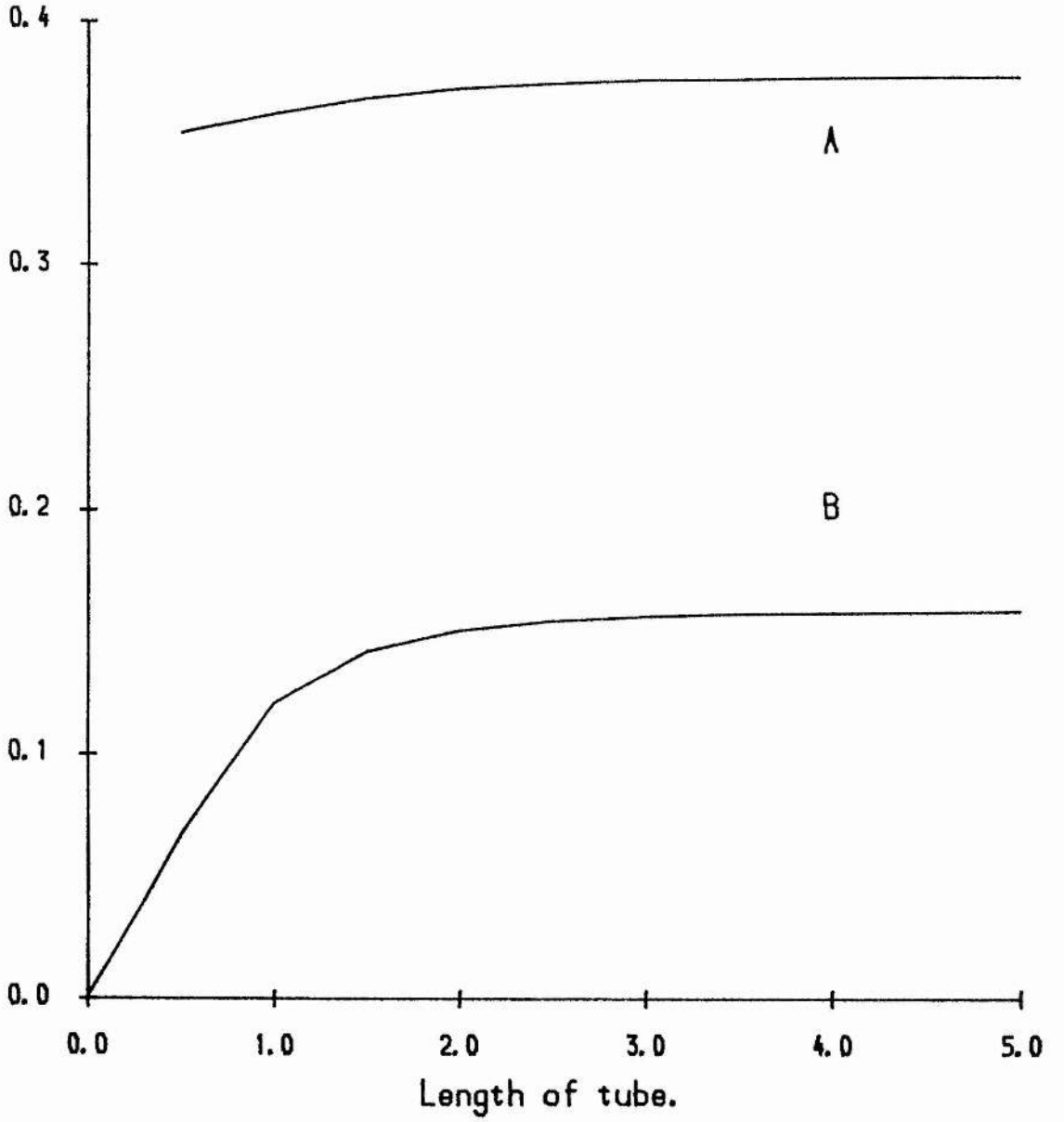

Figure 4.5. The radial position (A) and magnitude (B) of the maximum compression as a function of the loop length (in units of a).

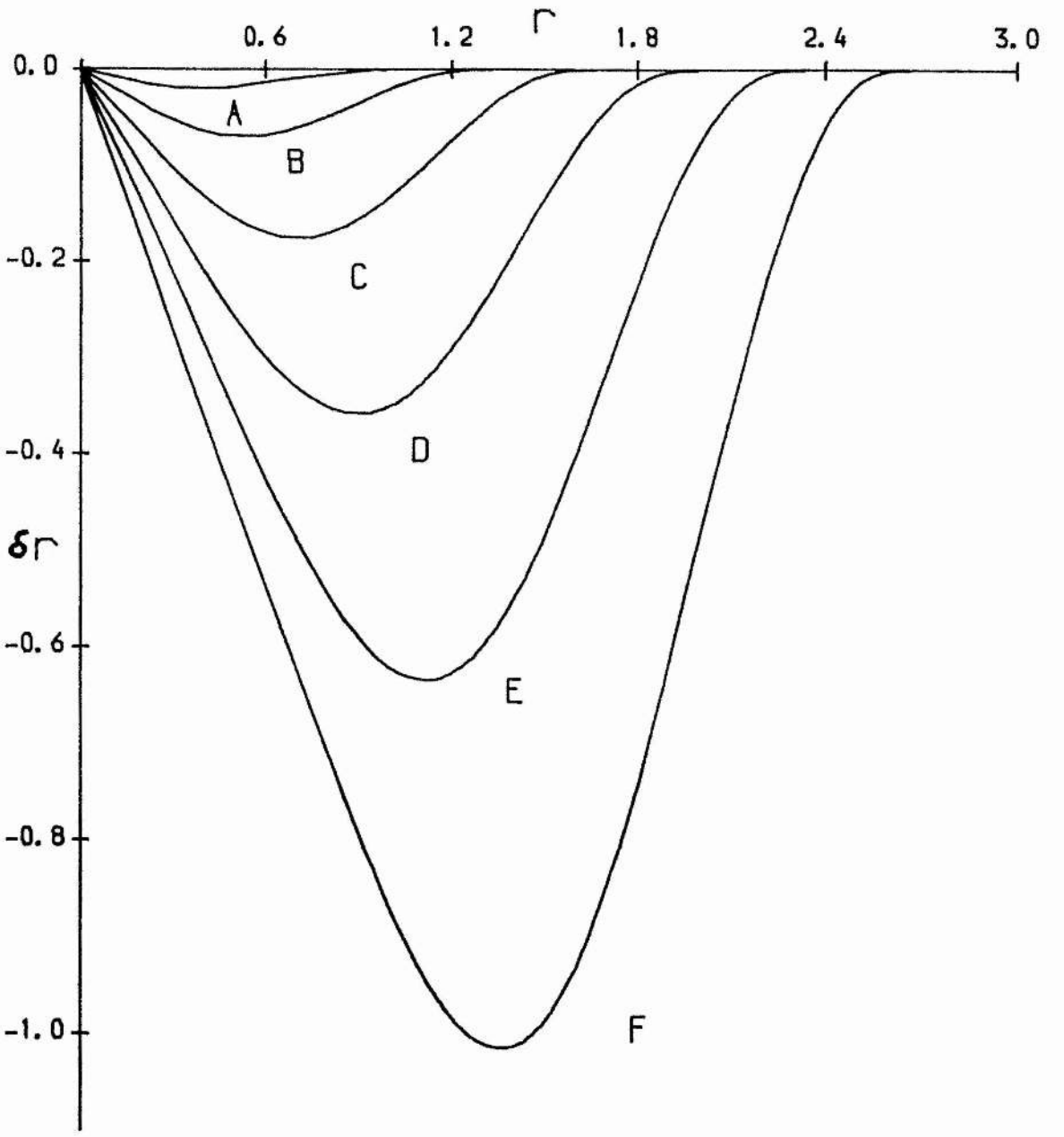

Figure 4.6. The change in radius of the flux surfaces as a function of r for the twist profile given by Equation (4.36) for various values of the parameter r_{max}, namely, A: 0.0, B: 0.3, C: 0.7, D: 1.0, E: 1.3, F: 1.7.

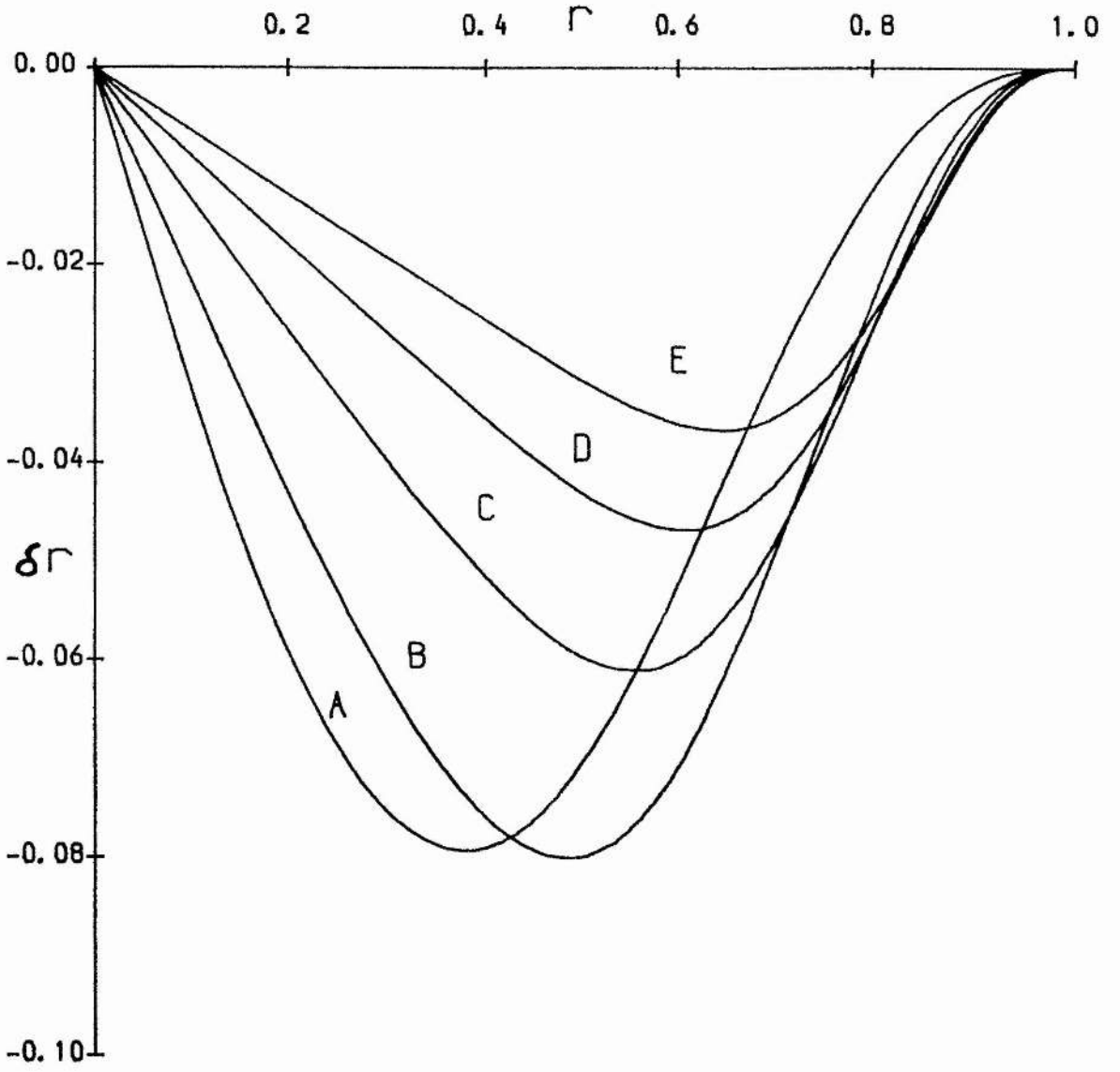

Figure 4.7. The change in radius of the flux surfaces as a function of r for the twist profile given by Equation (4.39) for various values of the parameter n, namely A: 0, B: 1, C:2, D: 3 , E: 4.

increasing n on this profile. In this case, as n increases the position of maximum compression increases, but its magnitude firstly increases slightly then decreases. This is because, at high n, the twist is highly localised at $r_{max,}$ which is close to the edge of the loop.

Steinolfson and Tajima (1987) have studied the 2-D non-linear development when there is a continuous twisting motion on the photospheric boundary. There is qualitative agreement with Zweibel and Boozer and this work in the early stages. However, at later times the twisting becomes so pronounced that a rapid change occurs in the magnetic field configuration, with the field completing several rotations along the length of the loop. Such a high degree of twisting would suggest that a 3-D kink mode instability is excited, as discussed by Hood and Priest (1979). Steinolfson and Tajima chose a twisting photospheric velocity that gives rise to an azimuthal field profile described by

$$f(r)=\begin{cases} r, & 0 \le r \le 0.75, \\ 3(1-r) & 0.75 \le r \le 1, \\ 0, & r \ge 1. \end{cases} \qquad (4.41)$$

when the twisting is slight. Although the loop length is only twice the radius of the tube, their results indicate that a substantial part of the tube has a constant cross-sectional area. The untied cylindrically-symmetric solution is given by

$$A_1 = \begin{cases} -\frac{r^4}{4} - \frac{9}{2}\left(\frac{1}{4} + \log\frac{3}{4}\right)r^2, & 0 \le r \le 0.75, \\ 9\left(-\frac{3r^2}{4} + r^3 - \frac{r^4}{4} - \frac{r^2}{2}\log r\right), & 0.75 < r \le 1, \\ 0, & r > 1. \end{cases} \qquad (4.42)$$

The position of maximum compression is at r = 0.476 and this form of A_1 agrees well with Steinolfson and Tajima's results for the linear phase.

4.6 Toroidal Effects.

The above results show that the twisted loop is to a large

degree well modelled by a cylindrically-symmetric field. We shall use this property to examine some simple consequences of the toroidal shape of the actual loop. The simplest way to proceed is to express the magnetic field in terms of flux co-ordinates, as in Chapter 2. Firstly, however, let us show that the boundary-layer features of the straight loop carry over to toroidal loops. Bending the cylindrical potential field described earlier into a semi-circle gives the new potential field as

$$\mathbf{B} = (0, B_0 R_0/R, 0) \tag{4.43}$$

where cylindrical co-ordinates (R,ϕ,Z) have been used and the photosphere is located at $\phi = \pm\pi/2$. The effect of twisting in the neighbourhood of the radius $R = R_0$ is best described in terms of Euler Potentials. The magnetic field may be written as

$$\mathbf{B} = B_0 \nabla\alpha \times \nabla\beta \tag{4.44}$$

where α and β are given by

$$\alpha = \log(R/R_0) + \alpha_1(R,\phi,Z) \; ; \quad \beta = -Z + R\beta_1(R,\phi,Z) \tag{4.45}$$

and α_1 and β_1 are understood to be small changes to the initial field (4.43). The equilibrium equation becomes, to first order,

$$\frac{1}{R}\frac{\partial}{\partial R}\left(R\frac{\partial\alpha_1}{\partial R}\right) + \frac{1}{R^2}\frac{\partial^2\alpha_1}{\partial\phi^2} = \frac{\partial^2\beta_1}{\partial R\partial Z} \tag{4.46}$$

and

$$\frac{1}{R^2}\frac{\partial^2\beta_1}{\partial\phi^2} + \frac{\partial^2\beta_1}{\partial Z^2} = \frac{1}{R}\frac{\partial}{\partial R}\left(R\frac{\partial\alpha_1}{\partial Z}\right) \tag{4.47}$$

The effect of twisting at the photospheric base can be modelled by prescribing the values of α_1 and β_1 there. However, it is now convenient to transform these equations into a local toroidal system that assumes that the twisting motion is localised about the radius R_0. If the twisting only extends to a distance a about the centre of the loop, we may define the inverse aspect ratio $\varepsilon = a/R_0$ as in Chapter 2. Our new (orthogonal) co-ordinate system is given by

$$r = \frac{\left[(R-R_0)^2 + Z^2\right]^{\frac{1}{2}}}{\varepsilon R_0} \tag{4.48}$$

and

$$\theta = \tan^{-1}\left(\frac{Z}{R_0-R}\right) \tag{4.49}$$

Using this change of variable, every R and Z derivative introduces a factor ε^{-1}. Hence, multiplying the final equations by ε^2 shows that terms involving ϕ derivatives are of the form $\varepsilon^2\partial^2/\partial\phi^2$. Thus, assuming that the length of the loop is much larger than its radius, we may expect to find boundary layers as in the cylindrical case. Since the main part of the toroidal loop is invariant in the ϕ direction, we now concentrate on loops which have constant cross-section. The flux co-ordinate formulation of Chapter 2 is appropriate. However, we shall only require $O(\varepsilon)$ terms in our analysis and the (r,θ,ϕ) system described by (4.48) and (4.49) is clearly the (r,θ,ϕ) system of Chapter 2 truncated to that order. The tokamak expansion should be appropriate for our weakly twisted field, which has the form

$$\mathbf{B} = R_0 B_0 \left(f(r)\nabla\phi \times \nabla r + g(r)\nabla\phi\right) \tag{4.50}$$

where

$$f/g = O(\varepsilon) \tag{4.51}$$

To understand the nature of the external plasma, consider such a field confined by an external fluid pressure p_e at r=a. The matching condition at the loop surface is

$$p_e(a) = \frac{B_0^2}{2}\left(1 + 2\varepsilon a\cos\theta + O(\varepsilon^2)\right) \tag{4.52}$$

Hence, due to the $\cos\theta$ dependence of the order ε term, *a constant external pressure cannot confine the magnetic field.* On the other hand, if f(r) falls to zero at a, the field may be constrained by a simple potential field in the outer region, given by

$$B = B_0 R_0\, g(a)\nabla\phi, \quad r > a. \tag{4.52}$$

Thus, the important conclusions reached are that toroidal coronal loops must be confined by an external magnetic field, perhaps potential in nature, and cannot be surrounded by a field-free region if the loop is to remain in equilibrium. These considerations motivate investigation of force-free loops, with twisting motions confined to a finite radius, such as that corresponding to the field profile given by (4.24).

In the following chapter, we shall examine the strongly twisted loop, bearing in mind the results of the present chapter.

5.1 Introduction.

As described in Chapter 4, coronal magnetic fields evolve in response to the motion of their photospheric footpoints. This process stores energy in the coronal magnetic field. If the field structure becomes unstable or a non-equilibrium situation develops, this energy may be released in the form of heat and motion. A gradual release of energy would contribute to the heating of the corona, whereas violent release corresponds to a flare. The two-ribbon flare occurs in arcade-type structures, while the less energetic compact flare is associated with coronal loops. In this chapter, we shall investigate whether the quasi-static evolution of a coronal loop leads to loss of equilibrium. In order to do this, we shall consider the non-linear phase of the twisting which we examined in Chapter 4.

We have shown that a long, weakly-twisted flux tube has a constant cross-section along most of its length. There is considerable evidence that this is also true of strongly-twisted tubes. In Steinolfson and Tajima's dynamical simulation, despite the shortness of their loop, the flux surfaces were straight over much of their length, even in the non-linear regime. At large times, the field showed highly dynamic behaviour, along with a dramatic increase in both magnetic and kinetic energies. This may indicate the development of an instability (either real or numerical) or a loss of equilibrium.

Browning and Hood (1989) solved the non-linear Grad-Shafranov equation and also obtained equilibria with almost constant radius over most of their length, at moderate aspect ratios. They observed that loops which carry finite current have flux surfaces which bow inwards everywhere. Such loops are not very relevant for our study,

since they imply footpoint movements extending to infinite radii. In contrast, loops which carry no net current have compressed flux in their centres and expanded outer flux surfaces. Hence, a region of depleted axial field develops as such a loop is progressively twisted.

Consider again the Grad-Shafranov equation (4.7), in the absence of pressure

$$\frac{\partial^2 A}{\partial r^2} - \frac{1}{r}\frac{\partial A}{\partial r} + \frac{\partial^2 A}{\partial z^2} + K\frac{dK}{dA} = 0 \qquad (5.1)$$

If we choose the form

$$K(A) = \lambda A \quad , A < 1 \qquad (5.2)$$

then (5.1) becomes

$$\frac{\partial^2 A}{\partial r^2} - \frac{1}{r}\frac{\partial A}{\partial r} + \frac{\partial^2 A}{\partial z^2} + \lambda^2 A = 0 \qquad (5.3)$$

which is linear, but describes the non-linear evolution of the loop. The axially-invariant solution is simply given by

$$A(r) = r\,\frac{J_1(\lambda r)}{2J_1(\lambda)} \qquad (5.4)$$

whereas the solution satisfying the boundary conditions

$$A|_{z=0} = A|_{z=L} = B_o\frac{r^2}{2} \;;\; A|_{r=1} = \frac{1}{2}B_o \;;\; A|_{r=0} = 0 \qquad (5.5)$$

is

$$A = r\,\frac{J_1(\lambda r)}{2J_1(\lambda)} + \sum_{n=1}^{\infty} a_n r J_1(\alpha_n r)\,\frac{\cosh(K_n(z - L/2))}{\cosh(K_n L/2)} \qquad (5.6)$$

where a_n is again the nth zero of J_1 and $K_n^2 = a_n^2 - \lambda^2$. The coefficients a_n are now given by

$$a_n = \frac{2}{J_0^2(\alpha_n)}\int_0^1 \left(\frac{r^2}{2} - r\,\frac{J_1(\lambda r)}{2J_1(\lambda)}\right) J_1(\alpha_n r)\,dr \qquad (5.7)$$

The boundary layer feature is again seen in (5.6). For long loops, $K_n L >> 1$, the axially-dependent part of the solution decays exponentially away from the edges, leaving the form (5.4) over most of the loop. Notice that the boundary condition at r =1 is not crucial to the conclusion. This boundary layer is clearly seen in the work of Steinolfson and Tajima (1987) and Browning and Hood (1989). As an

illustration of this, figure 5.1 has been taken from the latter paper. These show the flux surfaces obtained from a non-linear analysis of the twisted flux tube. In both sections of the figure, the boundary layers and the 1-D part of the loop are clearly visible. In 5.1(a), the loop, which has an inverse aspect ratio of 0.18, is behaving in the fashion predicted by the linear analysis. Note that, whereas the inner part of the field is compressed, the field at the loop edge (marked by a cross) is almost unmoved. For the shorter (inverse aspect ratio of 0.48), more twisted loop in 5.1(b), the edge of the loop has expanded and the region of depleted B_z is obvious.

Since we expect the behaviour of the main part of our loop to be essentially 1-D, we can use the 1-D Grad-Shafranov equation

$$\frac{d^2A}{dr^2} - \frac{1}{r}\frac{dA}{dr} + K\frac{dK}{dA} = 0 \qquad (5.8)$$

as in the previous chapter.

5.2 Twisting field with form of K specified.

To investigate the non-linear regime, we shall specify $K(A)=\lambda k(A)$, where λ is a (positive real) parameter and $k(A)$ is some specified function of A. We wish to know if there is a value of λ for which we cannot solve the equilibrium equation. The 1-D equation is

$$\frac{d^2A}{dr^2} - \frac{1}{r}\frac{dA}{dr} = -\lambda^2 k\frac{dk}{dA} \qquad (5.9)$$

Note that the LHS of (5.9) is equal to $r(B_z)'$. Consider a k-profile which simply rises from zero on the magnetic axis to a maximum and then falls to zero again at r=1. In this case, the minimum B_z will be given by

$$B_z(r_m) = B_o + \lambda^2 \int_{r_m}^{r_e} \frac{1}{r} k\frac{dk}{dA}\,dr \qquad (5.10)$$

where B_o is the value of the untwisted uniform field, r_m is the radius of minimum B_z and r_e is the radius of the loop edge. Since k dk/dA is negative everywhere in the region of integration, a sufficiently

(a)

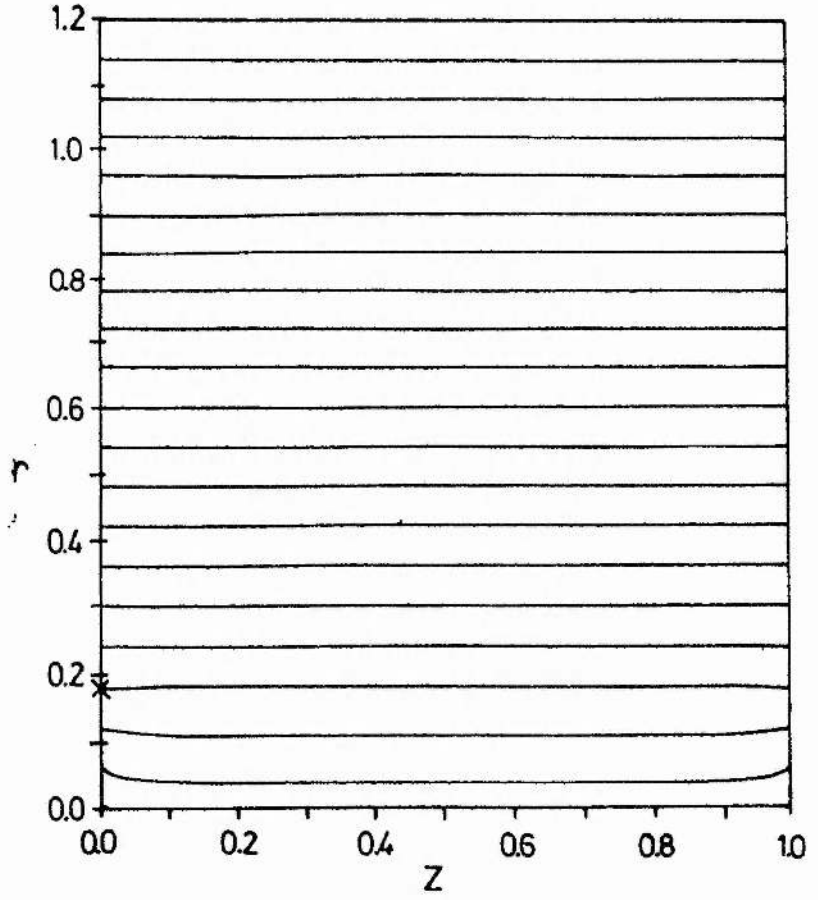

(b)

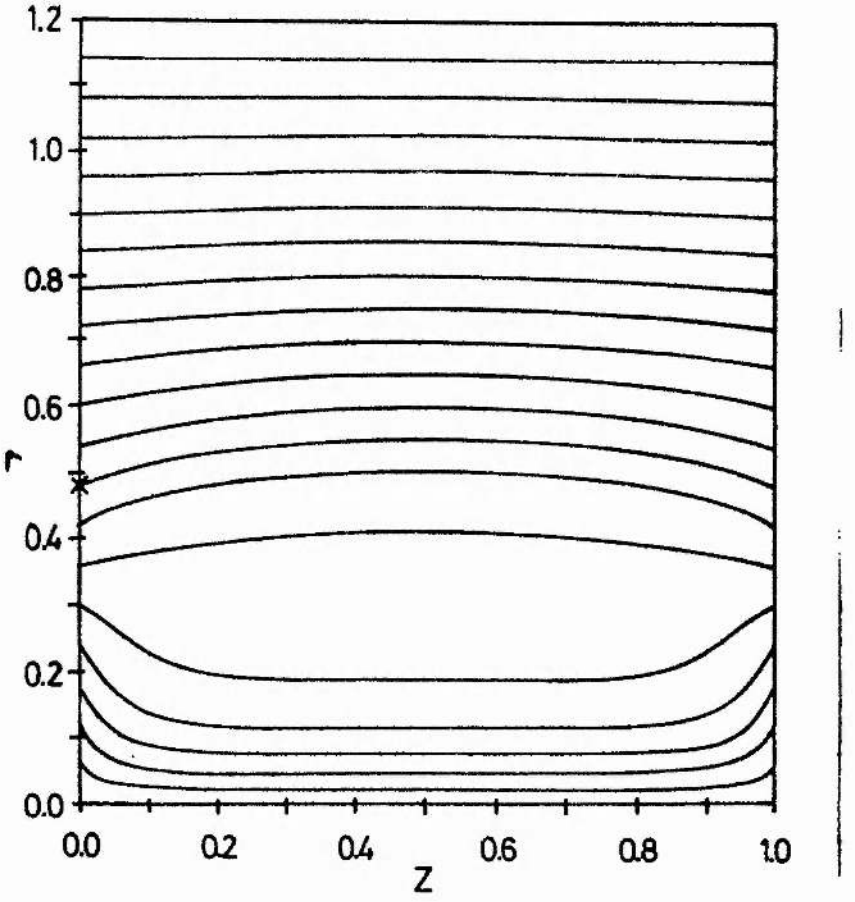

Figure 5.1 Flux surfaces for a twisted loop, obtained by Browning and Hood (1989).

large λ should drive B_z negative, causing a loss of equilibrium. If such a loss of equilibrium occurs at a radius small in comparison to the length of the tube, then we would not expect inclusion of the tension term (due to the radial field component) to restore equilibrium.

Consider the situation where the function K(A) is zero outside the radius r=1. If we normalise the untwisted initial field value at B_0=2, then A will be equal to unity at the edge of the twisted field region, which we shall refer to as the edge of the loop. When the loop has been twisted, the edge will have moved to a radius $r=r_e$, which may be identified as the radius at which A=1. Outside this radius, the field will maintain its initial value B_0, so the solution for A in $r>r_e$ is

$$A = 1 + r^2 - r_e^2 \tag{5.11}$$

In order to have magnetic pressure balance at the edge of the loop, we require the inner solution to satisfy

$$B_z^2(r_e) + B_\theta^2(r_e) = B_0^2 = 4 \tag{5.12}$$

In those cases where K(A) goes continuously to zero at A=1, this condition reduces to

$$B_z(r_e) = 2 \tag{5.13}$$

It is the ability to satisfy (5.12) which determines whether or not a solution exists. The method of solution chosen was to select a value of $B_z(0)$ and integrate out to A=1, using a Runge-Kutta-Merson method, thus obtaining a value for $B_z(r_e)$. $B_z(0)$ was then adjusted until $B_z(r_e)$ satisfied (5.12) or it became clear that no choice of $B_z(0)$ would achieve this. In order to compare with 2-D codes, the boundary condition

$$A(R) = R^2 \tag{5.14}$$

for some fixed radius R was applied on some runs. It was found that, provided R was large in comparison to r_e, there was little difference

between the two boundary conditions.

As an example, the profile

$$k(A) = A - A^2, \quad 0 \le A \le 1$$
$$= 0 \quad , \quad A > 1 \qquad (5.15)$$

was investigated. B_z and the change in radius δr of the flux surfaces from their untwisted positions for $\lambda = 9.5$ are shown as functions of radius in figures 5.2 and 5.3 respectively. Note, from figure 5.2, that the value of $B_z(0)$ has risen by a factor of 7, due to the pinching effect of the current. The corresponding inward displacement of the inner part of the field can be seen in figure 5.3, along with the expansion of the outer part. These movements combine to create a region of highly depleted axial field, which is visible in figure 5.2.

No solution was found for $\lambda > 9.7$. For this value of λ, the minimum of B_z had fallen to less than 10% of B_o. The outer flux surface of the loop had only expanded to a radius of 1.35. Hence, this approach would seem to show that twisting a loop results in non-equilibrium.

5.3 Twist on field line specified.

However, specification of K(A) is not very physical, since a finite K(A) may correspond to infinite footpoint motions. We would prefer to specify the total amount of twist on each field line, which is given by

$$\Phi(A) = \int_0^L \frac{B_\theta}{rB_z}\, dz \qquad (5.16)$$

where L is the loop length and the integration is taken along a single flux surface. However, if the loop is largely straight and, in addition, excessive amounts of twist are not absorbed by the boundary layers, this is approximately given by

$$\Phi = \frac{LB_\theta}{rB_z} \qquad (5.17)$$

where r is the radius of the central part of the tube. We may re-arrange (5.17), using (4.6), to obtain

$$K(A) = rB_\theta = r^2 B_z \frac{\Phi}{L} = r \frac{dA}{dr} \frac{\Phi}{L} \qquad (5.18)$$

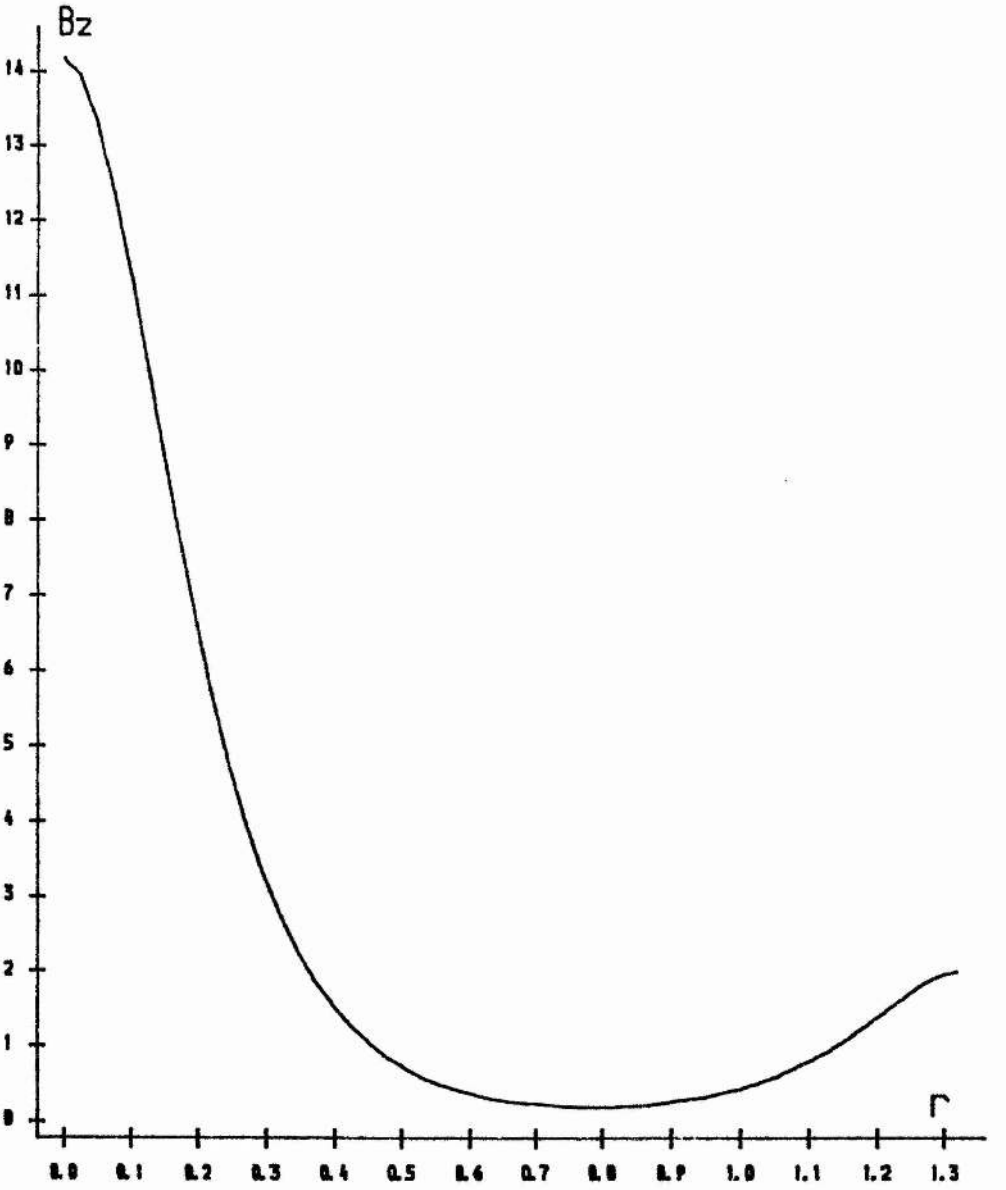

Figure 5.2. B_z for the twisted loop with K(A) specified.

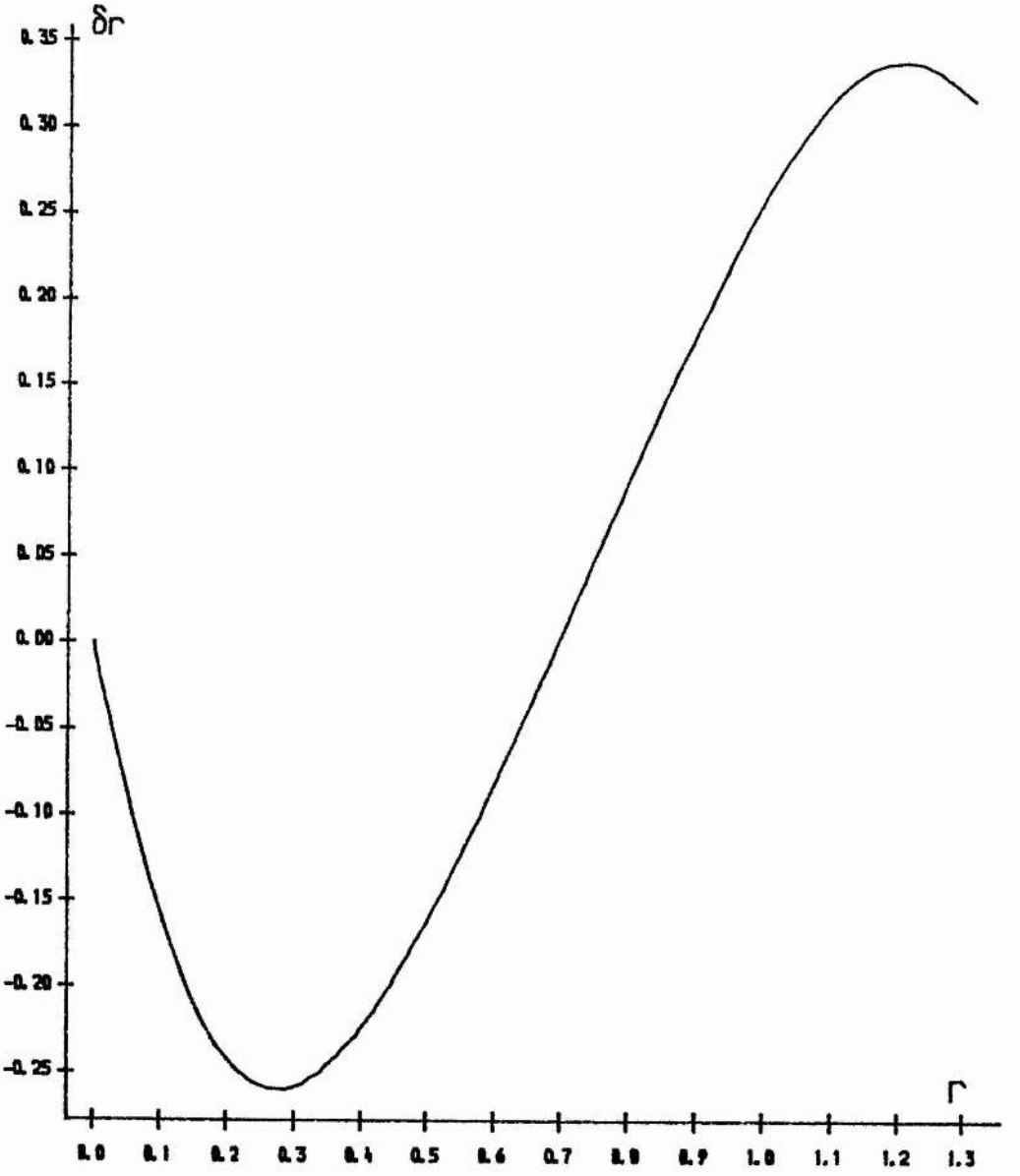

Figure 5.3. δr for the twisted loop with K(A) specified.

Following Browning and Hood, we substitute for K(A) in (5.8), to arrive at the 1-D equilibrium equation for a specified twist per unit length:

$$\left(1+\frac{r^2\Phi^2}{L^2}\right)\frac{d^2A}{dr^2}+\left(-\frac{1}{r}+\frac{d}{dr}\left[\frac{r^2\Phi^2}{2L^2}\right]\right)\frac{dA}{dr}=0 \qquad (5.19)$$

The 2-D nature is reflected in the dependence of Φ on the flux function.

Consider a field with a constant twist per unit length up to the radius A=1, i.e.

$$\frac{\Phi}{L}=\lambda \qquad A<1,$$
$$=0 \qquad A>1. \qquad (5.20)$$

Such a loop carries a non-zero current, unless there is a sheet of reverse current at the loop surface. The solution of (5.19) with the twist (5.20) is

$$A=\frac{\log\left(1+\lambda^2r^2\right)}{\log\left(1+\lambda^2r_e^2\right)} \qquad r<r_e,$$
$$=1+r^2-r_e^2 \qquad r\geq r_e \qquad (5.21)$$

where r_e is the radius of the loop, which must be determined by matching field strengths at the loop edge. With no current sheet, the matching condition at $r=r_e$ is simply continuity of B_z and we may show that there is always a solution and that the entire loop contracts as λ is increased. This is due to the pinch effect of the loop current. However, this corresponds to an azimuthal field which extends to infinity, which gives a twist falling off as r^{-2} rather than going directly to zero. Where there is a current sheet, there is no external B_θ and the external B_z must balance the combined internal fields. We may show that there is a solution and that, although the inner part of the field compresses, the outer part of the loop expands (except at very small λ, when there is a slight contraction of the outer field line).

We now wish to examine a twist which falls continuously to zero, in which case the loop carries no net current. The equivalent of the k-profile given by (5.15) is

$$\frac{\Phi}{L} = \lambda\,(1-A) \qquad (5.22)$$

For comparison with figures 5.2 and 5.3, figures 5.4 and 5.5 are their equivalents with $\Phi(A)$ specified. The figures are qualitatively similar, but there are some clear quantitative differences. In figure 5.4, the value of B_z on the axis is even higher than in 5.2. Nevertheless, the maximum and minimum values of δr are both lower for the present case and the edge of the loop has expanded less than in the case where K(A) was specified.

Solution of (5.19) for profile (5.22) showed no loss of equilibrium, even at very large values of λ. We conclude, therefore, that twist alone cannot cause non-equilibrium of a coronal loop. Solutions of (5.19) can be checked for correspondence to 2-D solutions by generating numerical values of K(A) and inserting them in equation (5.1), as outlined by Browning and Hood.

The twist of Steinolfson and Tajima corresponds to

$$\frac{\Phi}{L} = \lambda \qquad A < \frac{9}{16},$$

$$= 3\lambda\left(A^{-1/2} - 1\right) \qquad \frac{9}{16} < A < 1 \qquad (5.23)$$

This twist profile also showed no loss of equilibrium, suggesting that dynamic behaviour observed in their work was not due to loss of static equilibrium.

5.4 Effect of Enhanced Pressure.

Now consider the effect of creating an enhanced pressure P(A) within our loop. (5.19) becomes

$$\left(1 + \frac{r^2\Phi^2}{L^2}\right)\frac{d^2A}{dr^2} + \left(-\frac{1}{r} + \frac{d}{dr}\left[\frac{r^2\Phi^2}{2L^2}\right]\right)\frac{dA}{dr} = -r^2\,\frac{dP}{dA} \qquad (5.24)$$

For the untwisted loop, it is obvious that no equilibrium is possible if the pressure maximum exceeds the external magnetic pressure.

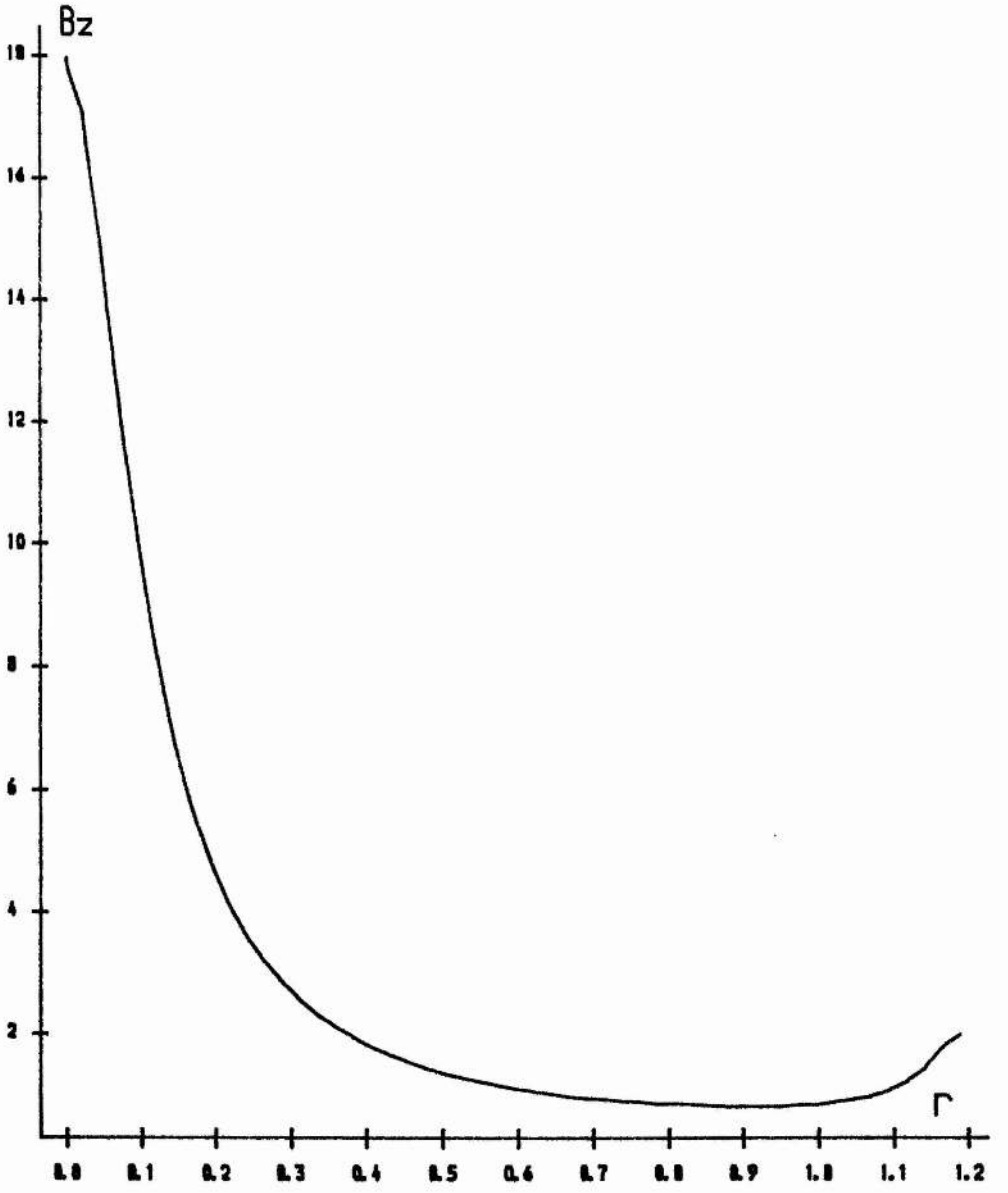

Figure 5.4. B_z for the twisted loop with $\Phi(A)$ specified.

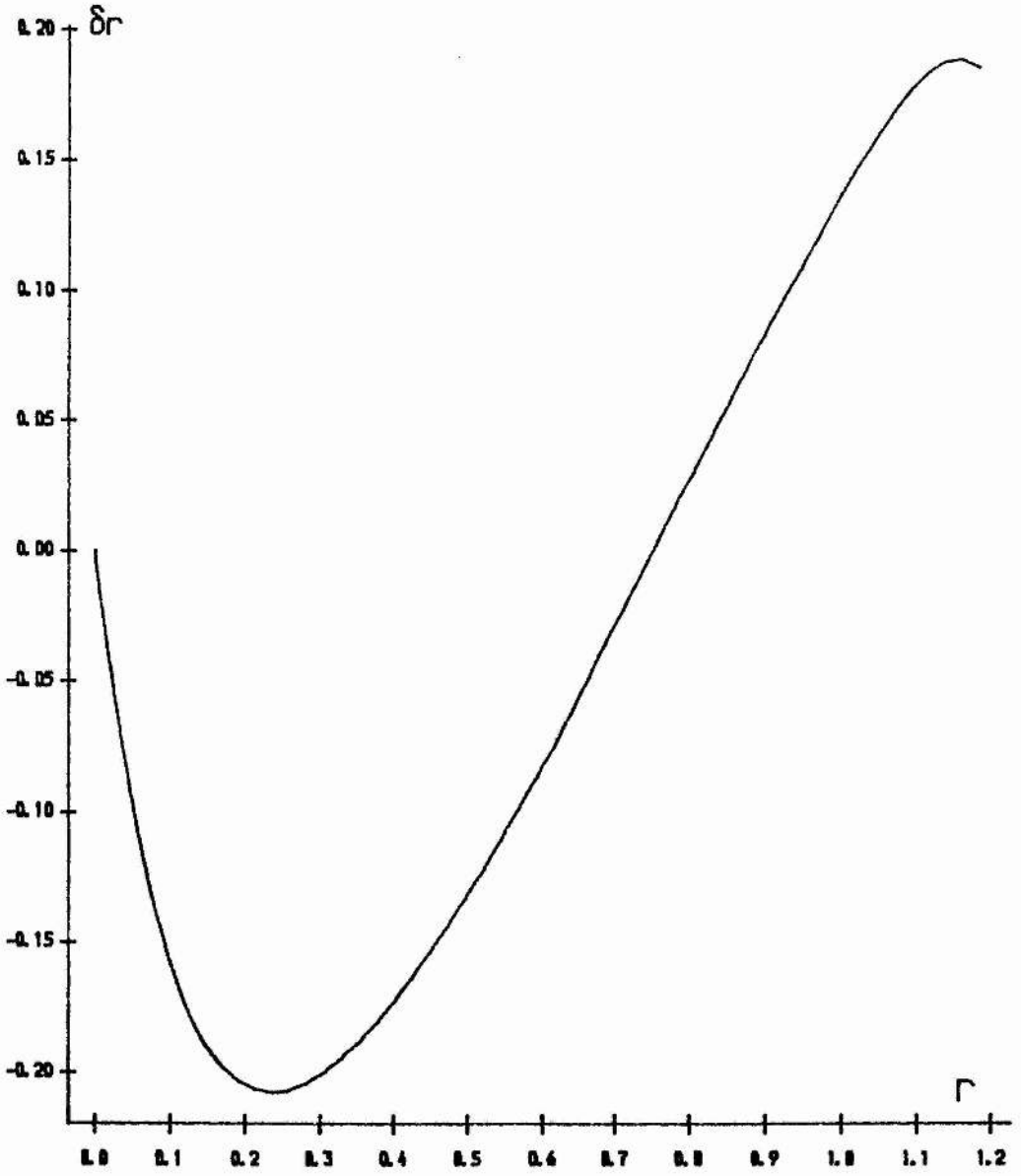

Figure 5.5. δr for the twisted loop with Φ(A) specified.

This is illustrated below.

We shall consider pressure profiles given by

$$P(A) = \begin{cases} \lambda_p p(A), & A < 1, \\ 0, & A > 1. \end{cases} \qquad (5.25)$$

for some specified p(A). We may obtain analytic solutions for some forms of p(A). Consider

$$p(A) = 1 - A \qquad (5.26)$$

for which the critical value of λ_p is clearly 2. (5.24) becomes

$$\frac{d^2A}{dr^2} - \frac{1}{r}\frac{dA}{dr} - \lambda_p r^2 = 0 \qquad (5.27)$$

which has solution

$$A = \frac{r^2}{r_e^2}\left(1 - \frac{\lambda_p}{8} r_e^4\right) + \frac{\lambda_p}{8} r^4 \qquad (5.28)$$

r_e is the radius of the edge of the tube, which is given by

$$r_e^2 = \frac{4}{\lambda_p}\left(1 - (1-\lambda_p/2)^{\frac{1}{2}}\right) \qquad (5.29)$$

The solution exists until $\lambda_p = 2$, at which point $r_e = \sqrt{2}$. Hence, the tube loses equilibrium when only slightly expanded and we do not expect tension to restore equilibrium.

We now compare the predictions of the 1-D model with a numerical solution to the 2-D equation:

$$r\frac{\partial}{\partial r}\left(\frac{1}{r}\frac{\partial A}{\partial r}\right) + \frac{\partial^2 A}{\partial z^2} = -r^2\frac{dp}{dA} \qquad (5.30)$$

Since a numerical solution is required, boundary conditions on A are applied at a finite radius, say r_{edge}=b. Then the effect of varying b can be studied. The boundary conditions chosen were

$$A(r,0) = A(r,L) = r^2 \;;\; A(0,z) = 0 \;;\; A(b,z) = b^2 \qquad (5.31)$$

The linear operator on the LHS of (5.30) was replaced by the corresponding difference operator (which we shall denote M) on a grid of A values. It was then possible to solve (5.30) using the simple iterative scheme

$$M\,\delta A = -\varepsilon\left(r^2\frac{dp}{dA^i} + MA^i\right) \;;\; A^{i+1} = A^i + \delta A \qquad (5.32)$$

with the iteration stopping when the norm of the RHS and the norm of δA are both sufficiently small (typically 10^{-5} and 10^{-3} respectively). Here the norm is taken as

$$\| \delta A \| = \sum_i \sum_j | \delta A_{ij} | \qquad (5.33)$$

ε was chosen to ensure convergence.

The conclusions about loss of equilibrium depend on the value of the outer radius b. For the pressure profile given by (5.25) and (5.26), no loss of equilibrium was found for b=2 (i.e. twice the radius of the tube). Results for $\lambda_p=2$ are shown in figures 5.6-5.10. In this example, the aspect ratio of the loop was chosen to be 8. Even at $\lambda_p=2$, the value of B_z on the axis has only fallen to 1, half its original value. In contrast to the infinite radius results obtained above, the total pressure increases, since the field is no longer free to expand and B_z does not drop as rapidly as the gas pressure increases. This result, as shown below, does not depend on the length of the loop. Figure 5.6 shows the field lines, which exhibit an expansion everywhere. However, the indication is that the 1-D model is still appropriate for this loop.

The typical boundary layer behaviour is clearly seen from the contours of B_z in figure 5.7. B_z is reduced at r=0, but remains approximately 2 outside the loop. A section through z=L/2 (figure 5.8) shows B_z as a function of radius for comparison with the 1-D model. For b=2, with $A=b^2$ at r=b, the 1-D solution becomes

$$A = \begin{cases} \left(\dfrac{b^2-1}{b^2-r_e^2} - \dfrac{\lambda_p}{4} r_e^2 \right) r^2 + \dfrac{\lambda_p}{8} r^4, & 0 \le r \le r_e, \\ b^2 + \dfrac{b^2-1}{b^2-r_e^2} (r^2-b^2), & r_e \le r \le b. \end{cases} \qquad (5.34)$$

where r_e satisfies

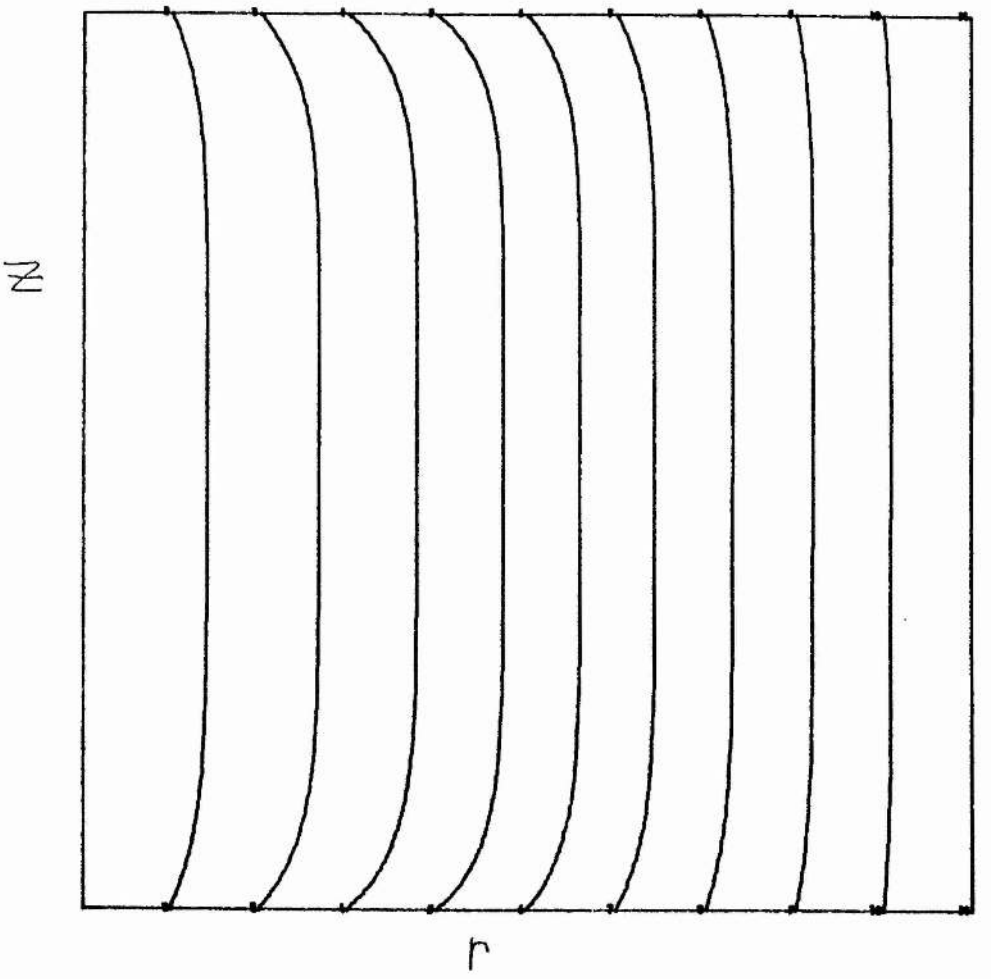

Figure 5.6. Field lines for loop with enhanced pressure:

$\lambda_p = 2$, $b = 2$.

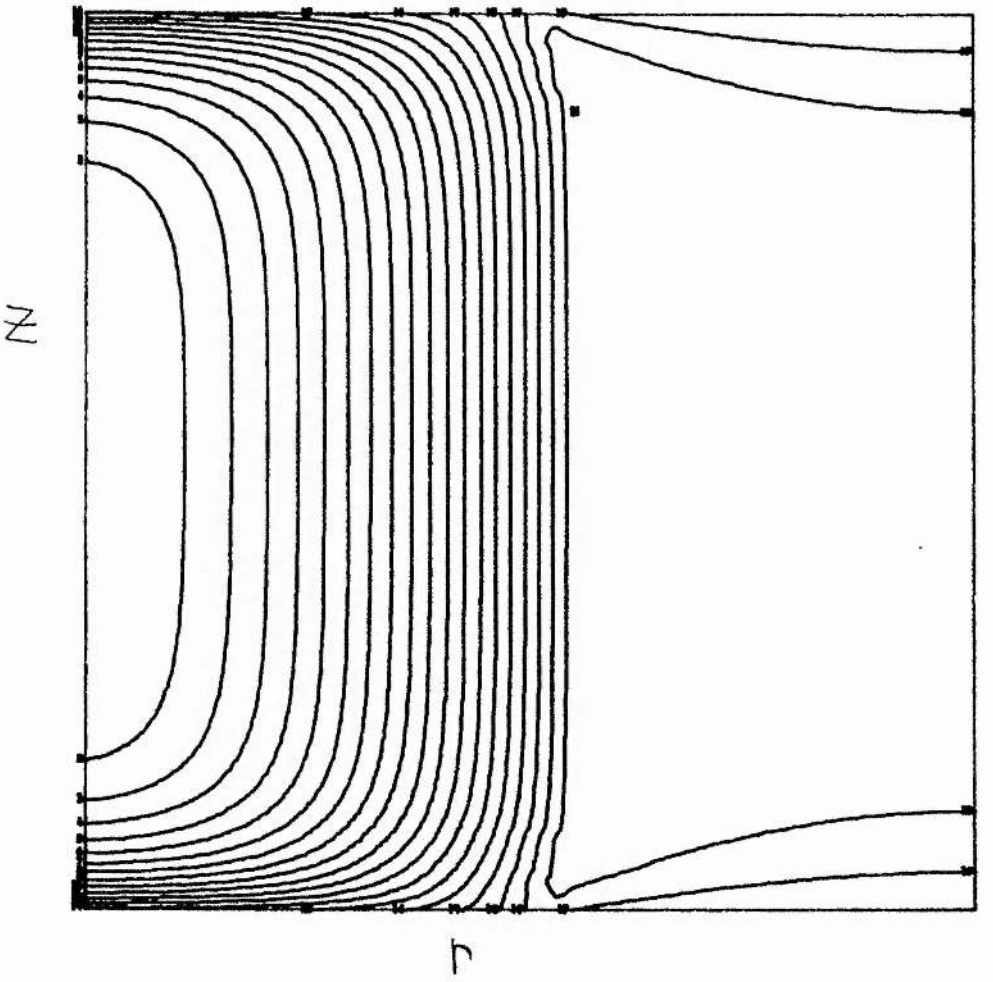

Figure 5.7. Contours of B_z for loop with enhanced pressure:

$\lambda_p = 2$, $b = 2$.

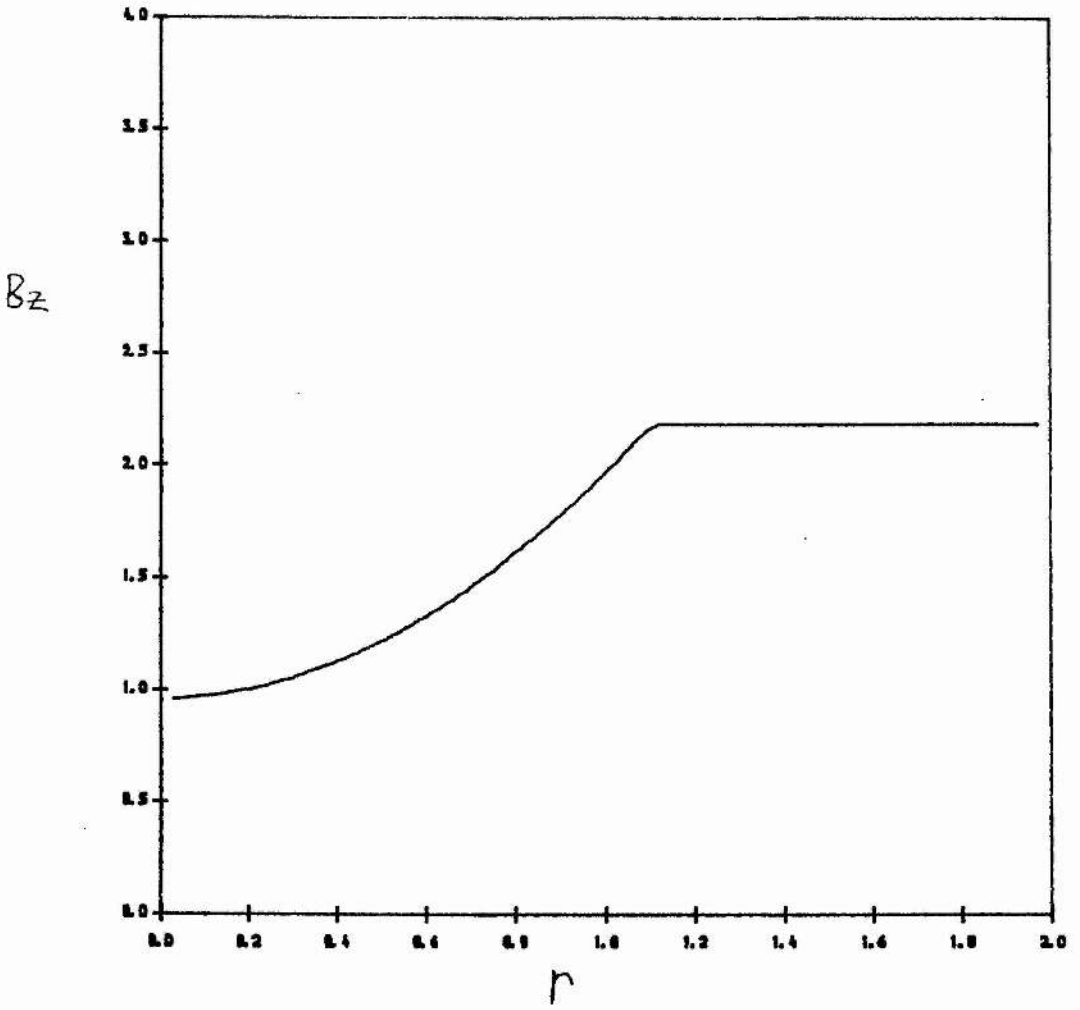

Figure 5.8. $B_z(r,L/2)$ for loop with enhanced pressure:

$\lambda_p = 2$, $b = 2$.

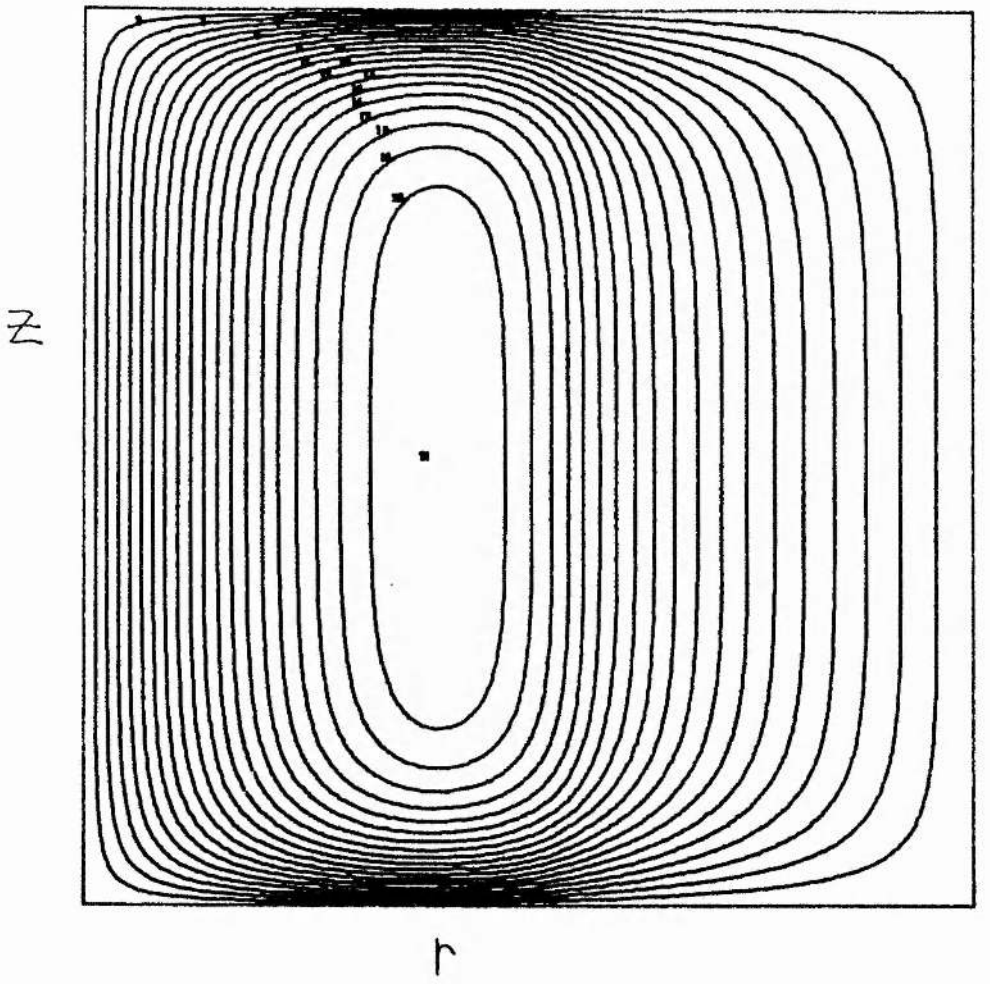

Figure 5.9. Contours of δr for loop with enhanced pressure:

$\lambda_p = 2$, $b = 2$.

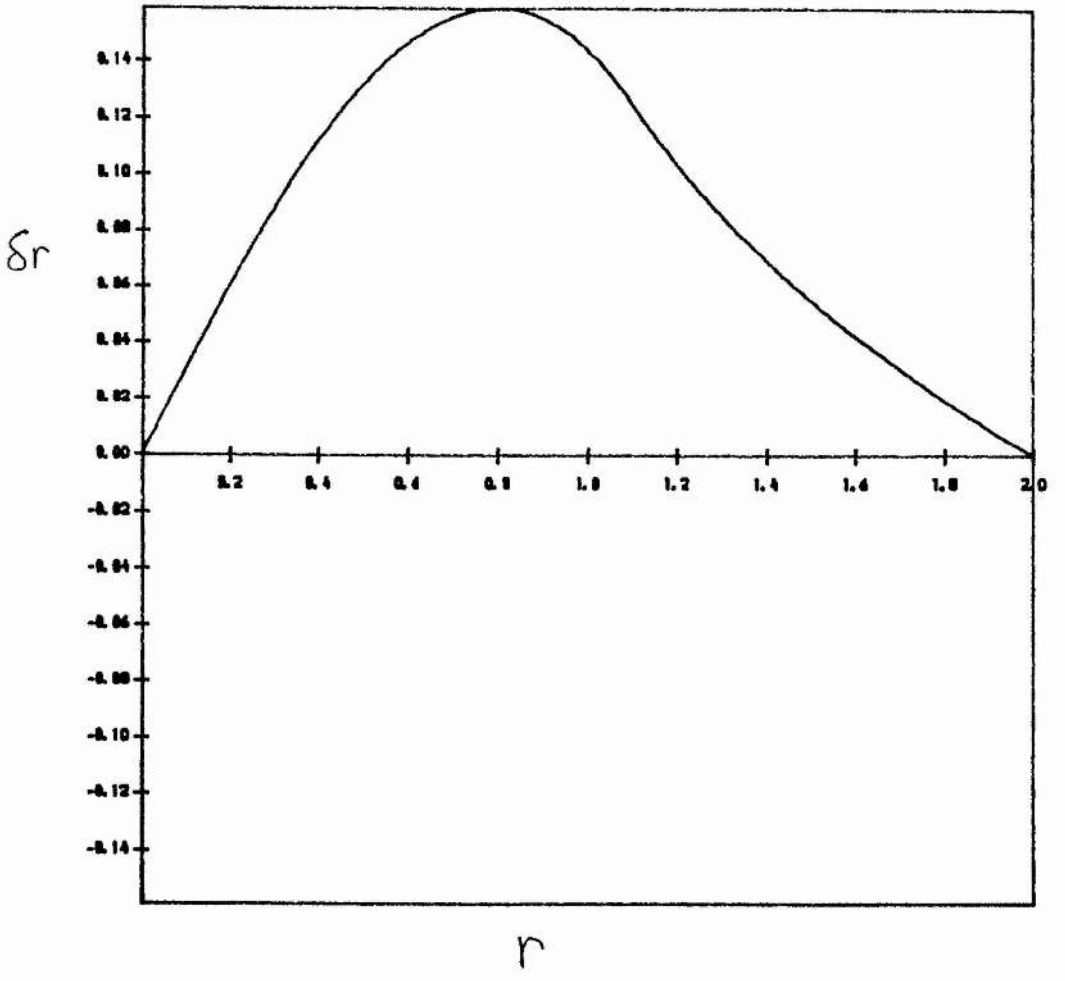

Figure 5.10. δr(r,L/2) for loop with enhanced pressure:

$\lambda_p = 2$, $b = 2$.

$$\frac{\lambda_p}{8} r_e^4 = b^2 \frac{r_e^2-1}{b^2-r_e^2} \tag{5.35}$$

Solving (5.35) with $\lambda_p=2$ gives $r_e^2 \approx 1.28$ and $B_z(0) \approx 0.93$ in good agreement with the 2-D results of figure 5.8.

Figure 5.9 shows the contours of δr, the change in radius, with the section through z=L/2 shown in figure 5.10. The existence of a non-equilibrium point can be deduced from (5.35). At such a point $d\lambda_p/dr_e=0$. Hence,

$$2 r_e^4 - (3+b^2) r_e^2 + 2b^2 = 0 \tag{5.36}$$

Thus,

$$r_e^2 = \frac{3+b^2}{4} \pm \frac{1}{4} \sqrt{9 - 10b^2 + b^4} \tag{5.37}$$

There are real solutions, and hence a point of non-equilibrium, if b>3. To illustrate this, the 2-D code was run with b=4 and L=8 and 65 points in each direction. The critical value of λ_p is approximately 2.3 and $r_e^2=2.19$. The results for λ_p =2.5 are shown in figures 5.11.-5.15. Notice how much more the field lines are bent in figure 5.11 and that B_z has dropped almost to zero in figures 5.12 and 5.13. No solutions were found for $\lambda_p=3$. The fact that the critical value is larger than that predicted from the 1-D theory is not too surprising, since tension effects will help to contain the higher pressure.

Thus, we have illustrated how important the position of the boundary is for determining whether non-equilibrium occurs or not. The wrong conclusion is reached if the outer radial boundary is too close to the edge of the loop. Once far enough away, this outer condition does not strongly influence the conclusions and the difference between the possible boundary conditions becomes small.

The pressure

$$p(A) = 1 - A^2 \tag{5.38}$$

falls off more slowly than the previous example. (5.24) becomes

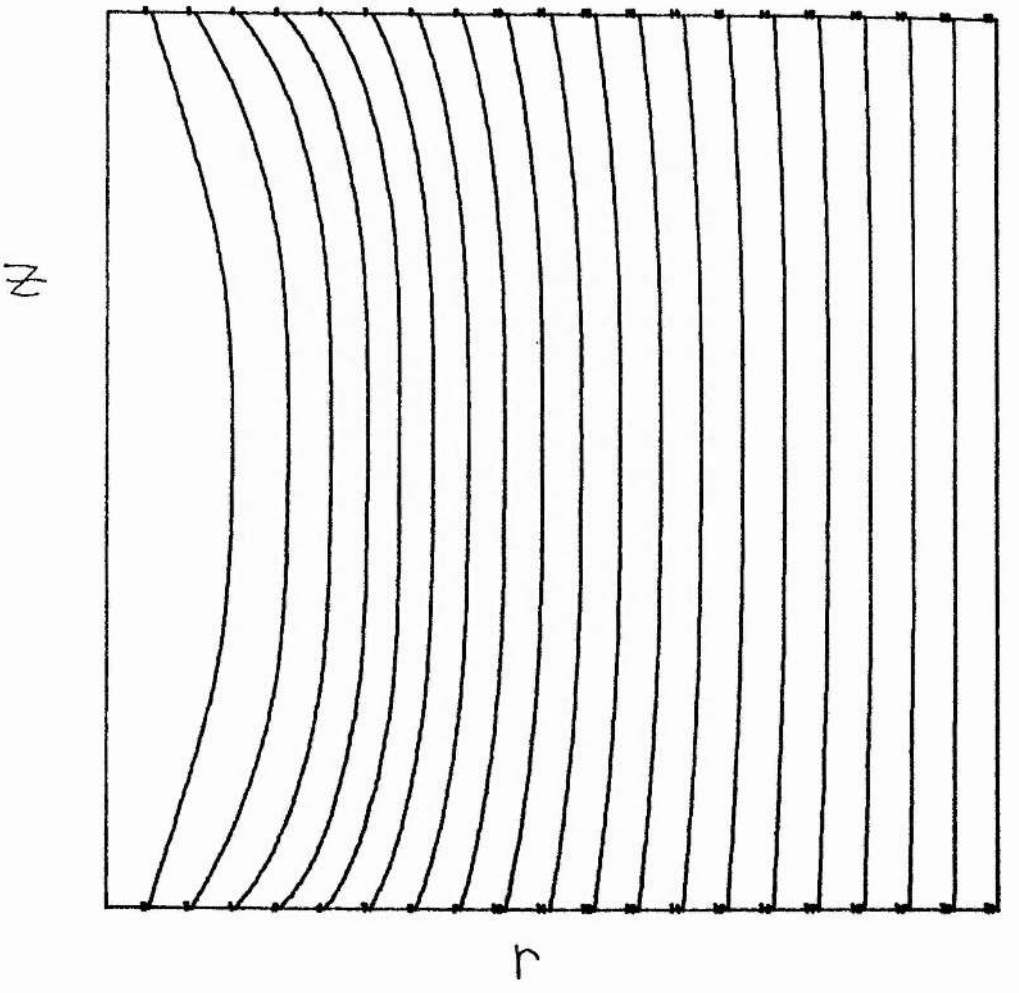

Figure 5.11. Field lines for loop with enhanced pressure:

$\lambda_p = 2.5$, $b = 4$.

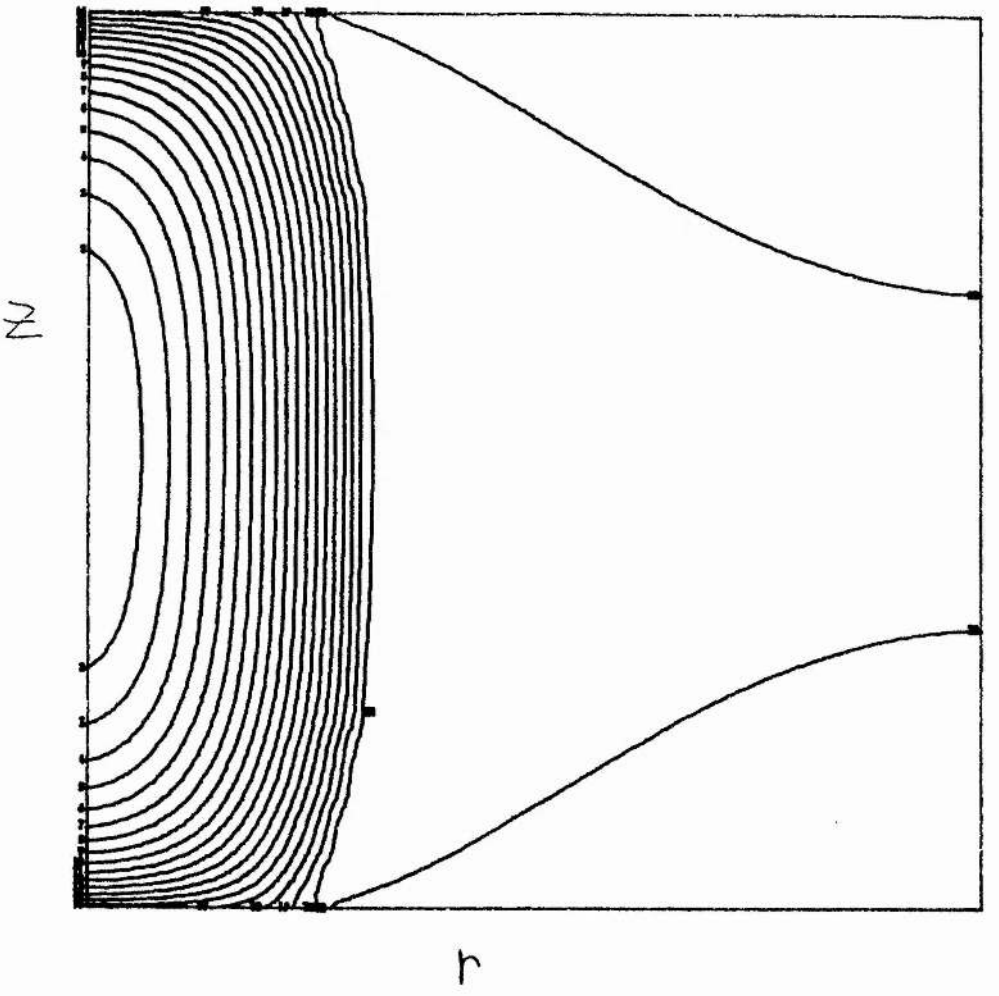

Figure 5.12. Contours of B_z for loop with enhanced pressure:

$\lambda_p = 2.5$, $b = 4$.

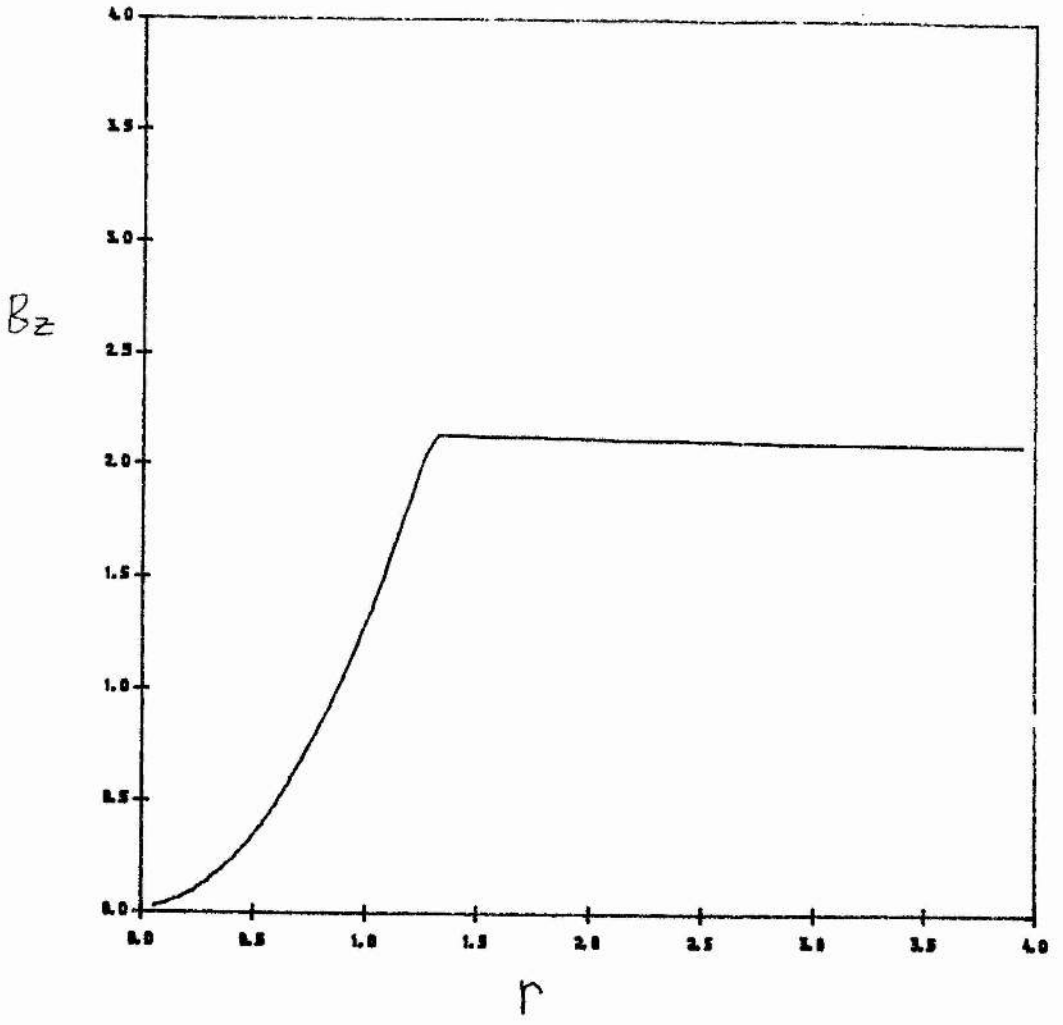

Figure 5.13. $B_z(r,L/2)$ for loop with enhanced pressure:

$\lambda_p = 2.5$, $b = 4$.

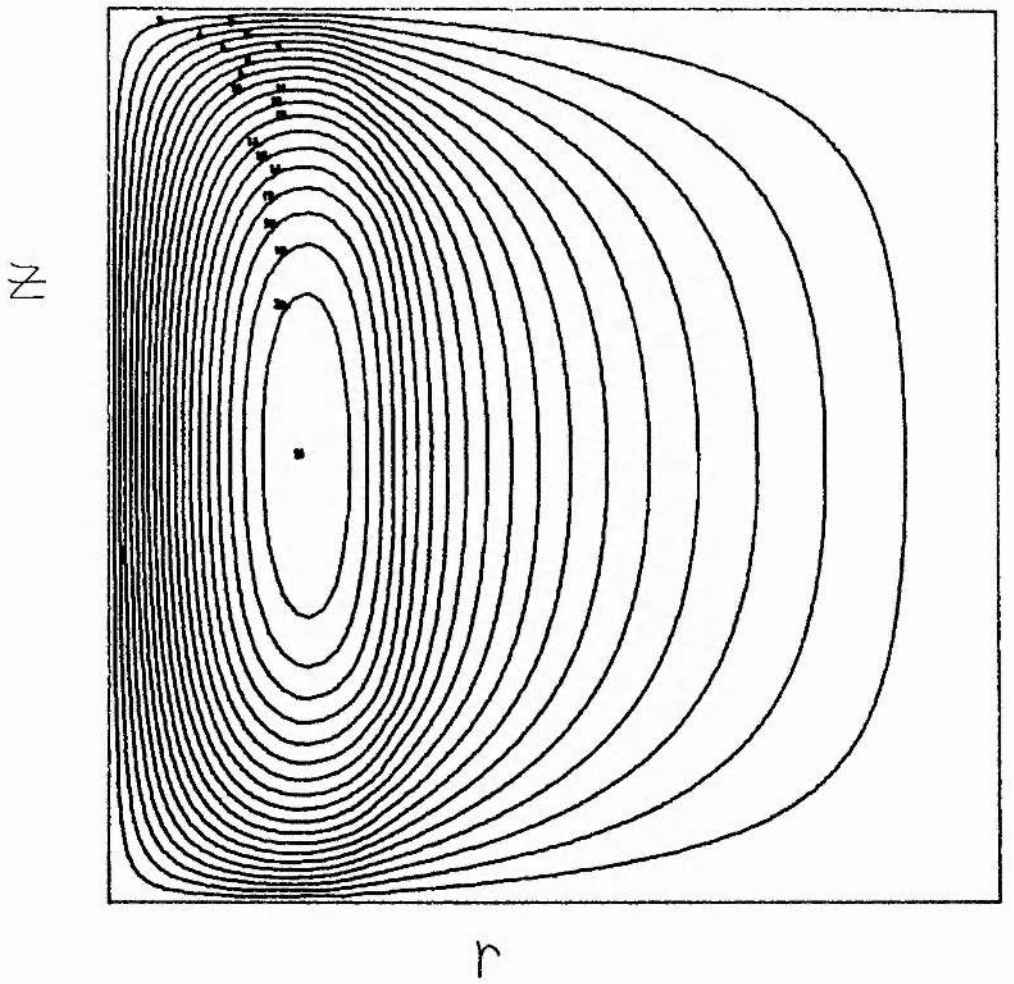

Figure 5.14. Contours of δr for loop with enhanced pressure:

$\lambda_p = 2.5$, $b = 4$.

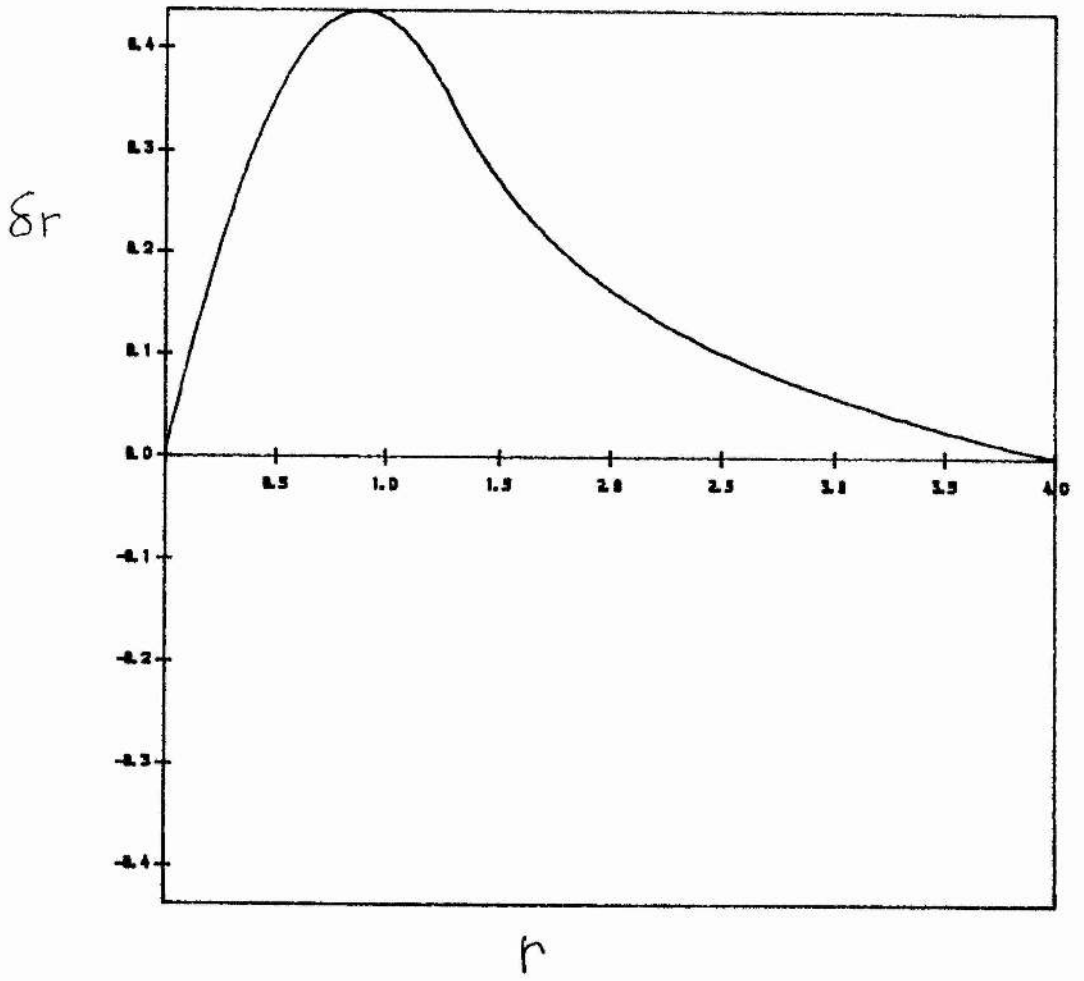

Figure 5.15. δr(r,L/2) for loop with enhanced pressure:

$\lambda_p = 2.5$, b = 4.

$$\frac{d^2A}{dr^2} - \frac{1}{r}\frac{dA}{dr} - 2\lambda_p r^2 A = 0 \qquad (5.39)$$

with solution

$$A = \frac{\sinh\left[\sqrt{(\lambda_p/2)}\, r^2\right]}{\sinh\left[\sqrt{(\lambda_p/2)}\, r_e^2\right]} \qquad (5.40)$$

where

$$r_e^2 = \left(\frac{2}{\lambda_p}\right)^{\frac{1}{2}} \tanh^{-1}\left(\frac{\lambda_p}{2}\right)^{\frac{1}{2}} \qquad (5.41)$$

Again, equilibrium is only lost when the pressure maximum becomes equal to the ambient magnetic pressure. Since r_e becomes infinite as λ_p tends to 2, the loss of equilibrium is less conclusive in this case. However, r_e remains small quite close to λ_p=2, e.g. r_e = 1.83 at λ_p=1.99. The profile

$$p(A) = A - A^2 \qquad (5.42)$$

has a maximum off-axis, which we consider unphysical; nevertheless, it is interesting to solve the problem. (5.24) becomes

$$\frac{d^2A}{dr^2} - \frac{1}{r}\frac{dA}{dr} + \lambda_p r^2 (1 - 2A) = 0 \qquad (5.43)$$

which has solution

$$A = \frac{1}{2}\left(1 - \cosh\left[\sqrt{(\lambda_p/2)}\, r^2\right]\right) + \frac{1 + \cosh\left[\sqrt{(\lambda_p/2)}\, r_e^2\right]}{2\sinh\left[\sqrt{(\lambda_p/2)}\, r_e^2\right]} \sinh\left[\sqrt{(\lambda_p/2)}\, r^2\right] \qquad (5.44)$$

r_e is the solution of

$$\frac{1 + \cosh\left[\sqrt{(\lambda_p/2)}\, r_e^2\right]}{2\sinh\left[\sqrt{(\lambda_p/2)}\, r_e^2\right]} = \sqrt{(2/\lambda_p)} \qquad (5.45)$$

and tends to infinity as λ_p tends to 8. This case behaves similarly to the previous case. We observe that, in all cases, equilibrium is obtained if the pressure maximum is less than the ambient magnetic

pressure. Hence, at least in the untwisted case, we do not expect pressure to drive coronal loops (which have a low β) out of equilibrium. We shall now consider the twisted loop with pressure.

5.5 The Twisted Loop with Pressure.

To the twist given by (5.22), a pressure given by (5.26) was added. It was found that small amounts of extra pressure could be contained by highly twisted loops. Figures 5.16 and 5.17 show δr and B_z for the case λ=2.2, λ_p=2.5. The large value of pressure has resulted in B_z being reduced at all radii. However, the field is still most depleted in a region away from both the axis and the edge. At smaller values of pressure, the pinch effect dominates and causes an increased value of $B_z(0)$.

Again we conclude that for coronal loops, small pressure fluctuations will not cause loss of equilibrium. It is interesting for other applications, to examine the loss of equilibrium at high pressures. Figure 5.18 shows the regions of equilibrium and non-equilibrium in the λ-λ_p plane. A second solution, which we do not consider physically relevant, appears when the pressure is nearly large enough to cause non-equilibrium. To illustrate how equilibrium is lost and the second solution appears, consider the method of solving (5.24). We begin with an estimated value for $B_z(0)$ and integrate out to A=1 (the edge of the loop). We then adjust $B_z(0)$ until $B_z(A=1)$ is 2. Figure 5.19 shows $B_z(A=1)$ as a function of $B_z(0)$ for several values of λ_p and a fixed value (λ=5) of the twist. In the zero pressure case, $B_z(A=1)$ simply rises monotonically from zero to 2 and beyond as $B_z(0)$ is increased. For finite pressure (λ_p=1,2), $B_z(0)$ begins from a non-zero value, drops slightly, then rises to 2 and beyond. When the value of $B_z(A=1)$ corresponding to $B_z(0)$=0 rises beyond 2 (e.g. λ_p=3), a second solution appears with a much lower

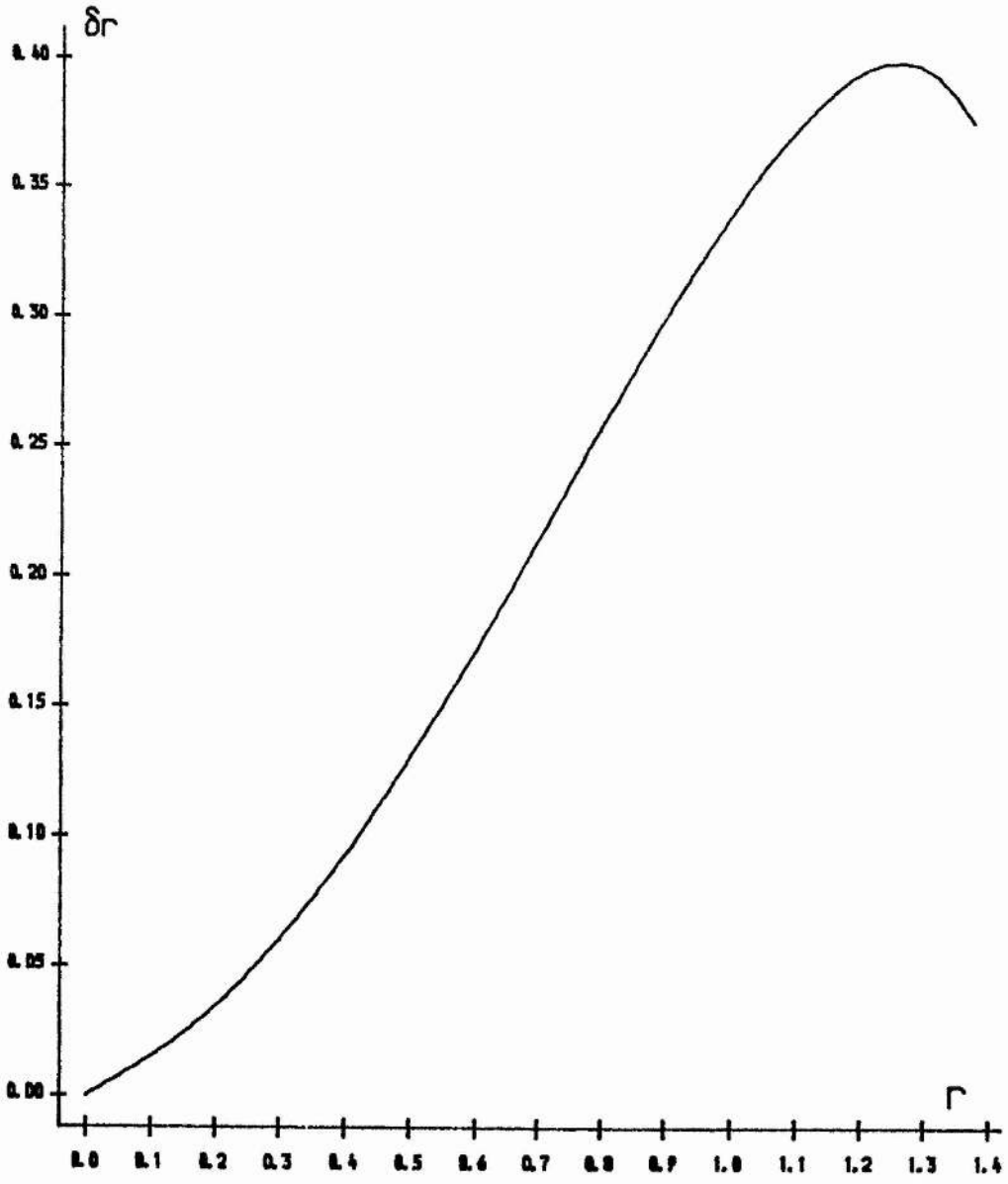

Figure 5.16. δr for the twisted loop with pressure:

λ =2.2, λ_p=2.5.

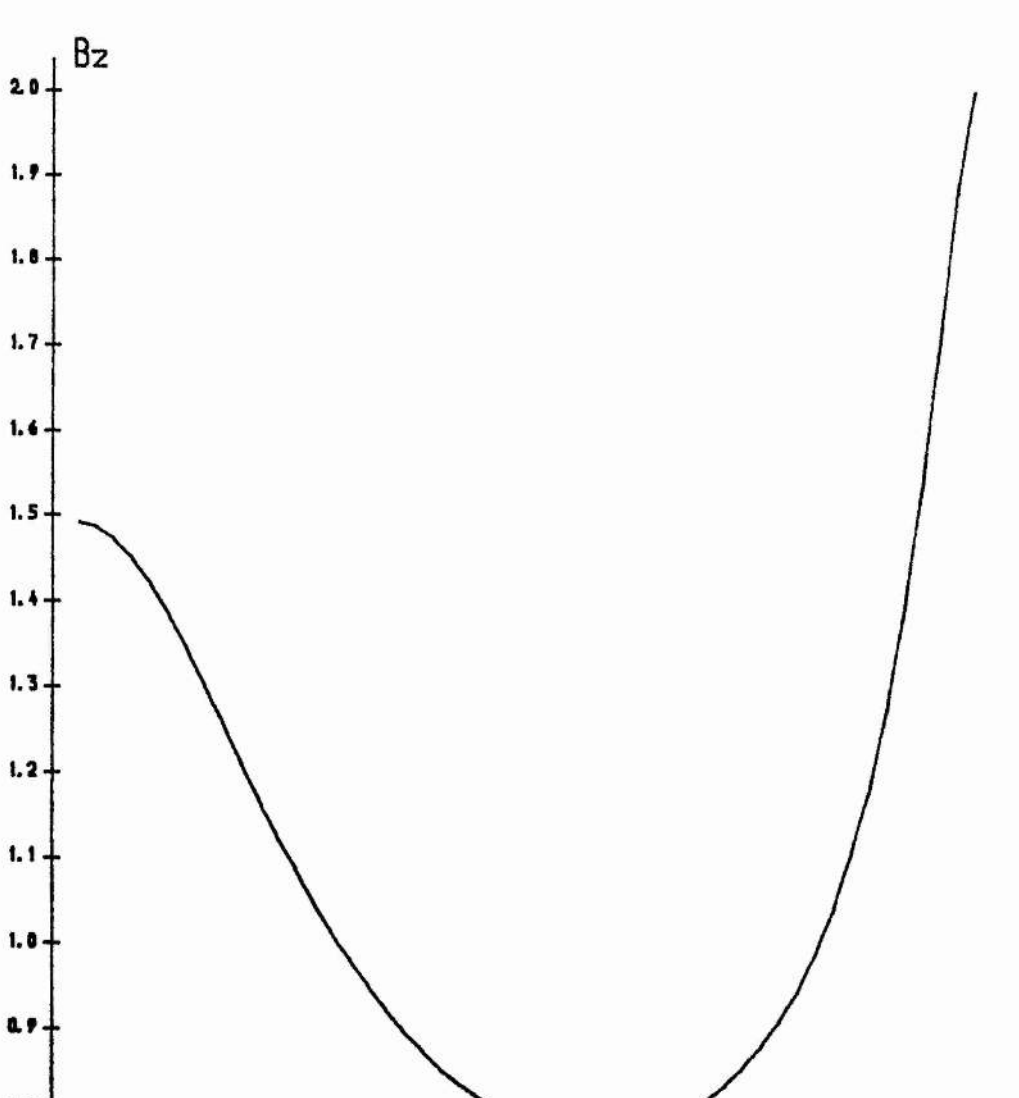

Figure 5.17. B_z for the twisted loop with pressure:

λ =2.2, λ_p=2.5.

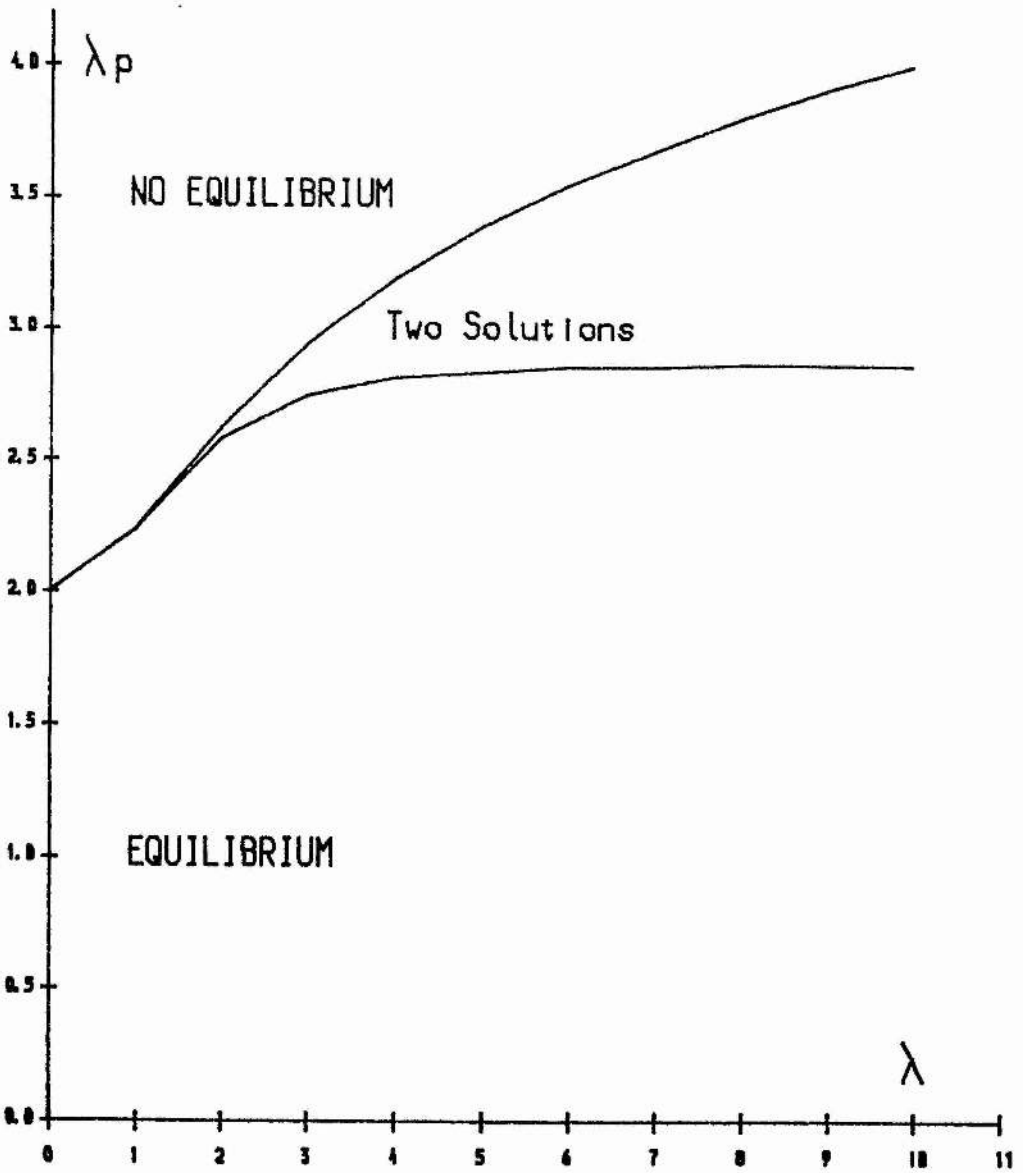

Figure 5.18. Regions of equilibrium and non-equilibrium

in the λ-λ_p plane.

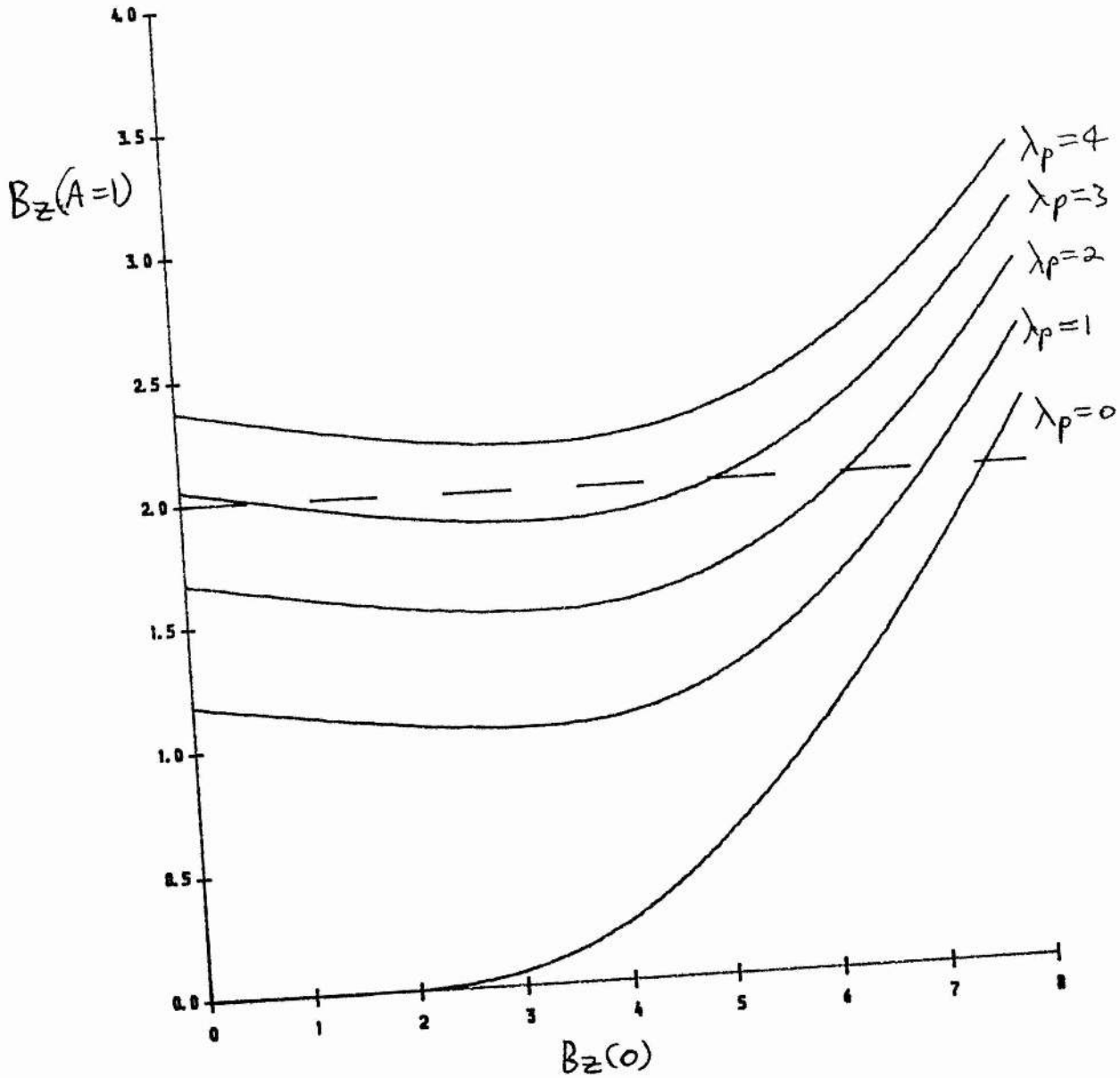

Figure 5.19. $B_z(A=1)$ as a function of $B_z(0)$ for $\lambda = 5$ and $\lambda_p = 0,1,2,3,4$.

value of $B_z(0)$. This solution represents a much more expanded tube than the first solution. At still higher values (λ_p=4) of the pressure, the curve is entirely above $B_z(A=1)=2$ and so there is no solution and, hence, no equilibrium.

5.6 Adiabatic Processes.

Instead of specifying the pressure as a function of A, we may require the entropy to be conserved. If plasma motions are adiabatic, then entropy is conserved in ideal MHD. This is appropriate when plasma motions are sufficiently fast to make heat transfer negligible. Although we have previously stipulated that motions shall be quasi-statically slow, it is nevertheless important to examine the adiabatic limit. Following Finn and Chen (1989), we shall consider the quantity PV^γ, which is constant for an adiabatic process. V is the volume of the plasma and γ is the ratio of specific heats, which we shall take to be 5/3, the value for an ideal monatomic gas. For a volume of plasma contained between two neighbouring flux surfaces enclosing flux A and A+dA, we have

$$PV^\gamma = P(A)\left(\frac{dV}{dA}dA\right)^\gamma \tag{5.46}$$

Where V(A) is the volume enclosed by the flux surface of value A and the photosphere. Since plasma cannot cross the flux surfaces, dA is constant and

$$P(A)\left(\frac{dV}{dA}\right)^\gamma = \text{a constant} \tag{5.47}$$

for an adiabatic process.

V(A) has the form

$$V(A) = 2\pi\int_0^L\int_0^{r(A)} r\,dr\,dz = 2\pi\int_0^L\int_0^A \frac{r}{\partial A/\partial r}\,dA\,dz = 2\pi\int_0^A\int_0^L \frac{dz}{B_z}\,dA \tag{5.48}$$

where the z-integral is taken at constant A. Hence, it is clear that

$$\frac{dV}{dA} = 2\pi\int_0^L \frac{dz}{B_z} \tag{5.49}$$

Note the numerical factor 2π, which Finn and Chen do not obtain; this

factor arises from the difference between arcade and cylindrical geometries.

We shall refer to the quantity S(A) given by

$$S(A) = P(A) \left[\int_0^L \frac{dz}{B_z} \right]^{\gamma} \tag{5.50}$$

which we have demonstrated to be conserved in adiabatic processes, as the pseudo-entropy. In the 1-D case, (5.50) reduces to

$$S(A) = P(A) \frac{L^{\gamma}}{B_z^{\gamma}} \tag{5.51}$$

The equivalent of (5.24) may easily be found as

$$\left[1 + \frac{r^2\Phi^2}{L^2} + \frac{\gamma S}{L^{\gamma}} \left(\frac{1}{r} \frac{dA}{dr} \right)^{\gamma-2} \right] \frac{d^2A}{dr^2} + \left[-\frac{1}{r} + \frac{r^2\Phi}{L^2} \frac{d\Phi}{dr} \right] \frac{dA}{dr}$$

$$- \frac{\gamma S}{L^{\gamma}} \left(\frac{1}{r} \frac{dA}{dr} \right)^{\gamma-1} + \frac{dS}{dA} \frac{r^2}{L^{\gamma}} \left(\frac{1}{r} \frac{dA}{dr} \right)^{\gamma} = 0 \tag{5.52}$$

We can see that, even where the initial equilibrium has no pressure gradients, the result of twisting is modified by the terms in S(A). Hence, a uniform non-zero coronal beta has an effect on adiabatic motions. If we re-arrange (5.52) to obtain the expression

$$\frac{dB_z}{dr} = - \frac{2\Phi^2 r B_z + r^3 \Phi \frac{d\Phi}{dA} B_z^2 + \frac{dS}{dA} r \frac{B_z^{\gamma}}{L^{\gamma}}}{1 + r^2\Phi^2 + \gamma S L^{-\gamma} B_z^{\gamma-2}} \tag{5.53}$$

we can see that this effect is likely to lessen any movement caused by twist. This is consistent with the fact that any expansion creates pressure gradients which act against the expanding forces. To see this effect, we compare the results for the twist profile (5.22) with zero beta and a constant pseudo-entropy corresponding to an initial beta of 0.079. We see, from figures 5.20 and 5.21, that both the value of B_z on the magnetic axis and the expansion of the tube are reduced by the effect of finite beta.

We also wish to examine the response of a tube to an enhanced base pressure, but keeping the pseudo-entropy fixed as a function of

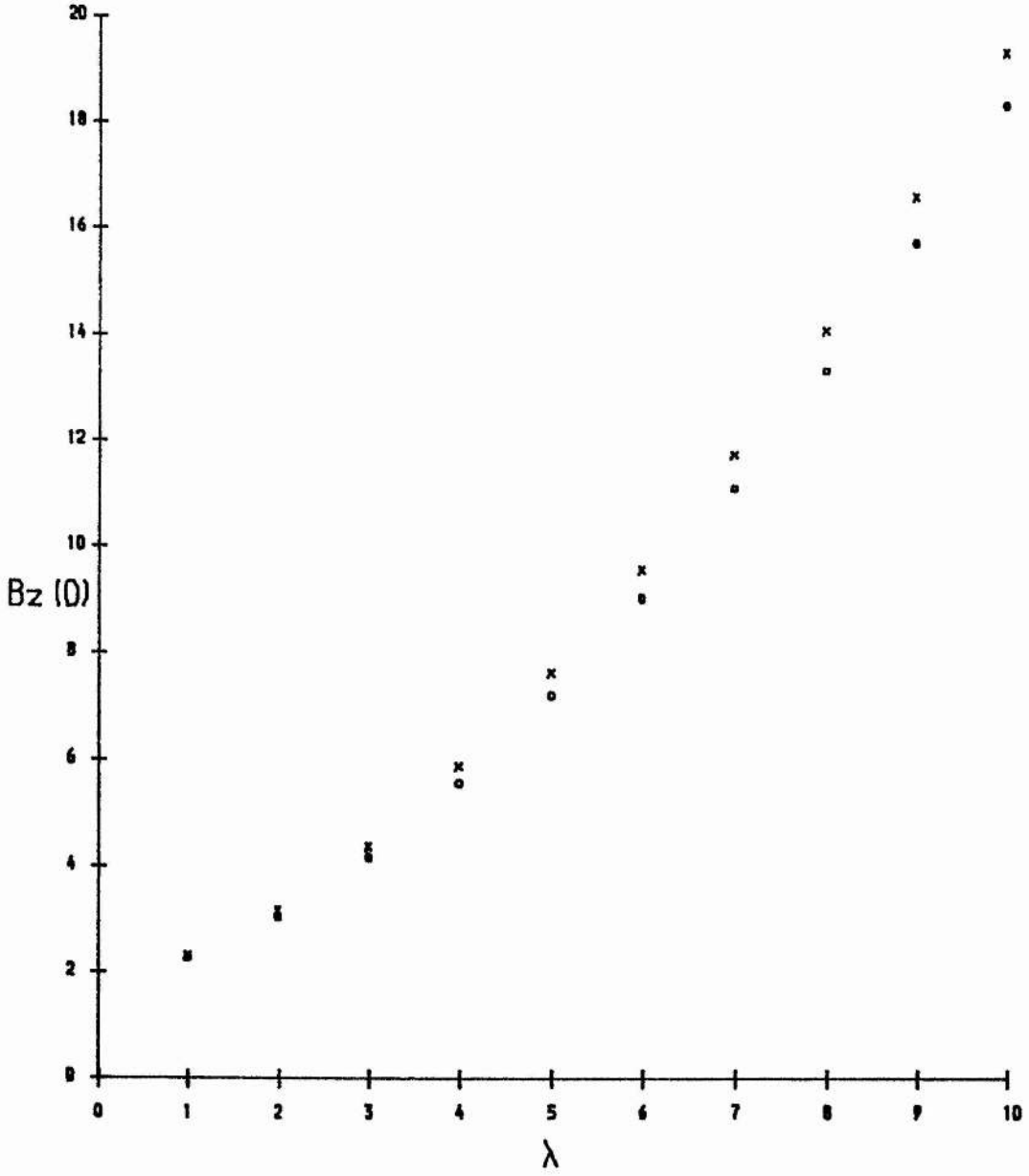

Figure 5.20. $B_z(0)$ as a function of λ for $\beta = 0$ (x)

and $\beta = 0.079$ (o).

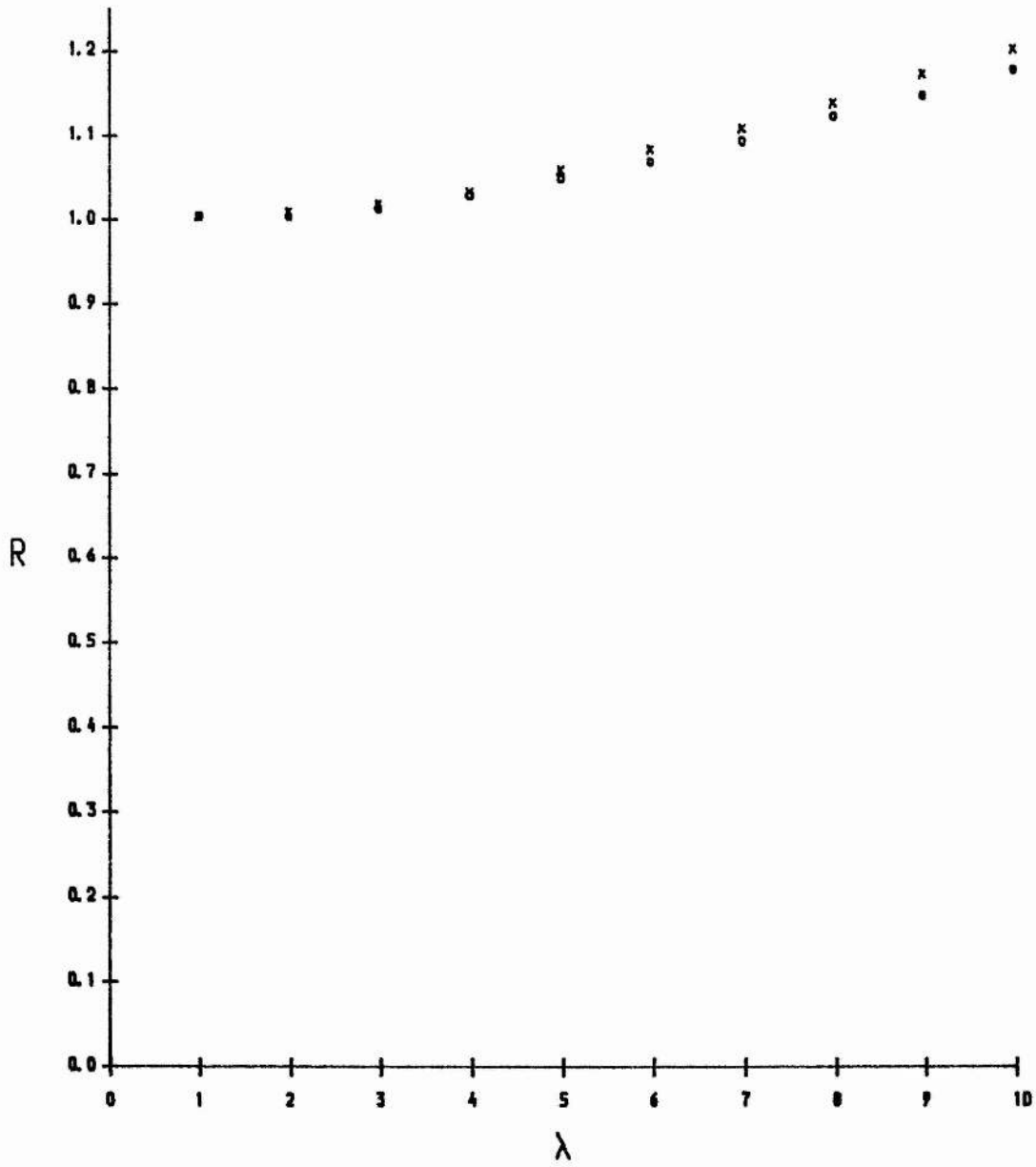

Figure 5.21. Radius of the flux tube as a function of λ

for $\beta = 0$ (x) and $\beta = 0.079$ (o).

A, rather than the pressure. We chose the following form for S(A):

$$\frac{S(A)}{L^{\gamma}} = 2^{-\gamma}\lambda_s (1-A), \quad A < 1,$$

$$= 0, \qquad A \geq 1. \tag{5.54}$$

The reason for the factor $2^{-\gamma}$ was to make the parameter λ_s equal to the equivalent parameter λ_p in (5.25), since the form of the pseudo-entropy corresponds to the initial pressure distribution (5.26). At very low values of λ_s, the results were similar to those with pressure specified. However, at higher values of λ_s, the effects were reduced. In particular, there was no loss of equilibrium at λ_s = 2. In fact, no loss of equilibrium was found below λ_s =10. The addition of twist as well as a specified pseudo-entropy resulted in similar effects to the case of twist and specified pressure, but with the loss of equilibrium at higher parameter values.

This form of the 1-D model allows us to make a comparison with the work of Mikic et al. (1990), in which the 3-D dynamical evolution of a twisted flux tube was studied. They confirmed that a twisted tube evolves through a series of equilibria and found that the tube eventually becomes unstable to an ideal kink mode. They studied a tube of aspect ratio 4, with a fixed radial boundary at 4 times the radius of the tube. In our 1-D analysis, we found negligible difference between this boundary condition and (5.13).

The applied photospheric velocity generated a twist given by

$$\frac{\Phi}{L} = \lambda (1-A)^2, \qquad A < 1 \tag{5.55}$$

and a uniform initial beta of 0.1 was assumed. Mikic et al. showed results for an equilibrium where the twist on the magnetic axis was 5π, just above the kink instability threshhold of 4.8π. Inserting this twist in (5.52), we obtained the plot of B_z shown in figure 5.22. This is almost identical to the plot given by Mikic et al. of B_z at the mid-plane of the loop. The 1-D model slightly underestimates the

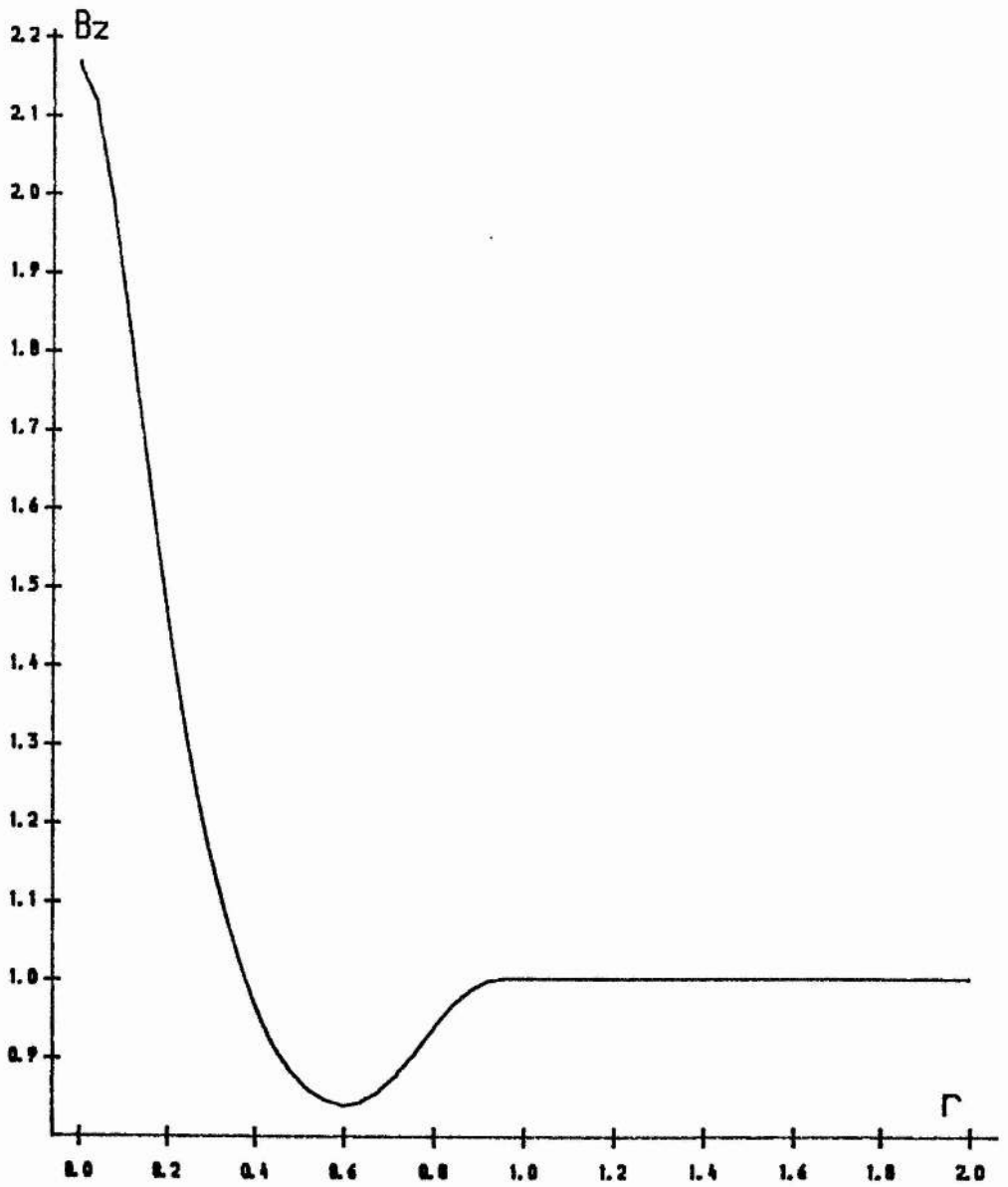

Figure 5.22. B_z for the twisted loop, for

comparison with Mikic et al.

value of $B_z(0)$ ($2.17B_o$ as opposed to $2.21B_o$) and gives the minimum B_z as $0.84B_o$ as opposed to $0.83B_o$. This is remarkably good agreement for such a simple model.

5.7 Non-uniform initial flux distribution.

The final case which we examined was a non-uniform initial flux distribution. Consider the flux function

$$\begin{aligned} A_o &= \frac{5}{2}r^2 && r < \frac{1}{2}, \\ &= \frac{1}{2}(r^2 + 1) && \frac{1}{2} < r < 1, \\ &= r^2 && r > 1. \end{aligned} \tag{5.56}$$

which represents a field concentrated near the axis. In our 1-D model, the effect of the non-uniformity will be to modify the appearance of the twist function as seen by the coronal field. For example, a twist

$$\frac{\Phi}{L} = \lambda(1 - r_o^2) \tag{5.57}$$

applied at the photosphere, which would give (5.22) for an initially uniform flux distribution, gives

$$\begin{aligned} \frac{\Phi}{L} &= \lambda\left(1 - \frac{2}{5}A\right) && A < \frac{5}{8}, \\ &= 2\lambda\,(1 - A) && \frac{5}{8} < A < 1, \\ &= 0 && A > 1 \end{aligned} \tag{5.58}$$

for (5.56). We examined the effect of applying such a twist on the coronal solution and found qualitatively similar behaviour to the results for an initially uniform flux distribution. Figures 5.23 and 5.24 show B_z and δr for λ=9.5. A more extreme case is when there is a region of the photosphere which is the source of no photospheric field. Then a twist applied at the photosphere will cause a photospheric current sheet. However, even this case gave rise to no loss of equilibrium.

5.8 Discussion.

Since a long loop is computationally expensive, most 2-D and 3-D loop analyses have been at short or moderate loop lengths,

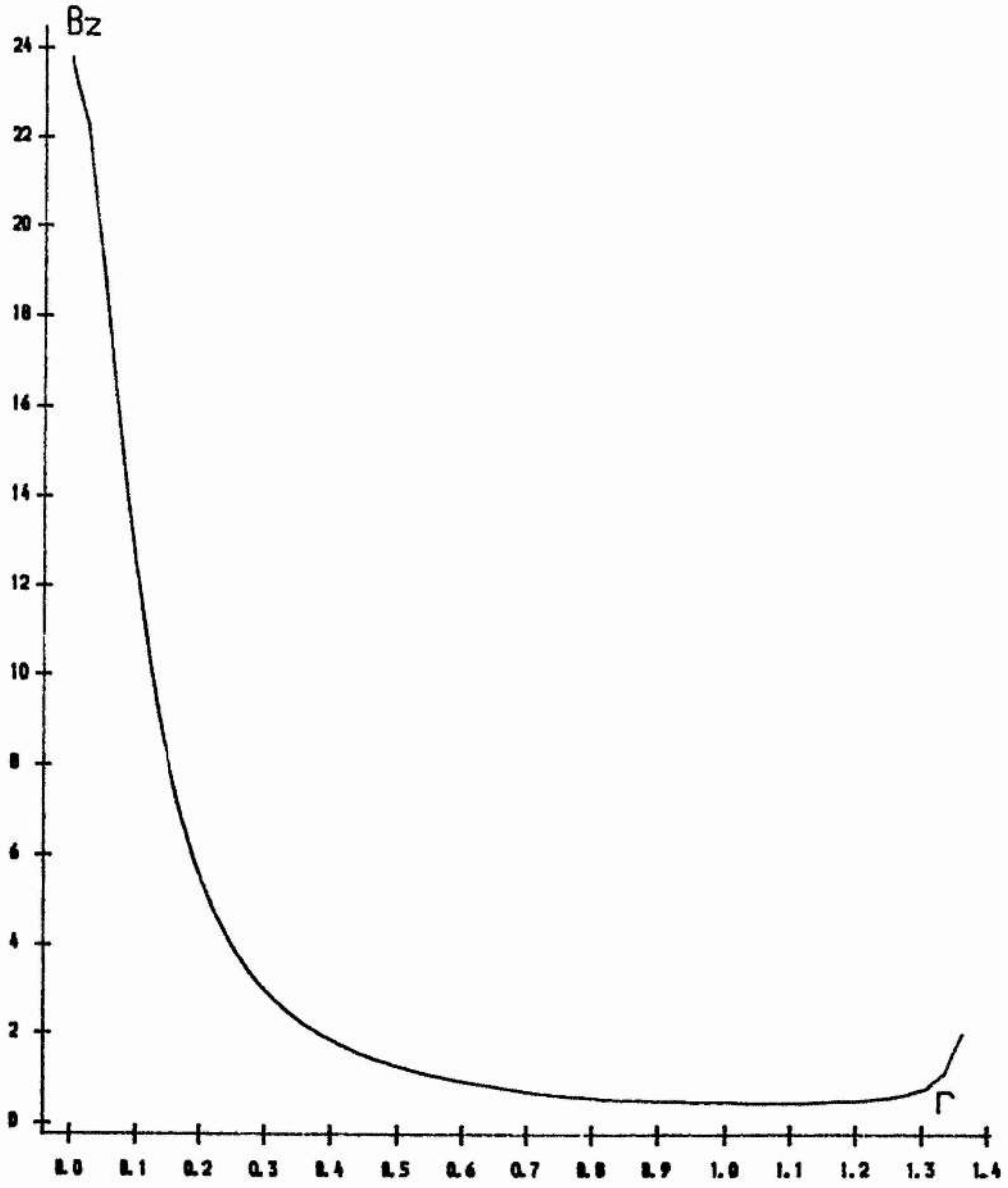

Figure 5.23. B_z for twisted loop with initially non-uniform flux distribution.

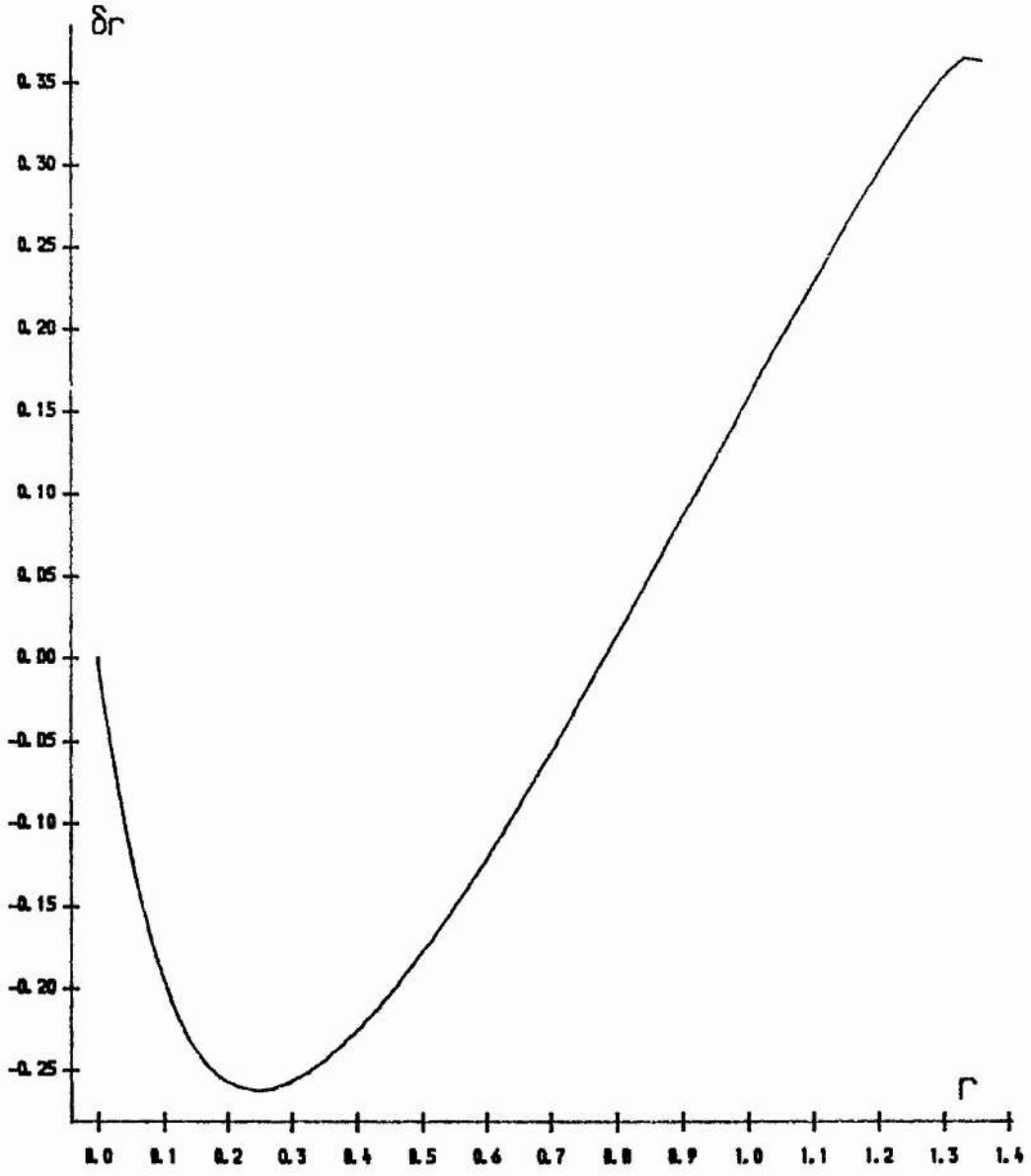

Figure 5.24. δr for twisted loop with initially non-uniform flux distribution.

rather than a length of about ten times the radius, which would correspond to observations. Nevertheless, there is remarkably good agreement between such work and the predictions of the 1-D long loop model. The 1-D model can be computed in seconds on a small computer, whereas realistic dynamical simulations require hours on very large computers.

It is particularly difficult to make comparisons for the case of a non-uniform initial flux distribution. Robertson et al. have carried out a 2-D time-dependent simulation for such a case. They obtained the initial untwisted equilibrium by relaxing an initially straight field. However, due to the shortness of their loop, the resulting field at the mid-plane of their loop was far from uniform (ranging from $1.83B_o$ to $0.82B_o$). Obviously, no comparison can be made between the effect of twisting such a field and the 1-D model.

Using our 1-D model, we have examined a number of different approaches to the non-equilibrium problem. Whereas non-equilibrium occurs for a tube with fixed K(A), the more physical approach of specifying the twist on each field line gives no loss of equilibrium. Sufficiently high pressure can drive a loop out of equilibrium, but this requires $\beta>1$. If we consider the loop to expand adiabatically, the requirement becomes $\beta>>1$. Even a non-uniform initial flux distribution appears to give no loss of equilibrium when twisted. We conclude that a low-beta, twisted coronal loop is unlikely to lose equilibrium.

Chapter 6. Conclusions.

We have derived the equations governing the behaviour of coupled tearing modes in tokamaks and solved them in the case of three modes coupled by elliptic shaping, when two of the modes have singular surfaces in the plasma. Current profiles exist for which the two singular modes are both stable in the limit of a circular cylinder, but for which the coupled mode becomes unstable at a degree of ellipticity typical of real tokamaks. So far only non-monotonic current profiles have shown this property. Since such profiles are somewhat unphysical, it would be desirable to find a montonic current profile for which this effect occurs. The addition of finite pressure gradients would be a useful extension of this work, as would the inclusion of more singular surfaces in the plasma.

We have studied the linear response of a line-tied coronal loop to twisting applied at its photospheric footpoints. The inner part of such a loop contracts, while its outer surface remains virtually unmoved. A long loop is straight over most of its length, with changes in radius occurring in narrow boundary layers at each end. A 1-D line-tied model is sufficient to describe most of the equilibrium properties of such a loop. It would be desirable to include realistic toroidal effects and we have indicated how this may be approached.

Using the 1-D line-tied model, we have gone on to look at the non-linear effects of twisting. In addition to the continued contraction of the loop's core, its outer layers expand. This results in a region of depleted axial field developing. Apparent non-equilibrium was found for a sufficiently twisted loop, when the azimuthal field at the footpoints was specified. However, no such loss of equilibrium was found when, more physically, the twist on each field line was specified. Addition of suficient pressure was found to cause loss of equilibrium, but only when β was order 1. A

2-D investigation of this showed that slightly higher pressures could be contained by tension effects. Since the coronal β is low, we do not expect this loss of equilibrium to be relevant to coronal loops. In an adiabatic process, non-equilibrium is not found until $\beta >> 1$. Twisting an initially non-uniform field does not result in non-equilibrium. The 1-D line-tied loop model was compared with 2-D and 3-D dynamical simulations and found to agree well with their results. The fact that some properties of a loop are well described by such a simple, computationally cheap model is remarkable. The logical continuation of this work would be a study of the MHD stability of coronal loop equilibria.

References.

Abramowitz M. and Stegun I.A., *Handbook of Mathematical Functions*, (Dover: New York), (1972)

Bateman G., *MHD Instabilities* (Cambridge, Mass. : MIT Press), (1978).

Browning P.K. and Hood A.W., *Solar Phys.* **124**, 271 (1989).

Browning P.K. and Priest E.R., *Astrophys. J.* **266**, 848 (1983).

Bussac M.N., Pellat R., Edery D. and Soulé J.L., *Phys. Rev. Lett.* **35**, 1638 (1975).

Carreras B.A., Hicks H.R. and Lee D. K., *Phys. Fluids* **24**, 66 (1981).

Connor J.W., Cowley S.C., Hastie R.J., Hender T.C., Hood A. and Martin T.J., *Phys. Fluids* **31**, 577 (1988).

Connor J.W. and Hastie R.J., *Culham Laboratory Report* CLM-M106 (1985).

Coppi. B., Galvao R., Pellat R., Rosenbluth M.N. and Rutherford P. M., *Sov. J. Plasma Phys.* **2**, 533.

Finn J.M. and Chen. J., *NRL Report* 6402 (1989).

Furth H.P., Killeen J. and Rosenbluth M.N., *Phys. Fluids* **6**, 459 (1963).

Furth H.P., Rutherford P.H. and Selberg H. *Phys. Fluids* **16**, 1054 (1973).

Gill R.D. (ed.), *Plasma Physics And Nuclear Fusion Research*, (London : Academic Press), (1981).

Glasser A.H., Greene J.M. and Johnson J.L., *Phys. Fluids* **18**, 875 (1975).

Greene J.M., Johnson J.L. and Weimer K.E., *Phys. Fluids* **14**, 671 (1971).

Hamada S., *Nucl. Fusion* **2**, 23 (1962).

Hood A.W. and Priest E.R., *Solar Phys.* **64**, 303 (1983).

Izzo R., Monticello D.A., De Lucia J., Park W. and Ryu C.M., *Phys. Fluids* **28**, 903 (1981).

Lentini M. and Pereyra V., *SIAM J. Numerical Analysis* **14**, 91 (1977).

Martin T.J., Private Discussion.

Mikic Z., Schnack D.D. and Van Hoven G., *Astrophys. J.* submitted, (1990).

Parker E.N., *Astrophys. J.* **174**, 499 (1972).

Parker E.N., *Cosmical Magnetic Fields*, (OUP: Oxford), (1979).

Priest E.R., *Solar Magnetohydrodynamics*, (Reidel: Dordrecht), (1982).

Rechester A.B. and Stix T.H., *Phys. Rev. Lett.* **36**, 587 (1976).

Robertson J.A., Hood A.W. and Lothian R.M., in preparation.

Steinolfson R. and Tajima T., *Astrophys. J.* **322**, 503 (1987).

Stix T.H., *Phys. Rev. Lett.* **36**, 521 (1976).

Waddell B.V., Carreras B., Hicks H.R., Holmes J.A. and Lee D.K., *Phys Rev. Lett.* **41**, 1386 (1978).

Waddell B.V., Carreras B., Hicks H.R. and Holmes J.A., *Phys. Fluids* **22**, 896 (1979).

Wesson J.A., *Nucl. Fusion* **16**, 130 (1966).

Wesson J.A. in Gill (1981).

White R.B., Monticello D.A., Rosenbluth M.N. and Waddell B.V., *Phys. Fluids* **20**, 800 (1977).

Zweibel E.G. and Boozer A.H., *Astrophys. J.* **295**, 642 (1985).

Appendix A

Consider a co-ordinate system (x^1,x^2,x^3) in which an infinitesimal element of length dl is given by

$$(dl)^2 = g_{ij}\, dx^i dx^j \qquad (A.1)$$

where (g_{ij}) is the metric tensor and repeated indices indicate summation. In such a system a vector **A** may be represented by contravariant components A^i given by

$$A^i = \mathbf{A}.\nabla x^i \qquad (A.2)$$

or by covariant components A_j given by

$$A_j = g_{ij}\, A^i \qquad (A.3)$$

The inverse of the metric tensor is its contravariant form (g^{ij}) which is related to the scale factors of the system by

$$g^{ij} = \nabla x^i.\nabla x^j \qquad (A.4)$$

The Jacobian J of such a system is related to the determinant of the metric tensor and the scale factors by

$$J = \sqrt{\det\ (g_{ij})} = \left[\nabla x^i.\left(\nabla x^j \times \nabla x^k\right)\right]^{-1} \qquad (A.5)$$

The following covariant and contravariant quantities are required for our analysis

$$(\nabla \times \mathbf{A})^i = \frac{1}{J}\varepsilon^{ijk}\frac{\partial A_k}{\partial x^j} \qquad (A.6)$$

$$(\mathbf{A} \times \mathbf{B})^i = \frac{1}{J}\varepsilon^{ijk}A_jB_k \qquad (A.7)$$

$$(\mathbf{A} \times \mathbf{B})_i = J\,\varepsilon_{ijk}\,A^jB^k \qquad (A.8)$$

$$\nabla.\mathbf{A} = \frac{1}{J}\frac{\partial(JA^i)}{\partial x^i} \qquad (A.9)$$

$$\mathbf{A}.\mathbf{B} = A^iB_i = A_iB^i \qquad (A.10)$$

where **A** and **B** are vector fields, V is a scalar field and ε_{ijk} is the permutation tensor.

Using (A.2), the contravariant components of the magnetic field (2.6) are obtained as

$$B^{\rho} = 0 \; ; \; B^{\omega} = R_o B_o \frac{f}{J} \; ; \; B^{\phi} = R_o B_o \frac{g}{R^2} \qquad (A.11)$$

Using (A.3), (A.5) and (A.11), the contravariant components of the current are

$$J^{\rho} = 0 \; ; J^{\omega} = -R_o B_o \frac{g'}{J} \; ; J^{\phi} = \frac{R_o B_o}{J}\left[\frac{\partial}{\partial \rho}\left(\frac{f g_{\omega\omega}}{J}\right) - \frac{\partial}{\partial \omega}\left(\frac{f g_{\rho\omega}}{J}\right)\right] \quad (A.12)$$

The ρ covariant component of the Lorentz force ($\mathbf{J} \times \mathbf{B}$) is

$$[\mathbf{J} \times \mathbf{B}]_{\rho} = R_o^2 B_o^2 \left[- \frac{gg'}{R^2} - \frac{f}{J}\left(\frac{\partial}{\partial \rho}\left(\frac{f g_{\omega\omega}}{J}\right) - \frac{\partial}{\partial \omega}\left(\frac{f g_{\rho\omega}}{J}\right)\right)\right] \quad (A.13)$$

and the other components, as expected, vanish identically. Equating this to $(\nabla p)_{\rho}$ gives the equilibrium equation (2.7).

Appendix B

We wish to approximate our large aspect ratio tokamak to a cylinder, adding corrections as higher order terms in the inverse aspect ratio of the tokamak. In order to do this we shall non-dimensionalise our lengths against R_o, the major radius of the magnetic axis. The co-ordinate ρ will be non-dimensionalised against the minor radius a, giving rise to factors of ε. Conversely, the non-dimensionalisation of ρ-derivatives gives rise to a factor ε^{-1}. The factors ρ in equation (2.9) have already been non-dimensionalised in this way. We shall now expand equation (2.7) in powers of ε, while non-dimensionalising.

The expansions of $g_{\omega\omega}$ and $g_{\rho\omega}$ may be obtained from (2.4) and (2.9) as

$$g_{\omega\omega} = R_o^2 \left[\varepsilon^2\rho^2 + \varepsilon^3 \left(2\rho \sum_n S^n(n-1)\cos(n\omega) \right) + \varepsilon^4 \left(-2\rho P + \left(\sum_n S^n(n-1)\cos(n-1)\omega \right)^2 + \left(\sum_n S^n(n-1)\sin(n-1)\omega \right)^2 \right) \right] \quad (B.1)$$

$$g_{\rho\omega} = R_o \left[\varepsilon^2 \left[\sum_n (\rho S^{n'} + (n-1)S^n)\sin(n\omega) - \rho\Delta'\sin\omega \right] + \varepsilon^3 \left[\Delta' \sum_n S^n(n-1)\sin(n-1)\omega + \sum_{n,m} (n-1)S^n S^{m'} \cos(n-1)\omega \sin(m-1)\omega \right] \right] \quad (B.2)$$

while the Jacobian J is given by

$$J = R_o \left[\varepsilon\rho + \varepsilon^2 \left[\sum_n ((n-1)S^n - \rho S^{n'})\cos(n\omega) + \rho\Delta'\cos\omega \right] + \varepsilon^3 \left(-(\rho P') + \Delta' \sum_n S^n(n-1)\cos(n-1)\omega - \sum_{n,m} (n-1)S^n S^{m'} \cos(n-m)\omega \right) \right] \quad (B.3)$$

Where ' denotes the derivative with respect to the

non-dimensionalised ρ and $S^{n'} = d(S^n)/d\rho$.

Hence, the terms in equation (2.7) have the following orders :

$$\frac{f}{J} = O(1) \; ; \; \frac{\partial}{\partial\rho}\left(\frac{fg_{\omega\omega}}{J}\right) = O(\varepsilon) \; ; \; \frac{\partial}{\partial\omega}\left(\frac{fg_{\rho\omega}}{J}\right) = O(\varepsilon^2) \; ; \; \frac{p'}{R_o^2 B_o^2} = O(\varepsilon^2) \qquad (B.4)$$

It is now obvious that g must expand as

$$g = 1 + \varepsilon^2 g_2 + \ldots \qquad (B.5)$$

in order that the final term on the LHS of (2.7) is not unbalanced. The straightforward, but laborious, substitution of (2.8), (2.9) and (B.1)-(B.3) into (2.7) now yields equations (2.10)-(2.12) from its various orders. Note that the field and current components and the equilibrium equation in this co-ordinate system may be obtained simply by replacing ρ and ω, by r and θ respectively, everywhere in equations (A.11)-(A.13). In order to obtain the scale factors of the new system, we must first derive their counterparts in the old system. This we may do by a trivial matrix inversion on the metric tensor, giving us its contravariant components:

$$g^{\rho\rho} = \frac{R^2 g_{\omega\omega}}{J^2} \; ; \; g^{\omega\omega} = \frac{R^2 g_{\rho\rho}}{J^2} \; ; \; g^{\rho\omega} = -\frac{R^2 g_{\rho\omega}}{J^2} \qquad (B.6)$$

We may now calculate the scale factors of the new system by using the standard rules for contravariant tensor transformations, bearing in mind that $\partial r/\partial\rho = 1$ and $\partial r/\partial\omega = 0$. Hence,

$$|\nabla r|^2 = g^{rr} = g^{\rho\rho} \; ; \; |\nabla\theta|^2 = g^{\theta\theta} = g^{\rho\rho}\left(\frac{\partial\theta}{\partial\rho}\right)^2 + g^{\omega\omega}\left(\frac{\partial\theta}{\partial\omega}\right)^2 + 2g^{\rho\omega}\frac{\partial\theta}{\partial\rho}\frac{\partial\theta}{\partial\omega};$$

$$\nabla r.\nabla\theta = g^{r\theta} = g^{\rho\rho}\frac{\partial\theta}{\partial\rho} + g^{\rho\omega}\frac{\partial\theta}{\partial\omega} \qquad (B.7)$$

The explicit forms (2.17) may be obtained after some algebraic manipulation.

Appendix C

Marginally Stable Ideal MHD in Toroidal Co-ordinates.

We wish to express equations (3.1)-(3.4) in the co-ordinate system of Chapter 2. The equations are:

$$\nabla(\delta p) = \delta \mathbf{J} \times \mathbf{B} + \mathbf{J} \times \delta \mathbf{B} \tag{3.1}$$

$$\delta \mathbf{J} = \nabla \times \delta \mathbf{B} \tag{3.2}$$

$$\delta p = - \xi . \nabla p \tag{3.3}$$

$$\nabla . \delta \mathbf{B} = 0 \tag{3.4}$$

Since p is a function of r alone, (3.3) becomes

$$\delta p = - \xi^r p' \tag{C.1}$$

Suppressing R_o and B_o and replacing ρ, ω by r, θ in (A.11)-(A.13) gives us the contravariant equilibrium field components

$$B^r = 0 \; ; \; B^\theta = \frac{f}{rR^2} \; ; \; B^\phi = \frac{g}{R^2} \tag{C.2}$$

and current components

$$J^r = 0 \; ; \; J^\theta = \frac{-g'}{rR^2} \; ; \; J^\phi = \frac{1}{rR^2}\left[\frac{\partial}{\partial r}\left(\frac{f g_{\theta\theta}}{rR^2} \right) - \frac{\partial}{\partial \theta}\left(\frac{f g_{r\theta}}{rR^2} \right) \right] \tag{C.3}$$

The covariant components of (3.1) are (using (A.7))

$$rR^2 \left\{ \delta J^\theta B^\phi - \delta J^\phi B^\theta + J^\theta \delta B^\phi - J^\phi \delta B^\theta \right\} + \frac{\partial}{\partial r}\left(\xi^r p' \right) = 0 \tag{C.4}$$

$$rR^2 \left\{ J^\phi \delta B^r - \delta J^r B^\phi \right\} + \frac{\partial}{\partial \theta}\left(\xi^r p' \right) = 0 \tag{C.5}$$

$$rR^2 \left\{ \delta J^r B^\theta - \delta B^r J^\theta \right\} + \frac{\partial}{\partial \phi}\left(\xi^r p' \right) = 0 \tag{C.6}$$

Now, we take (C.5)B^θ + (C.6)B^ϕ and employ the equilibrium equation to obtain

$$\delta B^r = \frac{1}{rR^2}\left(\frac{\partial}{\partial \theta} + q \frac{\partial}{\partial \phi} \right)(f \xi^r) \tag{C.7}$$

Using (A.9), (3.4) has the form

$$\frac{\partial}{\partial r}(rR^2 \delta B^r) + \frac{\partial}{\partial \theta}(rR^2 \delta B^\theta) + \frac{\partial}{\partial \phi}(rR^2 \delta B^\phi) = 0 \tag{C.8}$$

Using (A.3) and the fact that (g_{ij}) is the inverse of (g^{ij}), we may obtain

the covariant components of δB as

$$\delta B_r = r^2R^2|\nabla\theta|^2\delta B^r - r^2R^2\nabla r.\nabla\theta\ \delta B^\theta\ ;$$

$$\delta B_\theta = r^2R^2|\nabla r|^2\delta B^\theta - r^2R^2|\nabla r.\nabla\theta|\ \delta B^r\ ;\ \delta B_\phi = R^2\delta B^\phi \qquad (C.9)$$

Hence, from (3.2) and (A.6), the contravariant components of δJ are

$$\delta J^r = \frac{1}{rR^2}\left[\frac{\partial}{\partial\theta}\left(R^2\delta B^\phi\right) - \frac{\partial}{\partial\phi}\left(r^2R^2|\nabla r|^2\delta B^\theta - r^2R^2\nabla r.\nabla\theta\ \delta B^r\right)\right];$$

$$\delta J^\theta = \frac{1}{rR^2}\left[\frac{\partial}{\partial\phi}\left(r^2R^2|\nabla\theta|^2\delta B^r - r^2R^2\nabla r.\nabla\theta\ \delta B^\theta\right) - \frac{\partial}{\partial r}\left(R^2\delta B^\phi\right)\right];$$

$$\delta J^\phi = \frac{1}{rR^2}\left[\frac{\partial}{\partial r}\left(r^2R^2|\nabla r|^2\delta B^\theta - r^2R^2\nabla r.\nabla\theta\ \delta B^r\right)\right.$$

$$\left. - \frac{\partial}{\partial\theta}\left(r^2R^2|\nabla\theta|^2\delta B^r - r^2R^2\nabla r.\nabla\theta\ \delta B^\theta\right)\right] \qquad (C.10)$$

Substituting from (C.2), (C.3) and (C.10), (C.4) and (C.6) become

$$\left(\frac{\partial}{\partial\phi}\left[r^2R^2|\nabla\theta|^2\delta B^r - r^2R^2\nabla r.\nabla\theta\ \delta B^\theta\right] - \frac{\partial}{\partial r}\left(R^2\delta B^r\right)\right)\frac{g}{R^2} - g'\,\delta B^\phi$$

$$- \left[\frac{\partial}{\partial r}\left(rfR^2|\nabla r|^2\right) + \frac{\partial}{\partial\theta}\left(rfR^2\nabla r.\nabla\theta\right)\right]\delta B^\phi + \frac{\partial}{\partial r}\left(\xi^r p'\right)$$

$$- \frac{f}{rR^2}\left[\frac{\partial}{\partial r}\left(r^2R^2|\nabla r|^2\delta B^\theta - r^2R^2\nabla r.\nabla\theta\ \delta B^r\right)\right.$$

$$\left. - \frac{\partial}{\partial\theta}\left(r^2R^2|\nabla\theta|^2\delta B^r - r^2R^2\nabla r.\nabla\theta\ \delta B^\theta\right)\right] \qquad (C.11)$$

and

$$\left(\frac{\partial}{\partial\theta}\left(R^2\delta B^\phi\right) - \frac{\partial}{\partial\phi}\left(r^2R^2|\nabla r|^2\delta B^\theta - r^2R^2\nabla r.\nabla\theta\ \delta B^r\right)\right)\frac{f}{rR^2}$$

$$+ g'\,\delta B^r + \frac{\partial}{\partial\phi}\left(\xi^r p'\right) = 0 \qquad (C.12)$$

We now define new variables $y = f\xi^r$ and $z = R^2\delta B^\phi$, using (C.7) to eliminate δB^r. Assuming that all perturbed quantities vary as $\exp(-in\phi)$, we may express (C.8),(C.10) and (C.11) as

$$\frac{\partial}{\partial r}\left(\frac{\partial}{\partial\theta} - inq\right)y + \frac{\partial}{\partial\theta}\left(rR^2\delta B^\theta\right) - inr\,z = 0 \qquad (C.13)$$

$$\left[-in \left(r|\nabla\theta|^2 \left(\frac{\partial}{\partial\theta} - inq \right) y - r^2R^2 \nabla r.\nabla\theta\, \delta B^\theta \right) - \frac{\partial z}{\partial r} \right] \frac{g}{R^2} - \frac{g'}{R^2} z$$

$$- \left[\frac{\partial}{\partial r} \left(frR^2 |\nabla r|^2 \right) + \frac{\partial}{\partial\theta} \left(frR^2 \nabla r.\nabla\theta \right) \right] \delta B^\theta + \frac{\partial}{\partial r} \left(\frac{p'}{f} y \right) -$$

$$\frac{f}{rR^2} \left[\frac{\partial}{\partial r} \left[r^2R^2 |\nabla r|^2 \delta B^\theta - r\nabla r.\nabla\theta \left(\frac{\partial}{\partial\theta} - inq \right) y \right] \right.$$

$$\left. - \frac{\partial}{\partial\theta} \left[r|\nabla\theta|^2 \left(\frac{\partial}{\partial\theta} - inq \right) y - r^2R^2 \nabla r.\nabla\theta\, \delta B^\theta \right] \right] = 0 \qquad \text{(C.14)}$$

$$\left(\frac{\partial z}{\partial\theta} - in \left[r^2R^2 |\nabla r|^2 \delta B^\theta - r\nabla r.\nabla\theta \left(\frac{\partial}{\partial\theta} - inq \right) y \right] \right) \frac{f}{rR^2}$$

$$+ \frac{g'}{rR^2} \left(\frac{\partial}{\partial\theta} - inq \right) y - in \frac{p'}{f} y = 0 \qquad \text{(C.15)}$$

We now substitute for δB^θ from (C.15) in (C.13) to obtain (3.5) and in (C.14) to obtain (3.6), after using (3.5) to eliminate undifferentiated z terms. We observe that, we could include compressibility by changing the definition of y. For example, if the motion is polytropic, (i.e. $p = k\rho^\alpha$, where ρ is the density), then equations (3.5) and (3.6) hold with $y = f(\xi^r + \alpha p(\nabla.\xi)/p')$. Also, note that the perturbed field is linked to the displacement by the perturbed ideal induction equation

$$\delta\mathbf{B} = \nabla \times (\xi \times \mathbf{B}) \qquad \text{(C.16)}$$

which was not required in the above analysis. Note, however, that the first component of (C.16) is identical to (C.7). This loss of an independent equation is a result of the imposition of the additional constraint of incompressibility, since (C.7) appears here as a result of (3.3).